INORGANIC CHEMISTRY
FRONTIERS

REVIEW

View Article Online
View Journal | View Issue

Cite this: *Inorg. Chem. Front.*, 2020, **7**, 4711

Usage of P–V–L bond theory in studying the structural/property regulation of microwave dielectric ceramics: a review†

Hongyu Yang,[a] Shuren Zhang,*[b] Hongcheng Yang[a] and Enzhu Li *[b]

Received 27th July 2020,
Accepted 22nd September 2020

DOI: 10.1039/d0qi00907e

rsc.li/frontiers-inorganic

Structure/property regulation is widely investigated for providing theoretical foundations and guidance for designing microwave dielectric ceramics. P–V–L bond theory targets the provision of detailed structural parameters of crystals and fundamental chemical bond characteristics, such as bond ionicity, bond covalency and bond susceptibility. In this review, the concept of P–V–L bond theory, the binary bonding formula theory of complex polycrystalline and the usage of P–V–L bond theory regarding the structural effects on dielectric properties in various crystal structures are introduced. And the bond traits provided *via* P–V–L bond theory in several ion-doping modification systems are generalized with structural evolution and dielectric properties. Furthermore, conjectures about the development and application directions of P–V–L bond theory in the study of structure/properties of microwave dielectric ceramics are put forward.

1. Introduction

Microwave dielectric ceramics (MWDCs) are widely used in microwave frequency (300 MHz–300 GHz) circuits as dielectric materials to supply one or more functions. MWDCs have become promising in electronic communication technology for their widespread applications in filters, resonators, RF/antennae, frequency discriminators in electronic countermeasures, navigation, radar, home satellite live television receivers and hand-held mobile phones.[1,2] For their practical application, three key indicators are required: a moderate dielectric constant ε_r value to make the size of the device controllable, a high $Q \times f$ value ($Q = 1/\tan\delta$, f is the resonant frequency) to reduce the insertion loss of the application, and a near zero τ_f value to ensure the carrier signal of the application does not drift with the working environment of the communication devices.[3,4] Specifically, ceramics with various ε_r values show different application fields: *e.g.* $\varepsilon_r < 20$: Al_2O_3 ($\varepsilon_r = 10$, $Q \times f = 500\,000$ GHz)[5] for electronic circuit packages and dielectric resonance antennae, Zn_2SiO_4 ($\varepsilon_r = 6.6$, $Q \times f = 219\,000$ GHz, $\tau_f = -61$ ppm per °C)[6] and $(Mg_{1-x}Zn_x)Al_2O_4$ ($\varepsilon_r = 7.9$–8.5, $Q \times f = 82\,000$–$106\,000$ GHz, $\tau_f = -73$ ppm per °C)[7] for microwave

[a]*Department of Electronic Science and Engineering, University of Electronic Science and Technology of China, Chengdu, Sichuan, China*
[b]*Department of Electronic Science and Engineering, University of Electronic Science and Technology of China, Chengdu, Sichuan, China. E-mail: zsr@uestc.edu.cn, lienzhu@uestc.edu.cn*

†Electronic supplementary information (ESI) available. See DOI: 10.1039/d0qi00907e

Hongyu Yang

Hongyu Yang is a PhD candidate in the School of Electronic Science and Engineering, University of Electronic Science and Technology of China, Chengdu. He obtained his Bachelor's Degree in 2015 from the Southwest University of Science and Technology, China. His research interests include microwave dielectric materials and low temperature co-fired ceramics.

Shuren Zhang

Shuren Zhang is a professor in the School of Electronic Science and Engineering, University of Electronic Science and Technology of China, Chengdu. His research interests include electronic materials and devices, electronic materials and engineering, electronic thin films and integrated devices.

substrates; $20 < \varepsilon_r < 70$: $Ba(B_{1/3}B'_{1/3})O_3$ (B = Zn/Mg/Co/Ni, B′ = Ta/Nb) series of complex perovskite structures[1,8–11] ($BaZn_{1/3}Ta_{2/3}O_3$: ε_r = 29, $Q \times f$ = 150 000 GHz, τ_f = 0 ppm per °C), $BaTi_4O_9$,[12] $Ba_2Ti_9O_{20}$[13] and $(Zr, Sn)TiO_4$[14,15] for microwave dielectric resonance devices; $\varepsilon_r > 70$: $BaO–Ln_2O_3–TiO_2$ (Ln = Sm, Nd)[16–18] and $CaO–Li_2O–Ln_2O_3–TiO_2$[19–21] systems. Up to now, several MWDC materials with ε_r values of 5–100 have been commercialized, possessing excellent high $Q \times f$ values and zero τ_f values:[1] *e.g.* $BaB_{1/3}Ta_{2/3}O_3$ (B = Mg, Zn), $Ba(Co, Zn)_{1/3}Nb_{2/3}O_3$, $SrTiO_3–LaAlO_3$, and $ZrTiO_4–ZnNb_2O_6$. Driven by the rapid development of the internet of things (IoT) and 5th generation wireless systems (5G), much effort has been devoted to the exploration of novel MWDC materials with excellent dielectric performances.

Considering that crystal structures of different microwave dielectric ceramics are quite different, it is of great significance to study the influence of crystal structure and the origin of dielectric properties of ceramics in the microwave region for improvements in design and performance.[22,23] The properties of microwave dielectric ceramics are affected mainly by the crystal structure and fabrication process. The fabrication process, such as raw materials, preparation technology, phase structure, numbers of grain boundaries per volume, grain growth, porosity and sintering aids, inevitably results in extrinsic loss of microwave dielectric properties. For instance, the choice of boric acid as a raw material instead of boron oxide is attributed to its better solubility and dispersion in deionized water when preparing $Li_2O–B_2O_3–SiO_2$ glass frit.[24] A sol–gel method realizes better uniformity at the molecular level than a solid-state process, which is beneficial for improving the $Q \times f$ value.[25] A high sintering temperature positively affects the cation ordering of $Ba(Mg_{1/3}Ta_{2/3})O_3$ ceramics and then improves the $Q \times f$ value.[26] Ceramic samples with compact microstructures and uniform distributions of average grain size can also reduce the extrinsic dielectric loss.[27] When controlling external factors, such as preparation/fabrication technology, the influence of crystal structure as an internal factor has a crucial impact on microwave dielectric performance. Up to now, several theories have been developed to study the regulation between crystal structure and dielectric properties. For example, THz time-domain spectroscopy and far-infrared reflectance spectroscopy can be used to analyse the intrinsic properties of the lattice vibration of material systems;[28–31] the Clausius–Mossotti equation predicts the macroscopic dielectric constant of an ionic crystal by using ionic polarizabilities;[32,33] bond-valence theory gives the actual valence state of ions in a crystal structure and provides the basis for the state of the ions.[34–37] These concepts help researchers gain better insights into the relationship between crystal structure and dielectric properties.

Nowadays, the chemical bond theory named the P–V–L bond theory, established by Phillips, Van Vechten and Levine,[38–43] which provides fundamental bond characteristics, has been paid increasing attention and been applied to various dielectric ceramic systems to discuss the influence of crystal structure on the variation in chemical bond parameters and to establish the relationship between chemical bond characteristics and dielectric properties.

Chemical bond characteristics of crystals are crucial for analysing and studying the chemical and solid-state physical aspects of crystal structures. Several crystal features can be explained qualitatively using these concepts: *e.g.* the greater the electronegativity difference between A and B atoms in binary compounds, the more likely it is that a rock salt structure can be formed, otherwise an open covalent structure is preferred.[41] During the early 1970s, the chemical bond theory first proposed by Phillips and Van Vechten (abbreviated as P–V) was applied to characterize crystal features quantitatively. This theory relies on the dielectric definition of crystals and defines the calibration of chemical bond characteristics and the relationship between various micro-parameters in crystals. It has been used effectively to calculate many aspects of crystals, such as bond charge,[44,45] elastic and piezoelectric constants,[46,47] electronic structure,[48] thermodynamic properties,[49] cohesive energies and heats of formation,[50] nonlinear optical susceptibilities,[51–53] effective lattice charges,[54] valence band parameters,[55] band structures,[56] impurity binding energies,[57] photoelastic constants,[58,59] and electro-optic and elasto-optic phenomena.[60] It should be noted that the P–V theory applies only to eight-electron A^NB^{8-N} type crys-

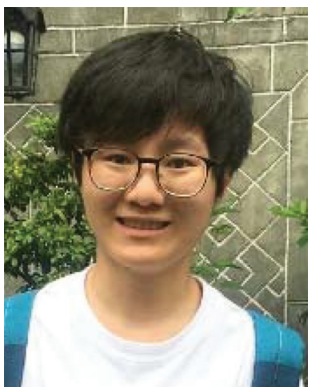

Hongcheng Yang

Hongcheng Yang is a PhD candidate in the School of Electronic Science and Engineering, University of Electronic Science and Technology of China, Chengdu. She obtained her Bachelor's Degree in 2016 from the Southwest University of Science and Technology, China. Her research interests include microwave dielectric materials and low temperature co-fired ceramics.

Enzhu Li

Enzhu Li is a professor in the School of Electronic Science and Engineering, University of Electronic Science and Technology of China, Chengdu. She received her PhD degree from Tokyo Institute of Technology in 2008. Her research interests include microwave dielectric materials and low temperature co-fired ceramics.

tals with one type of chemical bond: *e.g.* zinc blende, wurtzite, and rock salt. Following that, Levine then expanded the application of P–V bond theory to A_mB_n (NaCl, $A^{IV}B^{VI}$, $A^{N}B^{16-N}$), $A^{I}B^{III}C_2^{VI}$, $A^{II}B^{IV}C_2^{V}$ and $A^{III}B^{V}C_4^{VI}$ systems by dividing the crystal properties into parameters related to a single bond, such as polarizability, ionic properties and the average number of electrons per bond.[42] However, it should be realized that there are limitations since two types of bonds, with the same coordination number and nearly the same nearest-neighbour distances should be satisfied simultaneously. Even so, a normalization idea attributing the crystal properties to individual chemical bonds was developed.

In order to make P–V–L bond theory more applicable to extensive and complex multi-component crystals ($A_aB_bC_cD_d$), Zhang put forward the idea of decomposing complex polycrystals into binary crystals, where the crystal can be regarded as an aggregation of chemical bonds between ions.[61,62] Suppose that two ions that make up the chemical bond have the same symmetrical positions in the crystal, and bonds with the same length belong to one type of bond. Each kind of chemical bond with a binary expression has its own specific bond parameters, spatial configuration and proportion of elements. If the element proportional relationship of this kind of chemical bond is called a binary bond formula, then each kind of chemical bond in a crystal corresponds to a unique binary bond formula. The complex crystal is the aggregation of all the kinds of chemical bonds, and the molecular formula of the crystal is the sum of all the kinds of binary bond formulae. Then P–V–L bond theory can be applied to calculate the binary bond formula. Finally, once the relationship between the binary bond formula and complex crystals has been established, the purpose of studying the chemical bond properties of multiple complex crystals can be understood, and the relationship between microstructural parameters and macroperformance can be constructed. With these considerations in mind, P–V–L bond theory has been applied to several complex compounds. For instance, in a high-temperature oxide superconductor structure, the relationships between critical transition temperature and covalency have been established in $REBa_2Cu_3O_7$ (RE = Ln)[63,64] and $HgBa_2Ca_{n-1}Cu_nO_{2n+2+\delta}$ systems.[65] The calculation of chemical bond parameters of a hexagonal ferrite (such as M-type $BaFe_{12}O_{19}$ or W-type $BaCo_2Fe_{16}O_{27}$) crystal solved the calculation of isomeric displacement of Mössbauer spectra;[66] the stability of crystal structures was predicted *via* the calculations of lattice energy and thermal expansion of solid materials,[67,68] *etc*. Therefore, the physical and chemical properties of complex crystals have been explained at the scale of chemical bonds. Similarly, with the help of the binary bond splitting theory of polycrystalline materials, the P–V–L bond theory is expected to be applicable in MWDC systems.

In this contribution, we review the bond theory established by Phillips, Van Vechten and Levine and the binary bonding formula theory of complex polycrystals proposed by Zhang, and we specifically precis current studies focusing on structure–properties relationships discussed using P–V–L bond theory, and summarizing how P–V–L bond theory correlates with microwave dielectric properties.

2. P–V–L bond theory

The chemical bond theory established by Phillips, Van Vechten and Levine (P–V–L) is a dielectric description of the chemical bonds in a crystal structure, which correlates the structure and dielectric properties of a crystal. Firstly, in the theoretical calculation of a binary crystal $A^{N}B^{8-N}$, Phillips chose to build a unit cell with two atoms, where a symmetrical coordinate system is based on the middle position of the atoms.[41] Thus, the periodic potential of a crystal is expanded by Fourier transformation:

$$V(\boldsymbol{r}) = \sum_G V_G \cdot \exp(i\boldsymbol{G}\cdot\boldsymbol{r}) \quad (1)$$

$$V_G = [V_A(\boldsymbol{G}) + V_B(\boldsymbol{G})]\cdot\cos(\boldsymbol{G}\cdot\boldsymbol{r}) + i[V_A(\boldsymbol{G}) - V_B(\boldsymbol{G})]\cdot\sin(\boldsymbol{G}\cdot\mathbf{r}) \quad (2)$$

where $\boldsymbol{G}$ refers to the reciprocal lattice vector, V_A and V_B are the pseudopotentials of atoms A and B, and $V_A + V_B$ is the homopolar potential, and $V_A - V_B$ is the ionic potential. Therefore, eqn (2) between real basis functions is:

$$H_{12} = H_{21}^{*} = (E_h + iC)/2 \quad (3)$$

That is, the average energy gap between bonding and antibonding molecular orbitals E_g is divided into two parts: the average covalent energy gap E_h caused by homopolar potential energy and the average ionic energy gap C caused by ionic potential energy. The following relationship was put forward:

$$E_g^{\,2} = E_h^{\,2} + C^2 \quad (4)$$

The expressed form of the complex dielectric function is given as $\varepsilon(\omega) = \varepsilon_1(\omega) + i\varepsilon_2(\omega)$, which is correlated with the Kramers–Kronig relationship:

$$\varepsilon_1(\omega) = 1 + \pi^{-1}\cdot\int_{-\infty}^{\infty}\frac{\varepsilon_2(\omega')}{\omega'-\omega}\mathrm{d}\omega \quad (5)$$

By using a nearly free electron model isotropically applied to three dimensions, the low frequency limit $\varepsilon_1(0)$ was given as follows:[69]

$$\varepsilon_1(0) = 1 + \left(\frac{\hbar\cdot\omega_p}{E_g}\right)^2\cdot A \quad (6)$$

$$A = \left[1 - \left(\frac{E_g}{4E_F}\right) + \frac{1}{3}\left(\frac{E_g}{4E_F}\right)^2\right] \quad (7)$$

$$\omega_p^{\,2} = \frac{4\pi Ne^2}{m} \quad (8)$$

where $\hbar\omega_p$ refers to the Planck constant, E_F is the Fermi energy, E_g is the energy gap, N equals 4/atomic volume, and ω_p is the free electron plasma frequency.

Following that, Van Vechten provided calculation methods for the electronic dielectric constants of 68 crystals.[39,40] The homopolar part E_h is in reverse proportion to the nearest-neighbour distance, and the expression of the heteropolar part C is given as:

$$E_h = 39.74 \cdot r^{-2.48}\ \text{eV} \quad (9)$$

$$C_{AB} = 14.4 \cdot b \cdot \left(\frac{Z_A}{r_A} - \frac{Z_B}{r_B}\right) \cdot e^{(-k_s \cdot R)}\ \text{eV} \quad (10)$$

$$R = \frac{r_A + r_B}{2} \quad (11)$$

$$k_s = (4k_F/\pi a_0)^{1/2} \quad (12)$$

$$k_F = (3\pi^2 N_e)^{1/3} \quad (13)$$

where r refers to the ionic radius of atom A/B, Z is the number of valence electrons on atom A/B, $e^{-k''sR}$ is the Thomas–Fermi screening factor, b is the value of order of unity obtained from ref. 39, which lies in the range 1.4–1.6, a_0 is the Bohr radius, and N_e refers to eight electrons per diatomic volume. N_e is calculated as:

$$N_e = \frac{n}{v_b} = \frac{1}{v_b}\left(\frac{Z_A}{N_{CA}} + \frac{Z_B}{N_{CB}}\right) \quad (14)$$

for a crystal with one type of bond, $v_b = 1/N_b$ (N_b refers to the bond density, which is also the number of bonds per unit volume), Z_A is the valence electron of atom A, and N_{CA} is the coordination number of atom A.

The effect of the d state in atomic cores should be considered; therefore, ε_0 is adjusted as:

$$\varepsilon(0) = 1 + \frac{(\hbar \cdot \omega_p)^2}{(E_h)^2 + (C)^2} \cdot A \cdot D \quad (15)$$

$$D = \Delta_\alpha \Delta_\beta - (\delta_\alpha\ \delta_\beta) \cdot (Z_\alpha - Z_\beta)^2 \quad (16)$$

Δ and δ are parameters for the rows of the periodic table corresponding to α and β, which are chosen from Table 1. Therefore, the dielectric constants of crystals, such as diamond, zinc blende, wurtzite and rock-salt type crystals can be predicted *via* P–V bond theory.

As is known, chemical bonds are strong interaction forces between two or more atoms/cations in a molecule or crystal. Generally, the bonds formed by electrostatic attraction and electron transfer between atoms are called ionic bonds, in which ions can be single or atomic groups, such as Na^+, Cl^- or NO_3^-. While bonds formed between atoms by sharing pairs of electrons (overlapping clouds of electrons) are covalent bonds: *e.g.* HCl: H–Cl polar bond, and Cl_2: Cl–Cl nonpolar bond. In crystals, chemical bonds are beneficial for discussing several aspects of chemical and solid-state physical properties: for instance, the heat absorption and exothermic effects of a chemical reaction, the stability of a crystal structure, the melting/boiling point and the hardness of a crystal. Therefore, it is of great importance to study the chemical bonds at great length to achieve a better understanding of a crystal structure and its chemical–physical properties.

People find it appealing to determine the ionic and covalent contribution of chemical bonds since they are not in a fully ionic or covalent state. In an $A^N B^{8-N}$ crystal, Pauling defined the ionicity from a thermochemical point of view, where the ionicity originates from extra-ionic energy Δ_{AB}, which is proportional to the absolute value of the electronegativity difference between A and B atoms (M refers to the number of resonating bonds):[41]

$$f_i = 1 - \frac{N}{M} \cdot \exp\left[-\frac{1}{4} \cdot (X_A - X_B)^2\right] \quad (17)$$

To give a spectroscopic definition of ionicity and covalency, Phillips defined the polar coordinates as in Fig. 1:

$$\tan \varphi = \frac{C}{E_h} \quad (18)$$

$$f_i = \frac{C^2}{{E_g}^2} \quad (19)$$

$$f_c = \frac{{E_h}^2}{{E_g}^2} \quad (20)$$

Table 1 Δ and δ values of elements from the periodic table

row	Δ	δ
1	1.0	1.0
2	1.0	1.0
3	1.0	1.0
4	1.12	1.0025
5	1.21	1.0050
6	1.31	1.0075

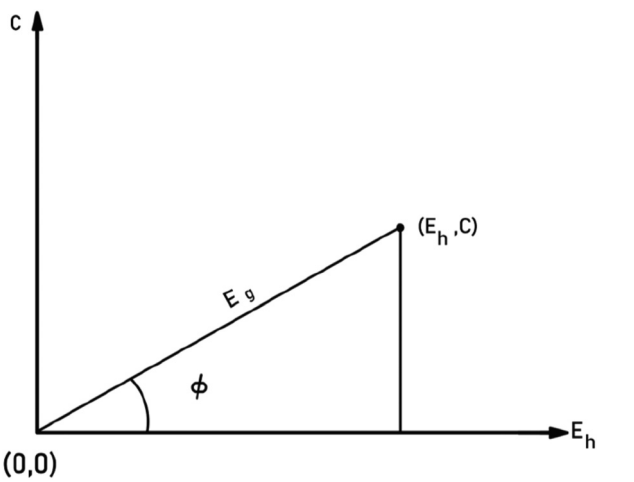

Fig. 1 A sketch showing how (E_g, φ) polar coordinates correspond to the covalent and ionic energies represented as Cartesian coordinates (E_h, C). The polar angle φ is called the ionicity phase angle (reprinted with permission from ref. 41. 2020 Copyright American Physical Society) (http://dx.doi.org/10.1103/RevModPhys.42.317).

Therefore, the ionicity or covalency of an A^NB^{8-N} crystal can be quantitatively calculated. By using the concept of ionicity, the coordination environments of 68 A^NB^{8-N} crystals, such as diamond, zinc blende, wurtzite and rock-salt type, were predicted precisely, as shown in Fig. 2, where crystals tend to be four-fold coordinated if $f_i < 0.785 \pm 0.010$; otherwise, they are six-fold coordinated.

However, it should be noted that P–V theory is restricted to A^NB^{8-N} crystals with only one type of chemical bond. To make it more applicable to other complex systems, Levine expanded the P–V theory to A_mB_n-type crystals and some systems with multiple bonds by using the idea of decomposing bulk properties into individual chemical bonds. Therefore, the macro-properties of crystal can be regarded as the sum of micro-contributions of chemical bonds. In his modification, one can expect the macro-susceptibility to be given by:[42]

$$\chi = \sum_{\mu} F^{\mu} \cdot \chi^{\mu} = \sum_{\mu} N_b^{\mu} \cdot \chi_b^{\mu} \tag{21}$$

where F^{μ} represents the proportion of μ-type bonds among all chemical bonds of crystals, χ^{μ} is the susceptibility of μ-type bonds, N_b^{μ} is the bond density of μ-type bonds, that is, the number of μ-type chemical bonds per unit volume, and χ_b^{μ} is the susceptibility of an individual bond in the μ-type bonds. The dielectric constant and susceptibility of μ-type bonds can be expressed as:

$$\chi^{\mu} = \frac{1}{4\pi} \cdot \left(\frac{\hbar \cdot \Omega_p^{\mu}}{E_g} \right)^2 \tag{22}$$

$$\varepsilon^{\mu} = 4\pi\chi^{\mu} + 1 \tag{23}$$

where ε^{μ} is the dielectric constant of a μ bond, and Ω_p^{μ} is the plasma frequency of a μ bond, which is composed of:

$$(\Omega_p^{\mu})^2 = \frac{4\pi N_e^{\mu} e^2}{m} A^{\mu} \cdot D^{\mu} \tag{24}$$

where N_e^{μ} is the number of valence electrons of a μ bond, A^{μ} and D^{μ}, similar to eqn (7) and (15) corresponding to a μ bond. The Fermi energy E_F^{μ} is calculated from the Fermi wave vector k_F^{μ}:

$$E_F^{\mu} = \frac{(\hbar \cdot k_F^{\mu})^2}{2m} \tag{25}$$

$$k_F^{\mu} = (3\pi^2 \cdot N_e^{\mu})^{1/3} \tag{26}$$

where N_e^{μ} is defined as:

$$N_e^{\mu} = \frac{n_v^{\mu}}{v_b^{\mu}} \tag{27}$$

$$n_v^{\mu} = \frac{Z_A^{\mu}}{N_{CA}^{\mu}} + \frac{Z_B^{\mu}}{N_{CB}^{\mu}} \tag{28}$$

$$v_b^{\mu} = (d^{\mu})^3 \cdot \left[\sum_{\nu} N_b^{\nu} \cdot (d^{\nu})^3 \right]^{-1} \tag{29}$$

with n_v^{μ} the number of valence electrons per μ bond, and v_b^{μ} the bond volume.

A special note for Levine's theory is that the heteropolar part C in an A_mB_n crystal is different and is adjusted as:

$$C^{\mu} = 14.4 \cdot b^{\mu} \cdot \left(Z_A^{\mu} - \frac{n}{m} \cdot Z_B^{\mu} \right) \cdot e^{(-k_s \cdot r_0^{\mu})} / r_0^{\mu} \quad (n > m) \tag{30}$$

$$C^{\mu} = 14.4 \cdot b^{\mu} \cdot \left(\frac{m}{n} \cdot Z_A^{\mu} - Z_B^{\mu} \right) \cdot e^{(-k_s \cdot r_0^{\mu})} / r_0^{\mu} \quad (n < m) \tag{31}$$

where $r_0^{\mu} = (r_A + r_B)/2$, and the value of b^{μ} is correlated with the average coordination number N_c^{μ}:

$$N_c^{\mu} = \frac{m}{m+n} N_{CA}^{\mu} + \frac{n}{m+n} N_{CB}^{\mu} \tag{32}$$

$$b^{\mu} = 0.089 \cdot (N_c^{\mu})^2 \tag{33}$$

Therefore, Levine's modification expanded the application of P–V theory to A_mB_n binary systems. Although it is still not practical for more complex multi-systems, the idea of decomposing the macro-properties into individual bonds is beneficial for future work.

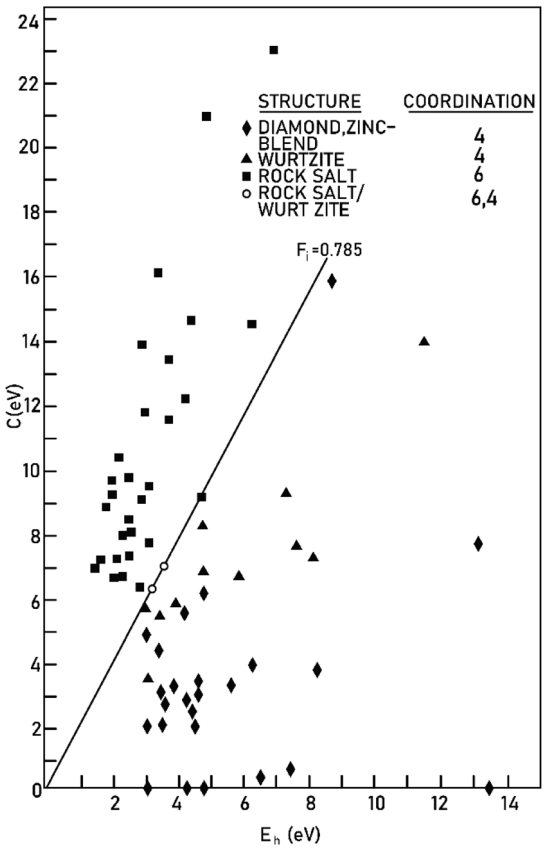

Fig. 2 The separation of four-fold and six-fold coordinated structures, using the spectroscopically defined covalent and ionic energy gaps E_h and C, respectively (reprinted with permission from ref. 41. Copyright 2020 American Physical Society) (http://dx.doi.org/10.1103/RevModPhys.42.317).

3. Binary bonding formula theory of complex polycrystals

In the process of materials research, compositions of materials are generally not confined to binary systems. For instance, high-entropy alloys, usually formed of five or more equal or approximately equal metals, have excellent properties in hardness, high temperature resistance, corrosion resistance, and wear resistance.[70] In the MWDC field, the ionic modification is usually based on a ternary system as well, such as Bi_2O_3–TiO_2–V_2O_5,[71] ZnO–TiO_2–Nb_2O_5,[72] or BaO–MgO–Nb_2O_5[73] systems. It is important to have a better understanding of the impact of chemical bond features on crystal structure. Therefore, P–V–L bond theory should be appropriately adjusted for a good fit with multi-systems.

The composition of a crystal can be expressed by the chemical molecular formula, which represents the atomic ratio among various chemical elements that constitute the crystal. However, the expression does not correspond to the spatial configuration in the specific crystal structure. On the other hand, the crystal can also be regarded as the aggregation of various ions and chemical bonds between ions. If the two ions that compose the chemical bond sharing the same symmetrical positions in a crystal and bond length are classified as the same type of bond, then this type of bond with the same specific properties, spatial configuration, and proportion of elements is called a binary bonding formula. Since more than one type of bond exists in a crystal, each kind of bond corresponds to a unique binary bonding formula. The crystal is the aggregation of various types of chemical bonds, so that the molecular formula of the crystal should also be the sum of the binary bonding formulas. Hence, one can deal with the binary bonding formula with P–V–L bond theory to obtain bond features. Once the proportional relationship between the binary bonding formula and complex multi-element crystal formula has been built, the purpose of dealing with the complex polycrystalline system is realized. Briefly speaking, the key idea is to convert the chemical formula of a complex polycrystal into a combination of binary bonding formulas.

Zhang developed the method for decomposing complex polycrystals into the binary bonding formula of a crystal when the crystal structure, coordination environment and element proportion in the crystal formula have been determined.

Suppose that the molecular formula of any complex crystal is:[62,74]

$$\mathrm{A}^1_{a1}\mathrm{A}^2_{a2}\mathrm{A}^3_{a3}\ldots\mathrm{A}^i_{aj}\mathrm{B}^1_{b1}\mathrm{B}^2_{b2}\mathrm{B}^3_{b3}\ldots\mathrm{B}^j_{bj}=\sum_{ij}\mathrm{A}^i_{mi}\mathrm{B}^j_{nj} \tag{34}$$

where A and B refer to cations and anions, respectively, A^i and B^j symbolise different elements or symmetry positions of equivalent elements, a_i and b_j indicate the number of elements. Correspondingly, the binary bonding formula of any type of A–B bond can be resolved under the conditions of given coordination numbers $N_{\mathrm{CA}i}$ and $N_{\mathrm{CB}j}$:

$$\frac{N(\mathrm{B}^j-\mathrm{A}^i)a_i}{N_{\mathrm{CA}i}}\cdot\mathrm{A}^i\cdot\frac{N(\mathrm{A}^i-\mathrm{B}^j)b_j}{N_{\mathrm{CB}j}}\cdot\mathrm{B}^j \tag{35}$$

$$m^i=\frac{N(\mathrm{B}^j-\mathrm{A}^i)a_i}{N_{\mathrm{CA}i}} \tag{36}$$

$$n^j=\frac{N(\mathrm{A}^i-\mathrm{B}^j)b_j}{N_{\mathrm{CB}j}} \tag{37}$$

where $N(\mathrm{B}^j-\mathrm{A}^i)$ is the number of A^i cations in the ligand of the B^j ion, and $N(\mathrm{A}^i-\mathrm{B}^j)$ is the number of B^j cations in the ligand of the A^i ion. The binary bonding formula should be electrically neutral like the crystal, and the same ion shows different valence states in different bonding formulas. Therefore, it is crucial to determine the effective valence electron number of the ion in the specific bonding formula.

Suppose that A and B ions in any μ bond present valences of P^μ(A–B) and P^μ(B–A), the following equation is expected:

$$\frac{P^\mu(\mathrm{A}-\mathrm{B})\cdot N(\mathrm{B}-\mathrm{A})\cdot a}{N_{\mathrm{CA}}}=\frac{P^\mu(\mathrm{B}-\mathrm{A})\cdot N(\mathrm{A}-\mathrm{B})\cdot b}{N_{\mathrm{CB}}} \tag{38}$$

The effective charges q^μ_{A} and q^μ_{B} of A and B ions are calculated as:

$$q^\mu_{\mathrm{A}}=\frac{P^\mu(\mathrm{A}-\mathrm{B})\cdot N_{\mathrm{CA}}}{\sum_\mu P^\mu(\mathrm{A}-\mathrm{B})\cdot N^\mu(\mathrm{B}-\mathrm{A})} \tag{39}$$

$$q^\mu_{\mathrm{B}}=\frac{P^\mu(\mathrm{B}-\mathrm{A})\cdot N_{\mathrm{CB}}}{\sum_\mu P^\mu(\mathrm{B}-\mathrm{A})\cdot N^\mu(\mathrm{A}-\mathrm{B})} \tag{40}$$

Therefore, the valence electron numbers Z_{A} and Z_{B} values in P–V–L bond theory should be adjusted as effective valence electron numbers $(Z_{\mathrm{A}})^*$ and $(Z_{\mathrm{B}})^*$:[75]

$$(Z_{\mathrm{A}})*=Z_{\mathrm{A}}\cdot q^\mu_{\mathrm{A}} \tag{41}$$

$$(Z_{\mathrm{B}})*=Z_{\mathrm{B}}\cdot q^\mu_{\mathrm{B}} \tag{42}$$

Combining P–V–L bond theory and the binary bonding formula expression, crucial fundamental bond parameters could be achieved, and two key indicators of MWDC, dielectric polarization ε_{r} and $Q\times f$ value, could be discussed. Starting from the crystal structure configuration, one can calculate the detailed bond volume v^μ_{b} using crystal structure parameters from the ICSD database or Rietveld refinement results. Combined with the coordinate environment and valence electrons of atoms, the parameter for the number of valence electrons of a μ bond, N^μ_{e}, could be obtained, and finally the bond ionicity f_{i}, bond covalency f_{c} and bond susceptibility χ could be specially assigned, which is helpful in discussing dielectric polarization. Furthermore, lattice energy U presents the binding ability between ions, where a high U value stands for a stable structure, and the internal loss caused by anharmonic vibration would be reduced. For MWDC, it reflects the internal dielectric loss $\tan\delta$ ($Q=1/\tan\delta$, f is the resonant frequency),

which is closely corelated with the $Q \times f$ value. As mentioned, there is no 100% ionic chemical bond in a crystal; therefore, the ionic part of a chemical bond's contribution to lattice energy U_{bi} and the covalent part of contribution U_{bc} should be considered. The lattice energy U is calculated as follows:[68]

$$U_{total} = \sum U_b^{\mu} \quad (43)$$

$$U_b^{\mu} = \sum (U_{bi}^{\mu} + U_{bc}^{\mu}) \quad (44)$$

$$U_{bi}^{\mu} = 1270 \cdot \frac{(m+n) \cdot Z_+^{\mu} Z_-^{\mu}}{d^{\mu}} \left(1 - \frac{0.4}{d^{\mu}}\right) f_i^{\mu} \quad (45)$$

$$U_{bc}^{\mu} = 2100\,\mathrm{m} \cdot \frac{(Z_+^{\mu})^{1.64}}{(d^{\mu})^{0.75}} f_c^{\mu} \quad (46)$$

where Z_+^{μ} and Z_-^{μ} are the valence states of the cation and anion, d^{μ} is the bond length, and the m/n value is obtained from the binary bonding formula.

4. Usage of P–V–L bond theory in dielectric ceramics

As mentioned above, much attention has been paid to the application of P–V–L bond theory in the MWDC field in recent years because investigations of chemical bond parameters are instrumental in studying structural features, and then providing the basis for ionic doping modification and the design of novel materials, which is helpful for understanding microwave dielectric properties. Up to now, several ceramic systems with excellent dielectric performances have been developed, as listed in Table 2.[13,76–95] In this section, current studies of applying P–V–L bond theory in the MWDC field with regard to structural-property investigations are summarized.

4.1 Monoclinic clinopyroxene-type

Clinopyroxene-type ABC_2O_6 (A = Ca; B = Co, Mg, Zn, Fe; C=Si, Ge) materials are crystallized as a monoclinic structure with a $C2/c$ space group.[96–98] Huber found out that the petedunnite $CaZnSi_2O_6$ phase stabilizes at $P > 0.8$ GPa; otherwise, it decomposes into Zn_2SiO_4, $Ca_2ZnSi_2O_7$ and SiO_2 if the pressure is low and temperature exceeds 650 °C.[99] Distortions of the polyhedra were quantitatively analysed by Heuer in a $CaBSi_2O_6$ system (B = Fe, Zn).[96] Recently, microwave dielectric properties of $CaBSi_2O_6$ (B = Co, Mg) were reported: ε_r = 6.04, $Q \times f$ = 12 457 GHz, and τ_f = −18.91 ppm per °C for B = Co,[100] sintered at 1175 °C; and ε_r = 7.46, $Q \times f$ = 59 638 GHz, and τ_f = −46 ppm per °C for B = Mg,[101] sintered at 1290 °C. $CaMgSi_2O_6$ ceramics are suitable candidates for electronic circuit packaging and microwave substrates as a result of their low ε_r value and low dielectric loss. Therefore, a number of studies focus on improving its dielectric properties and reducing its sintering temperature to lower than 950 °C to make it applicable in low-temperature cofired ceramic (LTCC) technology: *e.g.* if Mn^{2+}, Co^{2+}, Zn^{2+}, Cu^{2+}, $(Mn_{1/2}Zn_{1/2})^{2+}$ cations are used to partially substitute for Mg sites,[102–105] improvements in $Q \times f$ value could be achieved: an ε_r of 8.01, a $Q \times f$ of about 83 469 GHz, and a τ_f of *ca.* −45.27 ppm per °C for $CaMg_{0.98}Mn_{0.02}Si_2O_6$. In the $CaMg_{0.96}Cu_{0.04}Si_2O_6$ system: ε_r = 7.41, $Q \times f$ = 160 100 GHz, and τ_f = −42 ppm per °C. Furthermore, sintering aids, such as Li_2O–MgO–ZnO–B_2O_3–SiO_2, LiF, and Li_2CO_3–V_2O_5, were used to decrease the sintering temperature of $CaMgSi_2O_6$ ceramics, where it was effectively reduced from 1300 °C to 900 °C using 15 wt% Li_2O–MgO–ZnO–B_2O_3–SiO_2 with great microwave dielectric performances: ε_r = 8.2, $Q \times f$ = 32 000 GHz, and τ_f = −48 ppm per °C.[106]

The schematic monoclinic crystal structure of $CaMgSi_2O_6$ can be seen in Fig. 3(a) and (b). A phase transition takes place between $C2/c$ and $P2_1/c$ when the arrangements of tetrahedral

Table 2 Representative microwave dielectric ceramic systems with different dielectric constants

Material systems	ST (°C)	ε_r	$Q \times f$ (GHz)	τ_f (ppm per °C)	Ref.
Mg_2SiO_4	1450	6.8	270 000	−60	76
Al_2O_3	1550	10.0	333 000	−60	77
$0.75MgAl_2O_4$–$0.25TiO_2$	1400–1460	11.0	105 400	−12	78
$Mg_4(TaNb_{0.975}V_{0.025})O_9$	1200	12.0	200 000	−73	79
$MgWO_4$	1150	13.1	69 000	−58	80
Mg_2TiO_4	1500	14.2	160 000		81
$NdNbO_4$	1250	19.6	33 000	−24	82
$0.95MgTiO_3$–$0.05CaTiO_3$	1400	20.0	56 000	0	83
$(Zn_{0.7}Mg_{0.3})TiO_3$	950	22.0	65 000	−80	84
$Ba(Mg_{1/3}Ta_{2/3})O_3$	1640	24.0	430 000	5	85
$0.9LaAlO_3$–$0.1SrTiO_3$	1680	26.7	139 000	−50	86
$Zn_{1.01}Nb_2O_6/TiO_2/Zn_{1.01}Nb_2O_6$	1200	26.8	99 500	0.5	87
$La(Mg_{1/2}Ti_{1/2})O_3$	1650	29.0	114 000	−81	88
$ZnTiNb_2O_8$	1250	34.0	42 500	−52	89
$BaTi_4O_9$	1250	36.0	50 470	16	13
$Ba_2Ti_9O_{20}$	1300	37.0	57 000	−6	13
$Zr_{0.8}Sn_{0.2}TiO_4$	1600	38.9	51 500	0.7	90
$Ba_5Nb_4O_{15}$	1380	39.0	23 700	78	91
$CaLa_4Ti_4O_{15}$	1550	41.1	50 240	−25	92
$0.76ZrTiO_4$–$0.24ZnNb_2O_6$	1260–1300	47.0	34 000	0	93
$Li_{0.95}Nb_{0.45}Ti_{0.7}O_3$	1100	56.2	8350	15	94
BaO–Sm_2O_3–TiO_2	1300–1450	74.0	12 000	10	95

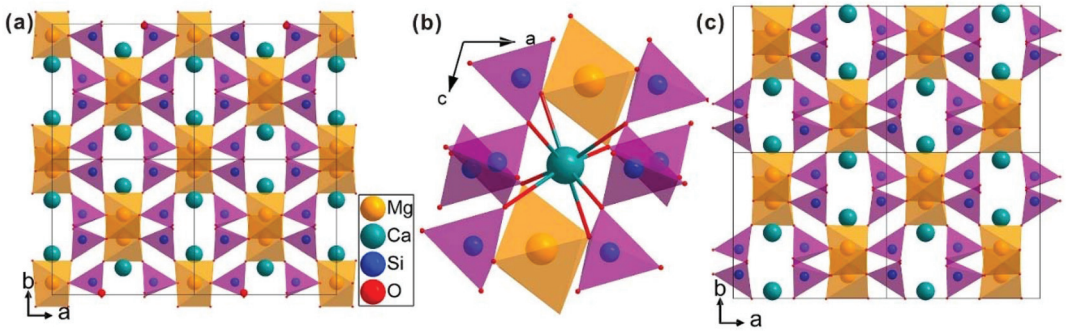

Fig. 3 $CaMgSi_2O_6$ crystal structure with different phases and Ca-clusters: (a) the *C*2/*c* structure patterns, (b) a cluster of eight-fold coordinated Ca polyhedra, (c) the $P2_1/c$ structure (reprinted with permission from ref. 104. Copyright 2019 Elsevier).

$[SiO_4]$ frameworks change, as indicated in Fig. 3(c).[104] Structural parameters of the monoclinic phase reported by Thompson (COD #1000007) are:[107] lattice parameters of a = 9.7397 Å, b = 8.9174 Å, c = 5.2503 Å, $\alpha = \gamma = 90°$, β = 105.866°, and V_{cell} = 438.631 Å.^{3} In its structure, atoms of Mg and Ca occupy the 4e Wyckoff position while Si and O (three types of O: O1, O2 and O3) atoms are in the 8f site. The structure is built from three types of oxygen polyhedra, where the Ca cation is eight-fold coordinated, forming a $[CaO_8]$ dodecahedron, the Mg cation is coordinated with six oxygen anions and forms an $[MgO_6]$ octahedron, and the Si cation is surrounded by four oxygen anions and tetrahedral $[SiO_4]$ is constructed. Specifically, Ca–O1 × 2, Ca–O2 × 2, Ca–O3(1) × 2 and Ca–O3(2) × 2 bonds appear in the $[CaO_8]$ dodecahedron. While the Mg cation coordinates with O1 and O2 anions, in which four Mg–O1 bonds and two Mg–O2 bonds exist: Mg–O1(1) × 2, Mg–O1(1) × 2 and Mg–O1(1) × 2 bonds. Si–O1, Si–O2 and Si–O3(1) and Si–O3(2) exist in an $[SiO_4]$ tetrahedron. Based on the crystal structure and coordination environments of ceramic $CaMgSi_2O_6$, the binary bonding formula was considered first:

$$\begin{aligned} CaMgSi_2O_6 = {} & Ca_{1/4}O1_{1/2} + Ca_{1/4}O2_{2/3} + Ca_{1/4}O3(1)_{1/2} \\ & + Ca_{1/4}O3(2)_{1/2} + Mg_{1/3}O1(1)_{1/2} + Mg_{1/3}O1(2)_{1/2} \\ & + Mg_{1/3}O2_{2/3} + Si_{1/2}O1_{1/2} + Si_{1/2}O2_{2/3} + Si_{1/2}O3(1)_{1/2} \\ & + Si_{1/2}O3(2)_{1/2} \end{aligned}$$

For cations, the effective valence electronic numbers are Z_{Ca} = 2, Z_{Mg} = 2, and Z_{Si} = 4, respectively, while the Z_o value of O^{2-} anion depends on the electric neutrality in any chemical bond, which differs along with the bonding formula. For instance, Z_o equals 3, 9/4 and 3 in Ca–O1, Ca–O2 and Ca–O3 bonds.

Ohsato reported that silicates presenting with low ε_r values, such as forsterite Mg_2SiO_4 ($\varepsilon_r \sim 6.8$) and willemite Zn_2SiO_4 ($\varepsilon_r \sim 6.6$), are caused by the large covalency of the $[SiO_4]$ tetrahedral framework.[108] In a $CaMgSi_2O_6$ ceramic, average chemical bond covalency (Af_c) values quantitatively calculated by Li are sequenced in descending order:[102] $Af_{c(Si-O)}$ = 35.55% > $Af_{c(Mg-O)}$ = 29.97% > $Af_{c(Ca-O)}$ = 16.50%, supporting the Si–O bond having a large bond covalency. Meanwhile, one can compare the contributions of chemical bonds to bond susceptibility χ to judge the dominant source of dielectric polarization. The bond susceptibility χ value calculated *via* their chemical bond parameters, can be seen in Table 1S in ESI,† where the contribution from Si–O bonds reaches approximately 66%, while Ca–O and Mg–O bonds provide small contributions of about 14% and 20%. This conclusion indicates that Si–O bonds play leading roles in dielectric polarizability. The calculated lattice energy U_{total} of the $CaMgSi_2O_6$ system is as large as 39645 kJ mol^{-1}, where Si–O bonds contribute 85% (33 627 kJ mol^{-1}), which is 6 times the total lattice energy of Ca–O and Mg–O bonds. Reported with same crystal structure, a $CaCoSi_2O_6$ ceramic with a U_{total} value (19899 kJ mol^{-1}) shows a $Q \times f$ value of about 12 457 GHz, which is smaller than that of $CaMgSi_2O_6$ (59 638 GHz) and also indicates the importance of structural stability to dielectric loss.[100]

To improve microwave dielectric performances, bivalent Mn^{2+} cations have been used to partially replace Mg sites in Ca$(Mg_{1-x}Mn_x)Si_2O_6$, and a solid solution forms in the region of x = 0–0.08, as shown in Fig. 4.[102] The introduction of the Mn

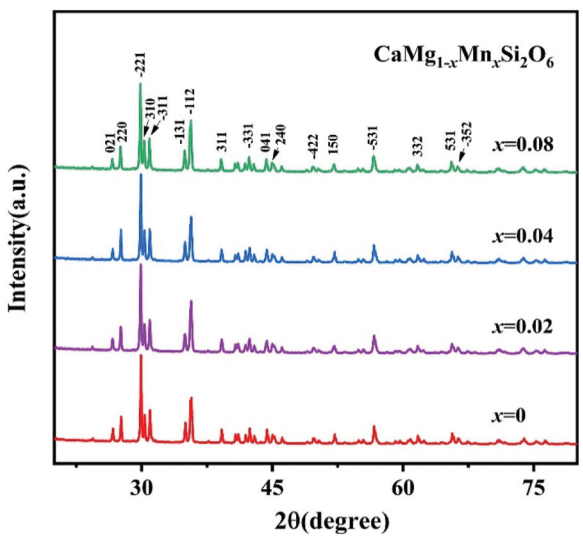

Fig. 4 The XRD patterns of $CaMg_{1-x}Mn_xSi_2O_6$ (x = 0–0.08) ceramics sintered at 1300 °C (reprinted with permission from ref. 102. Copyright 2019 Elsevier).

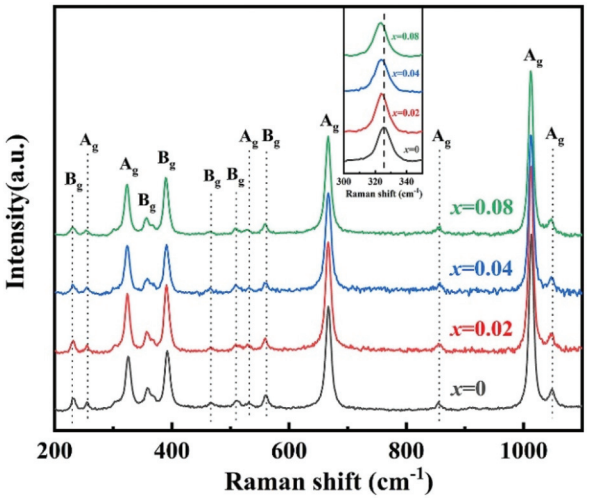

Fig. 5 The Raman spectra of $CaMg_{1-x}Mn_xSi_2O_6$ (x = 0–0.08) ceramics (reprinted with permission from ref. 102. Copyright 2019 Elsevier).

element leads to an increase in the average bond covalency f_c value, where the f_c value for Si–O bonds is still as large as 32%, resulting in an increasing trend in ionic polarizability based on the Clausius–Mossotti equation. Thus, the ε_r value increases monotonously. The increase in U_{total} suggests an enhancement in structural stability. The reported Raman spectra in Fig. 5 also show the most intense peak around 1011 cm^{-1}, which is caused by O–Si–O stretching vibration, which dominates the Raman-active vibration. On the other hand, by using the far-infrared reflectivity spectrum and obtaining the complex dielectric function by the Kramers–Kronig relationship, the intrinsic dielectric properties were acquired *via* a three-parameter classical harmonic oscillator model. The results indicate that the Mn^{2+} cation increases the ε_r value and decreases the dielectric loss (x = 0.02, $Q \times f$ = 83 469 GHz), also reflects the improvement in structural stability of $Ca(Mg_{0.98}Mn_{0.02})Si_2O_6$.

4.2 Tetragonal akermanite and monoclinic melilite-type

4.2.1 Tetragonal $A_2BSi_2O_7$ structure. Based on a calculation of monoclinic $CaMgSi_2O_6$ ceramic, it is determined that Si–O bonds have the largest bond covalencies and play leading roles in dielectric polarization and crystal structural stability. However, it is not appropriate to jump to the conclusion that the f_c value of the Si–O bond is the largest in all silicates according to P–V–L bond theory. Because for a specific crystal, such as a silicate structure, [MO_4] (such as M = Co, Mg, Zn, Mn) and [SiO_4] tetrahedral configurations coexist in tetragonal akermanite $Sr_2MSi_2O_7$ compared with the existence of [MgO_6] and [SiO_4] frameworks in $CaMgSi_2O_6$, where the coordinate environments obviously change.[109] Therefore, careful considerations should be taken into account.

A tetragonal akermanite-type $A_2BSi_2O_7$ structure with a space group of $P\bar{4}21m$(113) usually exists in $A_2BSi_2O_7$ (A = Sr, Ca; B = Mg, Zn, Co, Mn) systems. It has attracted public attention for it broad application prospects, such as lighting, display, photoelectric conversion, optoelectronic information, and biomolecular identification. Moreover, its excellent dielectric properties[109] ($Sr_2MgSi_2O_7$: ε_r = 8.3, $Q \times f$ = 55 000 GHz, and τ_f = −47.5 ppm per °C; $Sr_2MnSi_2O_7$: ε_r = 8.8, $Q \times f$ = 32 000 GHz, and τ_f = −58.5 ppm per °C; $Ca_2ZnSi_2O_7$: ε_r = 11.0, $Q \times f$ = 13 500 GHz, and τ_f = −64.3 ppm per °C) also indicate their huge potential in the microwave communication field. Recently, Xiao investigated the structural effects of a tetragonal $Sr_2MgSi_2O_7$ microwave dielectric ceramic *via* P–V–L bond theory, providing an insight into the structural properties of tetragonal silicates.[110] According to the tetragonal structure of $Sr_2MgSi_2O_7$ reported by Endo (COD #4317123),[111] as can be seen from Fig. 6, the Sr^{2+} cation is surrounded by eight O^{2-} anions, and Mg/Zn^{2+} and Si^{4+} cations are four-fold coordinated. An [MgO_4] tetrahedron connects with an [SiO_4] tetrahedron sharing a vertex (O3), while the [SiO_4] framework interconnects through shared vertices (O1). The structural detail is listed in Table 3. Therefore, the binary bonding formula is expressed as:

$$Sr_2MgSi_2O_7 = Sr_{1/4}O1(1)_{1/2} + Sr_{1/2}O2(1)_1 + Sr_{1/4}O2(2)_{1/2} + Sr_{1/2}O3(1)_1 + Sr_{1/2}O3(2)_1 + Mg_1O3_1 + Si_{1/2}O1_{1/2} + Si_{1/2}O2_{1/2} + Si_1O3_1$$

To make comparisons of bond features in tetragonal phases, a representative $A_2BSi_2O_7$ (A = Sr, Ca; B = Mg, Mn) with both reported structural details[111,112] and microwave dielectric performances (a $Ca_2MgSi_2O_7$ ceramic is not used as a comparison here due to the fact that secondary phase SiO_2 exists along with the $Ca_2MgSi_2O_7$ phase[113]) is chosen. Detailed comparisons of bond parameters can be found in Table 2S in ESI.†

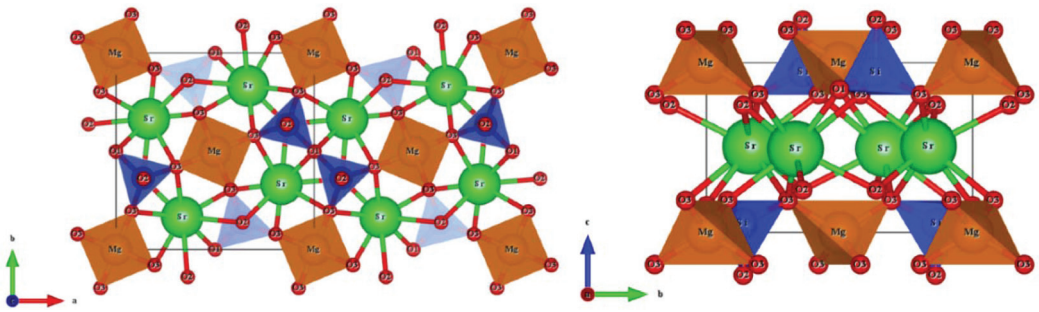

Fig. 6 Diagrammatic sketch of a tetragonal $Sr_2MgSi_2O_7$ crystal structure.

Table 3 Structural parameters of tetragonal $Sr_2MgSi_2O_7$ with a space group of $P\bar{4}21m$, where the lattice parameters are: $a = b = 8.011$ Å, $c = 5.164$ Å, $\alpha = \beta = \gamma = 90°$ and $V_{cell} = 331.355$ Å^3

		Fractional coordinates			
Atom	Position	x	y	z	Occ
Sr	4e	0.3341	0.1659	0.5074	1.0
Mg	2a	0.0000	0.0000	0.0000	1.0
Si	4e	0.1353	0.3647	0.9458	1.0
O1	2c	0.5000	0.0000	0.1580	1.0
O2	4e	0.1384	0.3616	0.2506	1.0
O3	8f	0.0788	0.1947	0.8111	1.0
Bond length (Å)	[SrO_8]: Sr–O1 × 1: 2.6050; Sr–O2(1) × 2: 2.7480; Sr–O2(2) × 1: 2.5830; Sr–O3(1) × 2: 2.7920; Sr–O3(2) × 2: 2.5870 [MgO_4]: Mg–O3 × 4: 1.9450 [SiO_4]: Si–O1 × 1: 1.6240; Si–O2 × 1: 1.5740; Si–O3 × 2: 1.5950				

Table 4 shows the average bond ionicity, lattice energy and proportion of bond susceptibility of T-type $A_2BSi_2O_7$ (A = Sr, Ca; B = Mg, Mn) structures. The variations in bond covalencies f_c are not similar to those in $CaMgSi_2O_6$, where the largest average bond covalencies are revealed in B–O bonds (46%–48%), followed by those in Si–O bonds and then A–O bonds. This different situation is possibly caused by the coordination environments of the B cation. However, based on the U_{total} and χ values, specifically, the U value of Si–O bonds drops from 34 891 to 34347.kJ mol^{-1} (the U_{total} for all bonds still decreases), which illustrates that $Sr_2MgSi_2O_7$ is intrinsically more stable than the $Ca_2ZnSi_2O_7$ structure. Although the actual $Q \times f$ value is also affected by external loss, such as densification, grain growth, and sintering process. The higher lattice stability explains the lower intrinsic dielectric loss. The proportion of Si–O bond susceptibility shows an increasing trend from 47.26% to 51.72%, corresponding to the increase in ε_r value from 8.3 to 11.0, suggesting the importance of Si–O bonds in dielectric polarizability.

Hanuza reported the Raman and IR spectra of $A_2BSi_2O_7$ (A = Sr, Ca; B = Mg, Zn) and calculated vibrational modes through lattice dynamic calculation,[114] where the most intense and sharp Raman peaks around 901 cm^{-1}, 650 cm^{-1} and 615 cm^{-1}, are attributed to the symmetric stretching modes of the SiO_3 groups, symmetric stretching modes of the Si^OSi (where O refers to the bridging oxygen), and bending modes of SiO_3 groups. IR spectra of $Ca_2ZnSi_2O_7$ show that the largest oscillator strength $\Delta\varepsilon$ (1.497) originates from the E mode, which is determined by the bending mode of $\delta(Si^OSi)$, the bending mode of the SiO_3 group $\delta(SiO_3)$ and the symmetric stretching mode of [CaO8] T′(Ca^{2+}). This result also show that Si–O bonds are important for intrinsic dielectric properties.

Table 4 Average bond ionicity Af_i value, total lattice energy U_{total} and proportion of bond susceptibility $\chi/\sum\chi$ of T-type $A_2BSi_2O_7$ (A = Sr, Ca; B = Mg, Mn, Zn) structures

Structure	Bond type	Af_i (%)	U_{total} (kJ mol^{-1})	$\chi/\sum\chi$ (%)
$Sr_2MgSi_2O_7$	Sr–O	85.75	5042	22.42
	Mg–O	47.99	4058	30.32
	Si–O	65.44	34 891	47.26
$Sr_2MnSi_2O_7$	Sr–O	85.81	5025	22.39
	Mn–O	48.69	3910	30.33
	Si–O	65.55	34 859	47.27
$Ca_2ZnSi_2O_7$	Ca–O	85.57	5166	22.40
	Zn–O	47.00	4271	25.88
	Si–O	65.66	34 347	51.72

In $A_2BSi_2O_7$ structures, it is found that although Si–O bonds do not show the largest bond covalency value, they still play an indispensable role in structural stability and dielectric polarization.

4.2.2 Monoclinic $A_2BSi_2O_7$ and $AB_2Si_2O_7$ structures. Monoclinic melilite-type structure silicate compounds can be found in $A_2BSi_2O_7$ (A = Ba; B = Co, Zn, Cu, Mg) and $AB_2Si_2O_7$ (A = Ba; B = Co, Zn) systems. However, structural diversities appear in $Ba_2ZnSi_2O_7$ and $BaCo_2Si_2O_7$ crystal structures. This phenomenon is caused by the different arrangements of the tetrahedral framework, as sketched in Fig. 7,[115] [SiO_4] interconnects with [ZnO_4] in the a–c plane in $Ba_2ZnSi_2O_7$, while [CoO_4] connects with [SiO_4] in the a–b plane. The structural details and bond parameters of $Ba_2ZnSi_2O_7$ can be obtained using COD #8100589 reported by Kaiser.[116] Song investigated the bond features in the $BaCo_2Si_2O_7$ system through P–V–L bond theory.[115] Due to the different coordination environments in $Ba_2ZnSi_2O_7$ and $BaCo_2Si_2O_7$ systems, as can be seen in Tables 3S and 4S in ESI,† the binary bonding formulas show large differences:

$$\begin{aligned}Ba_2ZnSi_2O_7 = {} & Ba_{1/4}O1(1)_{1/2} + Ba_{1/4}O1(2)_{1/2} + Ba_{1/4}O1(3)_{1/2} \\ & + Ba_{1/4}O2(1)_{1/2} + Ba_{1/4}O2(2)_{1/2} + Ba_{1/4}O3(1)_{1/2} \\ & + Ba_{1/4}O3(2)_{1/2} + Ba_{1/4}O4_{1/2} + Zn_{1/2}O2_{1/2} + Zn_{1/2}O3_{1/2} \\ & + Si_{1/2}O1_{1/2} + Si_{1/2}O2_{1/2} + Si_{1/2}O3_{1/2} + Si_{1/2}O4_{1/2}\end{aligned}$$

$$\begin{aligned}BaCo_2Si_2O_7 = {} & Ba_{1/8}O2(1)_{1/4} + Ba_{1/8}O2(2)_{1/4} + Ba_{1/8}O3_{1/3} \\ & + Ba_{1/8}O4_{1/4} + Ba_{1/8}O5_{1/3} + Ba_{1/8}O6_{1/3} + Ba_{1/8}O7(1)_{1/4} \\ & + Ba_{1/8}O7(2)_{1/4} + Co1_{1/4}O4_{1/4} + Co1_{1/4}O6_{1/3} \\ & + Co2_{1/4}O1_{1/3} + Co2_{1/4}O2_{1/4} + Co3_{1/4}O1_{1/3} \\ & + Co3_{1/4}O3_{1/3} + Co3_{1/4}O4_{1/4} + Co3_{1/4}O7_{1/4} + Si1_{1/4}O1_{1/3} \\ & + Si_{1/4}O2_{1/4} + Si1_{1/4}O5_{1/3} + Si1_{1/4}O6_{1/3} + Si_{1/4}O7_{1/4} \\ & + Si2_{1/4}O3_{1/3} + Si2_{1/4}O4_{1/4} + Si2_{1/4}O5_{1/3}\end{aligned}$$

After comparing the bond parameters of $Ba_2ZnSi_2O_7$ from Table 5S in ESI,† and $BaCo_2Si_2O_7$ from ref. 115 in Table 5,

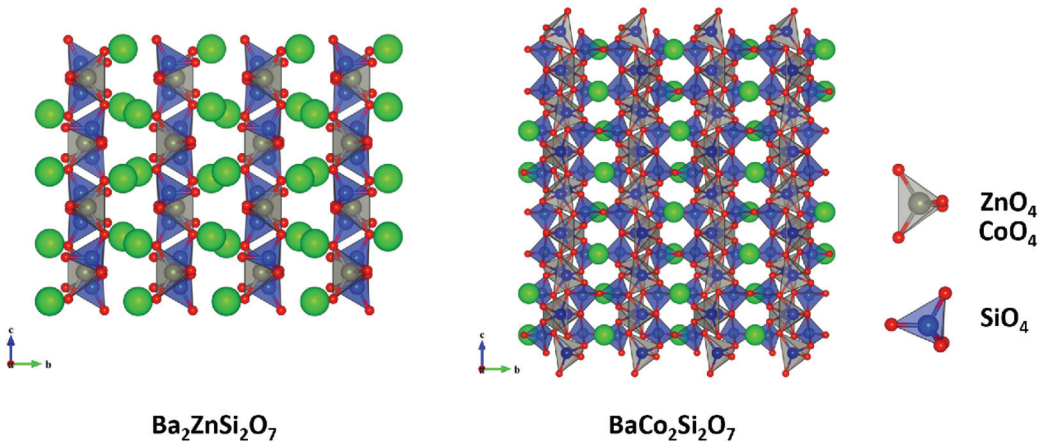

Fig. 7 Crystal structure of $Ba_2ZnSi_2O_7$ and $BaCo_2Si_2O_7$.

Table 5 Average bond ionicity Af_i value, total lattice energy U_{total} and microwave properties of M-type $Ba_2ZnSi_2O_7$ and $BaCo_2Si_2O_7$

Structure	Bond type	Af_i (%)	U_{total} (kJ mol^{-1})	Properties
$Ba_2ZnSi_2O_7$	Ba–O	85.35	4851	ε_r = 8.8
	Zn–O	46.90	4033	$Q \times f$ = 34 000 GHz
	Si–O	64.55	34 326	
$BaCo_2Si_2O_7$	Ba–O	83.65	2331	ε_r = 9.3
	Co–O	44.94	7644	$Q \times f$ = 31 000 GHz
	Si–O	59.75	33 088	

similar conclusions can be drawn as in the tetragonal akermanite structure that although the Si–O bond does not have the largest bond covalency, its contribution to lattice energy and bond susceptibility still determines its importance in dielectric polarization and lattice stability.

4.3 Rock salt structure

Driven by the requirements for high reliability and high-frequency applications, the pursuit of novel material systems with low ε_r value and ultra-high $Q \times f$ ($Q \times f \geq 100\,000$ GHz) value has been underway. Li_2O–AO–BO_2 based systems can be regarded as the substitution of the A site in AO (A = Mg, Zn, Ni) with Li_2BO_3 (B = Ti, Sn, Zr). For example, Li_2TiO_3 and MgO are subordinated to the same rock-salt-type structure, and the ionic radii of cations are close to each other ($IR_{Li,Ti}$ = 0.708 Å, IR_{Mg} = 0.72 Å),[117] which is beneficial for forming a solid solution. Therefore, material systems with the chemical formula of $Li_{2x}A_{1-x}B_xO_{1+2x}$ (A = Mg, Zn, Ni; B = Ti, Sn, Zr)[118,119] show large diversities as x varies. For instance, x = 1/5: $Li_2Mg_4TiO_7$,[120] x = 1/4: $Li_2Mg_3TiO_6$,[121] x = 2/5: $Li_4Mg_3Ti_2O_9$[122] and x = 1/2: Li_2MgTiO_4.[123] In 2016, novel rock-salt ceramics with the chemical formula of Li_2O–3MgO–TiO_2 (B = Ti, Sn, Zr) ceramics possess excellent microwave dielectric performances: ε_r = 8.8–15.2, $Q \times f$ = 86 000–152 000 GHz (f = 8.3–10.7 GHz).[124] Besides, the raw materials are cheap and easy to obtain, attracting a lot of public attention. However, it is noticed that the sintering characteristics are not satisfactory. For instance, the secondary-phase Mg_2SnO_4 exists along with the formation of the $Li_2Mg_3SnO_6$ phase,[125] ZrO_2 usually accompanies the existence of the $Li_2Mg_3ZrO_6$ phase.[124] Most importantly, a large number of micropores formed by the volatilization of lithium at high temperature lead to cracks or fractures in the microstructure, which is detrimental to the development of properties. Therefore, it is crucial to solve these fundamental and nonnegligible issues.

The volatilization of lithium can be compensated by burying the $Li_2Mg_3BO_6$ (B = Ti, Sn, Zr) green pellets in sacrificial powders of the same composition, which improves the sintering densification and acquiring the pure phase.[126] A non-stoichiometric ratio of the lithium of $Li_{2(1+x)}Mg_3ZrO_6$ partially inhibits ZrO_2 and impurities, achieving a $Q \times f$ value as high as 307319 GHz.[127] By using a novel atmosphere-controlled sintering process, where ZrO_2 powder provides a protective atmosphere, and Li_2CO_3 powder provides an Li-rich sintering atmosphere, $Li_{2(1+x)}Mg_3SnO_6$ ceramics with very dense microstructures were achieved.[125,128] Therefore, it is reasonable to discuss the structural–property relationship when the external loss caused by the fabrication process and sintering characteristics is controlled.

4.3.1 Variation of ionic occupancy in cubic $Li_{2x}Mg_{1-x}Ti_xO_{1+2x}$ (x = 1/4, 2/5 and 1/2) systems. $Li_{2x}Mg_{1-x}Ti_xO_{1+2x}$ (x = 1/4, 2/5 and 1/2) systems belong to a rock-salt cubic structure with an $Fm3m$(225) space group. A schematic diagram of the crystal structure is presented in Fig. 8, where the Li/Mg/Ti atoms are randomly distributed in the 4a Wyckoff position, and one type of O atom is in the 4b site. All the cations are six coordinated, forming an [MO_6] octahedron (M = Li/Mg/Ti).

It is interesting to note that the above-mentioned systems share the same crystal structure, spatial configuration, coordinate environments and distribution of valence states. While the only difference lies in ionic occupancy, which directly leads to variations in $N(B^j - A^i)$ and A_mB_n expression. Therefore, it is necessary to discover the impact of ionic occupancy on bond parameters and dielectric properties. The syn-

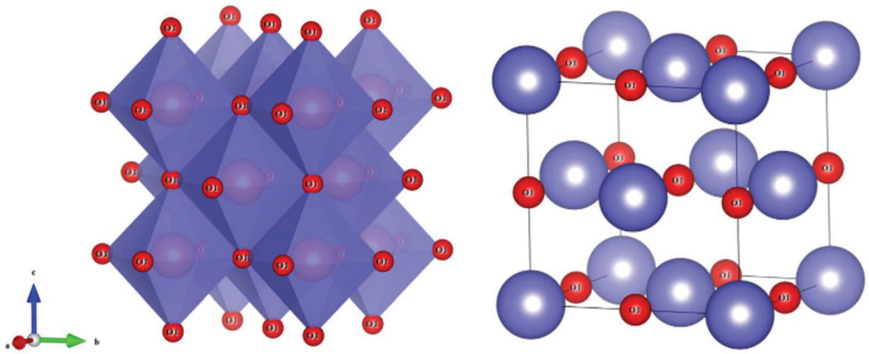

Fig. 8 Crystal structure of a cubic $Li_{2x}Mg_{1-x}Ti_xO_{1+2x}$ (x = 1/4, 2/5 and 1/2) system.

Table 6 Bond parameters, bond ionicity and bond susceptibilities of $Li_{2x}Mg_{1-x}Ti_xO_{1+2x}$ (x = 1/4, 2/5 and 1/2) systems

System	Bond type	E_h (eV)	E_g (eV)	d (Å)	f_i (%)	U (kJ mol^{-1})	χ^μ	F^μ	χ	$\chi/\sum\chi$ (%)
x = 1/4	Li–O	6.379	11.561	2.09065	69.537	2102	1.8019	0.3333	0.60	31.89
	Mg–O	6.379	16.029	2.09065	84.148	11 711	1.9310	0.5000	0.97	51.26
	Ti–O	6.379	22.611	2.09065	92.033	15 402	1.9054	0.1667	0.32	16.86
x = 2/5	Li–O	6.451	11.676	2.08160	69.500	4204	1.7871	0.4444	0.79	42.90
	Mg–O	6.451	16.191	2.08160	84.143	11 710	1.9138	0.3333	0.64	34.46
	Ti–O	6.451	22.852	2.08160	92.041	30 801	1.8861	0.2222	0.42	22.64
x = 1/2	Li–O	6.470	11.709	2.07910	69.467	2111	1.7865	0.5000	0.89	48.47
	Mg–O	6.470	16.239	2.07910	84.126	3920	1.9131	0.2500	0.48	25.95
	Ti–O	6.470	22.923	2.07910	92.034	15 467	1.8850	0.2500	0.47	25.57

thesis and structural properties of $Li_{2x}Mg_{1-x}Ti_xO_{1+2x}$ (x = 1/4, 2/5 and 1/2) ceramics were discussed by several researchers using P–V–L bond theory,[122,123,126] where the binary bonding formulas are shown as:

$$(x = 1/4)Li_2Mg_3TiO_6 = Li_2O1_2 + Mg_3O1_3 + TiO_1$$

$$(x = 2/5)Li_4Mg_3Ti_2O_9 = Li_4O1_4 + Mg_3O1_3 + Ti_2O1_2$$

$$(x = 1/2)Li_2MgTiO_4 = Li_2O1_2 + MgO$$

where all the O^{2-} anions in Li–O, Mg–O and Ti–O bonds have the same effective valence electronic numbers (Z_o) of 3, 6, 12, while for the cations they are Z_{Li} = 1, Z_{Mg} = 2, and Z_{Ti} = 4, respectively. The relative bond features of $Li_{2x}Mg_{1-x}Ti_xO_{1+2x}$ (x = 1/4, 2/5 and 1/2) systems are listed in Table 6.

From Table 6, it is straightforward to find that variation in ionic occupancy leads to a difference in bond proportion F^μ, where the F^μ values of Li–O and Ti–O bonds increase along with the x value, while for the Mg–O bond, it decreases. Average bond ionicity (f_i) value shows a monotonous downward trend from 81.906% to 81.876%, where the f_i value is descending as $f_{i(Ti-O)} > f_{i(Mg-O)} > f_{i(Li-O)}$. The lattice energy of the Ti–O bond U_{Ti-O} accounts for the majority contribution in the three types of systems. The susceptibility χ^μ of the Mg–O bond is the largest in the three types of systems; however, as indicated, the proportion of Mg–O bonds decreases, leading to different situations for the contribution to bond susceptibility, where the contributions of Li–O and Ti–O increase with the x value. The above-mentioned systems have the same structure and configuration; however, the primary relationship between the contribution of chemical bonds to bond susceptibility obviously changes along with the ionic occupancy, and then different bond features are displayed. This conclusion shows that it is necessary to consider variation in ionic occupancy when calculating bond properties of the same structure. Also, one can expect from Table 6 that the total lattice energy U in an x = 2/5 system has the largest value of 46715 kJ mol^{-1} and the smallest value of 21499 kJ mol^{-1} in an x = 1/2 system, which suggests superior structural stability in the $Li_4Mg_3Ti_2O_9$ system. And total bond susceptibility $\sum\chi$ shows a slight decline from 1.88 to 1.84 as x increases, indicating a gradually weakening dielectric polarization due to the χ value being proportional to bond susceptibility. Combined with the reported microwave dielectric performances: $Li_2Mg_3TiO_6$ ceramic well-sintered at 1600 °C with an ε_{rp} (porosity corrected) of about 16.0, a $\tan\delta$ of about 7.3 × 10^{-5}, and τ_f of *ca.* −13 ppm per °C;[129] for $Li_4Mg_3Ti_2O_9$ ceramic sintered at 1450 °C: ε_{rp} = 15.9, $\tan\delta$ = 6.0 × 10^{-5}, and τ_f = −7 ppm per °C;[122] for Li_2MgTiO_4 ceramic sintered at 1350 °C: ε_{rp} = 15.1, $\tan\delta$ = 8.4 × 10^{-5}, and τ_f = −4 ppm per °C,[123] it is shown that experimental results provide evidence for the calculations. It is notable that the $Q \times f$ value is not only affected by intrinsic structural effects, but is very sensitive to extrinsic parts, such as sintering temperature, which promotes the growth of grain and alters the amount of grain boundaries. Thus, another nonnegligible contribution to actual dielectric loss comes from extrinsic loss.

4.3.2 Ionic modification of the Mg/Ti site in cubic $Li_2Mg_3TiO_6$ systems. As important as the A_mB_n binary bonding formula expression, the discrepancy in elementary substance also affects the bond parameters because of their differences in ionic radii and electronegativity. To improve the microwave dielectric properties of $Li_2Mg_3TiO_6$ ceramics, ionic substitutions of the Mg/Ti sites were extensively studied: *e.g.* divalent cations M^{2+} (M = Zn, Co, Cu) for the Mg site and tetravalent cations M^{4+} (M = Zr, Sn, Mg/Sb, M/Ta) for the Ti site. The relationship between bond parameters and microwave dielectric properties were correlated using P–V–L bond theory.

By using Cu^{2+} cations to partially replace Mg sites, it is shown that a cubic solid solution is formed within x = 0.00–0.20 in $Li_2Mg_{3-x}Cu_xTiO_6$, as shown in Fig. 9.[130] Lattice parameters a, b, c, and V_{cell} monotonously increase due to the larger ionic radii of Cu^{2+} than Mg^{2+} at CN = 6 (0.73 Å > 0.72 Å). With the increase in Cu^{2+} content, the ionicity f_i values of all types of bonds present increasing trends with the ε_r value, indicating an enhancement in dielectric polarization. This conclusion is confirmed by the increases in observed and theoretical dielectric polarizability using the addition rule of dielectric polarizability, as shown in Fig. 10. The lattice energy U value decreases along with the x value, reflecting that the stability of crystal structure is gradually weakening and then the intrinsic loss would be reduced. Variations in the $Q \times f$ value shown in Fig. 11 provide evidence for the drop in dielectric loss. On the other hand, Kim defined the evaluating indicator of packing fraction (PF) in a scheelite compound as the proportion of volume of packed ions to the volume of a primitive unit cell, which is directly proportional to the $Q \times f$ value.[131] In a cubic rock salt $Li_2Mg_3TiO_6$ structure, a similar relationship between PF and the $Q \times f$ value can be revealed as well.

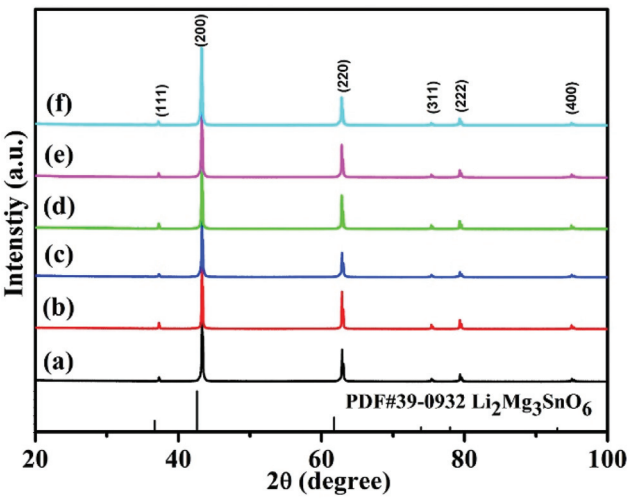

Fig. 9 The XRD patterns of $Li_2Mg_{3-x}Cu_xTiO_6$ (x = 0.00–0.20) ceramics obtained at optimum temperatures: (a) x = 0, 1310 °C, (b) x = 0.04, 1280 °C, (c) x = 0.08, 1250 °C, (d) x = 0.12, 1250 °C, (e) x = 0.16, 1220 °C, (f) x = 0.20, 1220 °C (reprinted with permission from ref. 130. Copyright 2019 Elsevier).

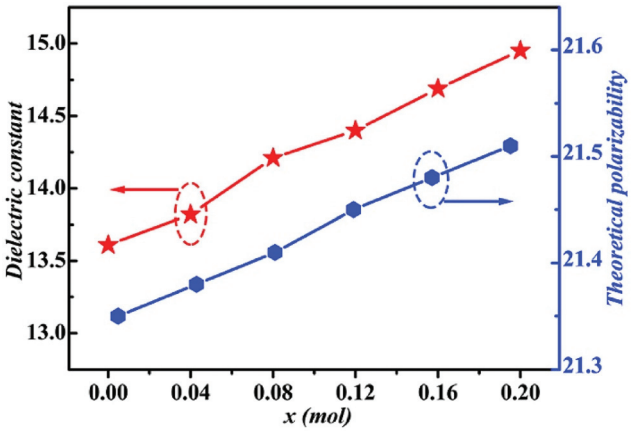

Fig. 10 The theoretical polarizability and ε_r of $Li_2Mg_{3-x}Cu_xTiO_6$ (x = 0.00–0.20) ceramics obtained at optimal densification temperatures (reprinted with permission from ref. 130. Copyright 2019 Elsevier).

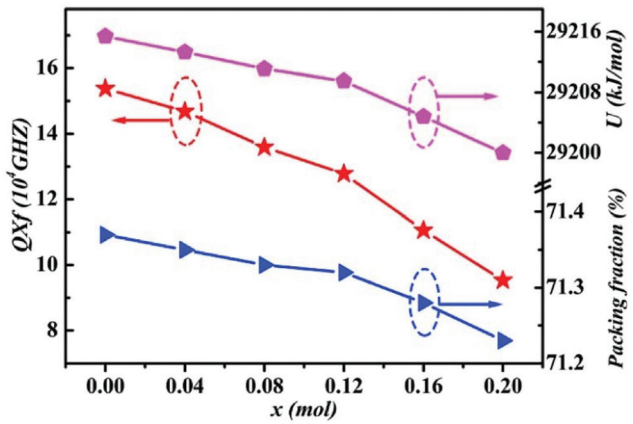

Fig. 11 The packing fraction, total lattice energy and $Q \times f$ of $Li_2Mg_{3-x}Cu_xTiO_6$ (x = 0.00–0.20) ceramics obtained at optimal densification temperatures (reprinted with permission from ref. 130. Copyright 2019 Elsevier).

In an $Li_2(Mg_{1-x}Co_x)_3TiO_6$ ($0 \le x \le 0.4$) system doped with Co^{2+} cations, the chemical bond length increases from 2.091 to 2.095 Å, which leads to an increasing trend for all types of bond ionicity f_i values.[129] The ε_r value increases with x value. Here, an increase in bond ionicity indicates increased dielectric polarization, which can be confirmed by dielectric polarizability using the Clausius–Mossotti equation. Similarly, the introduction of Co^{2+} cations decreases the crystal structural stability; as a result, the intrinsic loss would be increased. The decline in PF value also serves as a verification of this conclusion. Furthermore, ZnO is usually used as a substitution source for Mg sites. Yang reported the Zn^{2+} ionic doping of an $Li_2(Mg_{1-x}Zn_x)_3TiO_6$ (x = 0–0.2) system. In the region of x = 0–0.15, a cubic solid solution is formed, the secondary Zn_2TiO_4 phase appears when the solid solution exceeds the limit of x = 0.15. Similarly, the crystal structural parameters increase for the larger ionic radius of the Zn^{2+} cation than

Mg^{2+} (0.74 Å > 0.72 Å) cation.[132] Based on P–V–L bond theory calculation, it is also found that ionicity for all types of bonds increases with x value, corresponding to an increase in dielectric polarization and ε_r value. The decline in lattice energy also shows a similar variation trend to PF and $Q \times f$ value. The Mg site was also reported with Ca^{2+} ionic replacement; however, due to the large discrepancy between ionic radii (39% > 15%), it is unlikely to form a solid solution even over a small concentration range ($x = 0.03$) in $Li_2Mg_{3-x}Ca_xTiO_6$.[133]

From the three cases, one can find a common interesting phenomenon that the dielectric polarization increases, and the structural stability drops when the Mg site is replaced by a larger radius of cations. According to the definition of bond ionicity:

$$f_i = 1 - f_c = 1 - \frac{{E_h}^2}{{E_g}^2} \quad (47)$$

The homopolar potential energy E_h can only be smaller as bond length increases, while heteropolar energy E_g decreases. Thus, the variations in f_i value should depend on the changing ratio of homopolar energy to heteropolar energy. In a cubic structure, since cations randomly distribute at the same site, and one type of M–O1 bond exists in an $[MO_6]$ (M = Li/Mg/Ti) octahedron, decreasing ratios of E_h in all type of bonds are larger than the decreasing ratios of E_g. Thus, this phenomenon causes an increase in the bond ionicity f_i value.

For substitution of Ti sites, single cations Zr^{4+}, Sn^{4+}, Ge^{4+} and complex cations $(Mg_{1/3}Sb_{2/3})^{4+}$, $(Mg_{1/3}Nb_{2/3})^{4+}$ and $(Mg_{1/3}Ta_{2/3})^{4+}$ were chosen as sources for substitution. When a Ti site was replaced by an Sn^{4+} cation in an $Li_2Mg_3Sn_{1-x}Ti_xO_6$ system, a solid solution could be formed over the entire range of x = 0–1, as shown in Fig. 12.[134] Due to the larger radius of the Sn^{4+} (0.69 Å) cation than Ti^{4+} (0.605 Å), the introduction of SnO_2 leads to an increase in the crystal structural parameters a, b, c, and V_{cell} (from x = 1 to 0) and bond length. Based on reported bond features, it is found that the bond covalency f_c value decreases with the increase in SnO_2 content, which is in accordance with the variation in the ε_r value. This different result indicates that dielectric polarizability decreases as the content of SnO_2 increases, which is confirmed by the drop in ionic polarizability. Such a situation exists in other systems as well, such as the $Ca(Mg_{1-x}Mn_x)Si_2O_6$ system.[102] Also, increasing content of SnO_2 leads to a declining trend in structural stability and then the intrinsic loss would be increased, as shown in Fig. 13. To determine whether this phenomenon is an exception or exists in most Ti site doping cases for $Li_2Mg_3TiO_6$ ceramics, ZrO_2 was chosen in $Li_2Mg_3Zr_{1-x}Ti_xO_6$ ($0 \le x \le 1$).[135] Similarly, a solid solution was formed over the whole range of x = 0–1. An increase in Zr^{4+} cations (ionic radius: 0.72 Å) leads to an expansion of cell volume and an increase in bond length. The covalency f_c value of all bonds decreases, accompanied by a decrease in ε_r value. Structural stability also shows a similar tendency to PF and $Q \times f$ values.

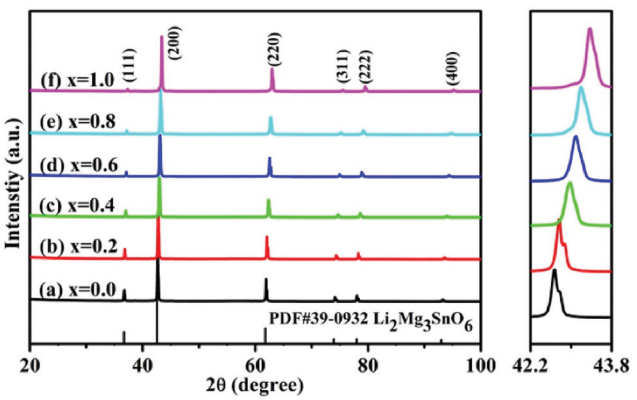

Fig. 12 The XRD patterns of $Li_2Mg_3Sn_{1-x}Ti_xO_6$ (x = 0.0–1.0) ceramics obtained at optimal temperatures: (a) x = 0.0, 925 °C, (b) x = 0.2, 925 °C, (c) x = 0.4, 925 °C, (d) x = 0.6, 900 °C, (e) x = 0.8, 900 °C, (f) x = 1.0, 900 °C (reprinted with permission from ref. 134. Copyright 2020 Elsevier).

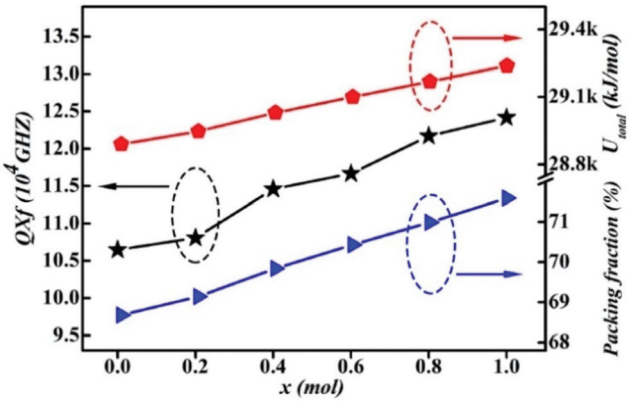

Fig. 13 The total lattice energy U_{total}, packing fraction and $Q \times f$ of the $Li_2Mg_3Sn_{1-x}Ti_xO_6$ (x = 0.0–1.0) samples obtained at optimal temperatures (reprinted with permission from ref. 134. Copyright 2020 Elsevier).

By substituting Ti sites with $(Mg_{1/3}Ta_{2/3})^{4+}$ complex cations (ionic radius: 0.72 Å) in $Li_2Mg_3Ti_{1-x}(Mg_{1/3}Ta_{2/3})_xO_6$ ($0 \le x \le 0.2$) system,[136] the cell volume and bond length increase, and based on P–V–L bond theory, the decreasing trend in bond covalency f_c value is also consistent with the ε_r value. From another point of view, Pan confirmed this decrease in ε_r value using far-infrared reflectivity. By transforming infrared spectra into a complex dielectric function with the Kramers–Kronig relationship and fitting it with a classical Lorentz three-parameter model, the real part and the imaginary part of the dielectric constant are shown in Fig. 14, and the intrinsic ε_r value is also confirmed as decreasing from 13.68 to 12.57 along with the increase in x value.

To make comparisons between the B site in cubic $Li_2Mg_3BO_6$ (B = Ti, Sn, Zr) systems, the bond parameters are listed in Table 7. From Table 7,[126,128,138] a similar conclusion could be jumped to that an increase in bond length from Ti to Zr leads to a similar decrease in the bond covalency f_c value, which corresponds to a decline in the ε_r value. Also, the higher structural stability in the B = Ti system shows its smaller

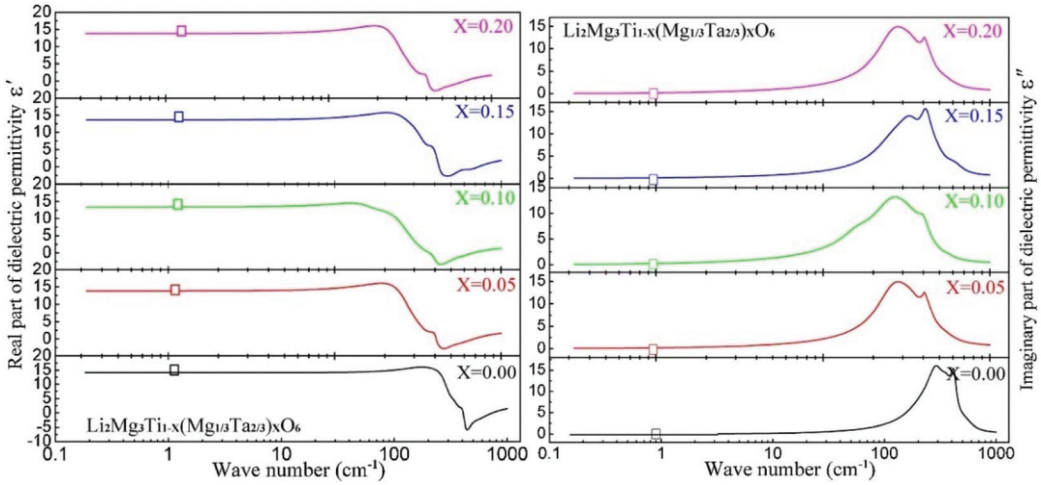

Fig. 14 Real and imaginary parts of complex permittivity for $Li_2Mg_3Ti_{1-x}(Mg_{1/3}Ta_{2/3})_xO_6$ ($0 \le x \le 0.2$) ceramics sintered at the optimum temperatures (reprinted with permission from ref. 136. Copyright 2018 Elsevier).

Table 7 Comparisons between bond ionicity, lattice energy and microwave dielectric properties of B site difference in cubic $Li_2Mg_3BO_6$ (B = Ti, Sn, Zr) systems

B	Bond type	Bond length	f_i (%)	U (kJ mol^{-1})	ε_r	$Q \times f$ (GHz)
Ti	Li–O	2.0900	69.54	2102	14.8	175 000
	Mg–O	2.0900	84.15	11711		
	Ti–O	2.0900	92.03	15402		
	Af_i = 81.91%, U_{total} = 29215 kJ mol^{-1}					
Sn	Li–O	2.1216	69.78	2078	12.4	168 330
	Mg–O	2.1216	84.25	11510		
	Sn–O	2.1216	92.06	15231		
	Af_i = 82.03%, U_{total} = 28819 kJ mol^{-1}					
Zr	Li–O	2.1365	69.89	2066	12.2	113 000
	Mg–O	2.1365	84.29	11519		
	Zr–O	2.1365	92.07	15150		
	Af_i = 82.08%, U_{total} = 28735 kJ mol^{-1}					

Table 8 Modified $Li_2Mg_3BO_6$ (B = Ti, Sn, Zr) ceramics with bond ionicity, bond covalency value, lattice energy and microwave dielectric properties

System	V_{cell}	f_i/f_c	ε_r	U	$Q \times f$
$Li_2Mg_{3-x}Cu_xTiO_6$	↗	f_i ↗	↗	↘	↘
$Li_2(Mg_{1-x}Co_x)_3TiO_6$	↗	f_i ↗	↗	↘	↘
$Li_2(Mg_{1-x}Zn_x)_3TiO_6$	↗	f_i ↗	↗	↘	↘
$Li_2Mg_3Sn_{1-x}Ti_xO_6$	↘	f_c ↗	↗	↗	↗
$Li_2Mg_3Zr_{1-x}Ti_xO_6$	↘	f_c ↗	↗	↗	↗
$Li_2Mg_3Ti_{1-x}(Mg_{1/3}Ta_{2/3})_xO_6$	↗	f_c ↘	↘	↘	↘

intrinsic loss, and the $Q \times f$ value presents the largest value among $Li_2Mg_3BO_6$ (B = Ti, Sn, Zr) systems. Also, in $(Mg_{1/3}Sb_{2/3})^{4+}$ and $(Mg_{1/3}Nb_{2/3})^{4+}$ complex ionic substitution, the cell volume increases, and the ε_r value presents a decreasing trend. At this point, one may guess that it is more convenient to predict the variation in dielectric polarization through the addition rule of ionic polarizability (α_{theo}). However, this guess does not fit with the substitution in the Ti site with Zr^{4+}, $(Mg_{1/3}Sb_{2/3})^{4+}$, $(Mg_{1/3}Nb_{2/3})^{4+}$ or $(Mg_{1/3}Ta_{2/3})^{4+}$ cations[136–138] for their large α_{theo} values of about 3.25, 3.29, 3.09 and 3.59 compared with the 2.93 of the Ti cation. Here, we summarize modified $Li_2Mg_3BO_6$ (B = Ti, Sn, Zr) ceramics with bond ionicities and bond covalency values and lattice energies in Table 8.

Therefore, we may find that the expansion or shrinkage in cell volume relies on the radius of the donor ion, while Mg site substitution with a large size of ion leads to an increase in bond ionicity f_i value and ε_r value. While in B site substitution, the variation in ε_r value is proportional to the bond covalency f_c value. Based on the bond features and microwave dielectric properties, we may put forward a conjecture that one could improve the $Q \times f$ value with a smaller size ionic substitution. Xiang reported Ti sites partially replaced with smaller sized Ge^{4+} cations (0.535 Å), and the result also showed an improvement from 1.1×10^5 at $x = 0.04$ to 1.35×10^5 at $x = 0.1$.[139] However, whether this conjecture is ubiquitous in cubic $Li_2Mg_3BO_6$ systems still requires considerable future experiments.

4.3.3 Bond features in orthorhombic $Li_3Mg_2NbO_6$ systems. $Li_3Mg_2NbO_6$ is another typical rock salt structure studied worldwide because of its excellent microwave dielectric properties: ε_r = 14.9, $Q \times f$ = 100 965 GHz, τ_f = 21.96 ppm per °C when sintered at 1225 °C for 4 h.[140] It is crystallized as an orthorhombic structure with an *Fddd* space group. The XRD patterns of $Li_3Mg_2NbO_6$ ceramics sintered at 1175–1300 °C are shown in Fig. 15.[140] A diagrammatic sketch of a crystal structure is presented in Fig. 16, where in its structure, three types of Li and Mg atoms and two types of O atoms are shown, where Li1Mg1 and Li2Mg2 atoms occupy the 16 g Wyckoff position, while Li3Mg3 atoms are in the 8b site and Nb is in the 8a site. 16f and 32 h sites are distributed with O(1) and O(2) atoms. All the cations are six-fold coordinated, forming an oxygen octahedron. Detailed structural parameters can be

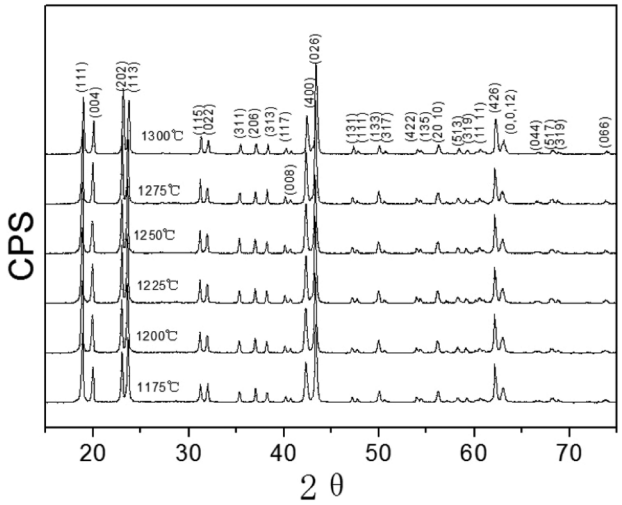

Fig. 15 X-ray diffraction patterns of $Li_3Mg_2NbO_6$ ceramics sintered at different sintering temperature from 1175 °C to 1300 °C for 4 h (reprinted with permission from ref. 140. Copyright 2016 Elsevier).

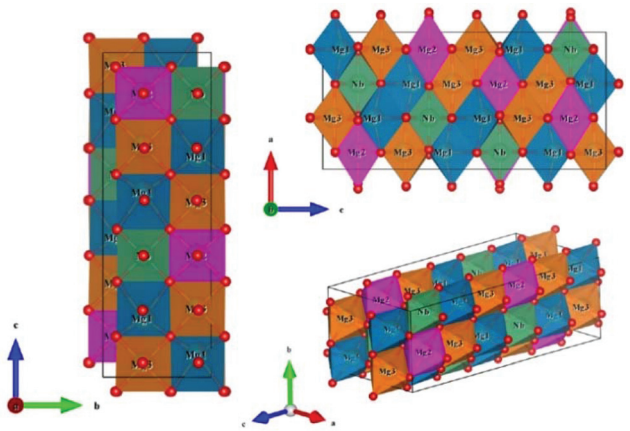

Fig. 16 Diagrammatic sketch of $Li_3Mg_2NbO_6$ structure.

traced in ref. 140. Recently, the relationships between bond characteristics and microwave dielectric properties were studied by several researchers based on the actual crystal structure, coordinate environments, and ionic occupancy. First and foremost, the binary bonding formula expression was considered by Wu:[140]

$$\begin{aligned}Li_3Mg_2NbO_6 = {} & 2/3(Li_1Mg_1)2/3O_{(1)} + 4/3(Li_1Mg_1)4/3O_{(2)} \\ & + 2/3(Li_2Mg_2)2/3O_{(1)} + 4/3(Li_2Mg_2)4/3O_{(2)} \\ & + 1/3(Li_3Mg_3)1/3O_{(1)} + 2/3(Li_3Mg_3)2/3O_{(2)}\end{aligned}$$

According to P–V–L bond theory calculation, it is found that Nb–O bonds have the largest average ionicity f_i value of about 98.72%, followed by that of Li–O bonds (95.72%) and Mg–O bonds (93.62%). As the following relationship indicates,[141] the ε^μ of a μ bond is proportional to the f_i value; it is then supposed that Nb–O bonds make the predominant contribution to dielectric polarization. Meanwhile, due to the larger total lattice energy of Nb–O bonds (25382 kJ mol^{-1}) than Mg–O (9378 kJ mol^{-1}) or Li–O (5308 kJ mol^{-1}) bonds, the importance of Nb–O bonds on structural stability is noneligible, affecting the dielectric loss:

$$\varepsilon^\mu = \frac{n^2 - 1}{1 - f_i^\mu} + 1 \quad (48)$$

where n is the refractive index. Up to now, several attempts have been made to improve the microwave dielectric properties of $Li_3Mg_2NbO_6$ ceramics at Li, Mg and Nb sites. For instance, Li^+/Ti^{4+} ions were chosen as a substitution source in an $Li_{3+x}Mg_2Nb_{1-x}Ti_xO_6$ (x = 0.02–0.08) system, where the cell volume drops along with the x value.[142] In the region of x = 0.02–0.06, the ε_r value and $Q \times f$ value show an increasing tendency. The Mg site can usually be replaced with Mn^{2+}, Ca^{2+}, Zn^{2+}, Ni^{2+}, and Co^{2+} ions.[143–147] Tetravalent Ti^{4+} and pentavalent V^{5+}, Sb^{5+}, Ta^{5+}, and hexavalent W^{6+} ions are reported to substitute for Nb sites.[148–154] For instance, a Ta^{5+} ion replaces an Nb site in $Li_3Mg_2Nb_{1-x}Ta_xO_6$ (x = 0–0.04) system leading to a decrease in cell volume, and the ε_r value increases along with the x value owing to the enhancement in dielectric polarizability. The $Q \times f$ value consistent with PF and relative density show an increasing trend with the x value. The Nb site also can be replaced with an Ti^{4+} ion because of the smaller discrepancy in ionic radius, resulting in the formation of a solid solution. Similarly, the ε_r value and $Q \times f$ value both increase from x = 0 to 0.04, improving the $Q \times f$ value from 1×10^5 to 1.31×10^5 GHz. An Sb^{5+} cation was used to substitute for the Nb site in an $Li_3Mg_2(Nb_{1-x}Sb_x)O_6$ system (x = 0.02–0.08). An orthorhombic solid solution was formed and the cell volume declined as x increased. It is also found that Sb_2O_5 leads to an increase in total bond ionicity f_i value, corresponding to an increase in ε_r value. By controlling the extrinsic loss, such as densified temperature, the extrinsic contribution to dielectric properties is minimized. The total lattice energy in accordance with the variation in $Q \times f$ value increases in the range x = 0.02–0.06, illustrating that the dielectric loss is highly correlated with structural stability in an $Li_3Mg_2NbO_6$ system. Furthermore, for reported Li bond parameters in an Zn^{2+} doped $Li_3Mg_2SbO_6$ system, a proportional relationship between bond ionicity f_i value and ε_r value can still be found, whereas the gradually decreasing total lattice energy reflects the decline in $Q \times f$ values.[155]

Just as section 4.1 shows, however, even Ca–O bonds obtain a larger bond ionicity (86.267%) value than Si–O bonds (67.983%) in a $CaMgSi_2O_6$ system, and the results show that the majority contribution to dielectric polarization originates from Si–O bonds because of their largest proportion of bond susceptibility value. Besides, it is also shown from the lattice dynamic calculation that the largest oscillator strength $\Delta\varepsilon$ (1.497) in the IR spectra of $Ca_2ZnSi_2O_7$ shows that Si–O bonds are important for the intrinsic dielectric properties. A possible reason is that the refractive index differs with an A_mB_n crystal; therefore, it would be more convincing to compare bond susceptibility in an $Li_3Mg_2NbO_6$ system to predict the variation in dielectric polarization.

4.4 Tetragonal scheelite $CaWO_4$ structure

As a tetragonal scheelite structure, alcium tungstate ($CaWO_4$) is broadly applied in laser, phosphor, and scintillation counters due to the merits of outstanding luminescence characters. The microwave dielectric properties of scheelite-type $A^{2+}B^{6+}O_4$ (A^{2+}: Ca, Pb, Ba; B^{6+}: Mo, W) ceramics were first reported, where $CaWO_4$ ceramics sintered at 1100 °C show excellent dielectric properties: ε_r = 10.4, $Q \times f$ = 76 550 GHz, τ_f = −24.4 ppm per °C.[131]

Based on the structural detail reported by Rodríguez–Hernández (COD #1546034),[156] lattice parameters of $a = b$ = 5.205 Å, c = 11.275 Å, and V_{cell} = 305.46 Å^3 with a space group of $I4_1/a$ are shown. In its crystal structure (Z = 4), as shown in Fig. 17, the W^{5+} cation is four-fold coordinated, while the Ca^{2+} cation is surrounded by eight oxygen anions. The O^{2-} anion, however, is nearly close to two Ca^{2+} ions and one W^{5+} ion, showing that its coordination number CN = 3. Thus, according to the actual structural configuration, its binary bonding formula is expressed as:

$$CaWO_4 = CaO_{8/3} + WO_{4/3}$$

The effective valence electronic numbers of O^{2-} anions in a Ca–O bond and a W–O bond are 2.25 and 13.5, respectively. The ionicity f_i value for Ca–O(2) bond is largest (75.87%), followed by that for the Ca–O(1) bond of about 75.80%, and the smallest f_i value is observed in the W–O bond (68.86%).

Shao investigated the electronic structure of the $CaWO_4$ crystal by choosing the molecular-cluster model with the framework of the fully relativistic self-consistent Dirac–Slater theory equipped with the DV-Xα method, and reported the total/partial densities of states of a perfect $CaWO_4$ crystal in Fig. 18.[157] It is proved that O 2p and W 5d states both provide contributions to the top of the valence bands and the bottom of the conduction bands, which illustrates that the W–O bond has a much stronger covalent property than other bonds in the $CaWO_4$ crystal. This finding provides evidence for P–V–L bond theory calculation. Moreover, the lattice energy U_{W-O} (29564 kJ mol^{-1}) is about ten times larger than that in Ca–O(1) (2722 kJ mol^{-1}) or Ca–O(2) (2720 kJ mol^{-1}) bonds, emphasizing the significance of W–O bonds in structural stability and intrinsic loss. It is widely acknowledged that the Raman peak with the highest intensity dominates the Raman-active vibrations, and most researchers found that the half width (FWHM) value of the most intense Raman peak is closely related with dielectric loss because the half width of the Raman scattering peak is related to the damping coefficient of structural vibration. The larger the damping coefficient of Raman scattering, the wider the half width of the peak. The damping coefficient of structure vibration is a parameter directly related to the intrinsic loss of microwave dielectric ceramics. The larger the damping coefficient of structural vibration is, the larger the intrinsic loss of microwave dielectric ceramic material would be; as a result, a lower $Q \times f$ value is presented. Gracia reported the Raman spectrum of the $CaWO_4$ crystal, as shown in Fig. 19.[158] It is shown that the most intense peak around 912 cm^{-1} is attributed to the A_g mode of the stretching vibrational behaviour of the WO_4 unit. This conclusion also supports that W–O bonds provide the major contributions to the intrinsic loss. Moreover, due to the close ionic radius between Ca^{2+} (IR = 1.12 Å at CN = 8) and Sr^{2+} (IR = 1.26 Å at CN = 8) ions, Xiao prepared a series of tetragonal $Ca_{1-x}Sr_xWO_4$ (x = 0–0.1) solid solutions, where the total bond covalency f_c shows a decreasing trend, corresponding to a decline in dielectric polarization, while the introduction of an Sr^{2+} cation is beneficial for improving the structural stability, which demonstrates an improvement in $Q \times f$ value.[159]

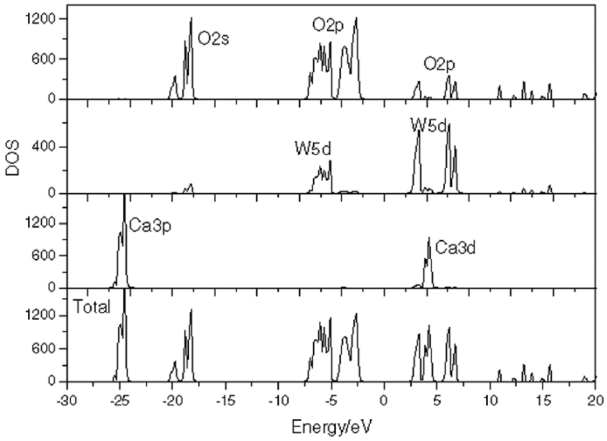

Fig. 18 Total densities of states and partial densities of states for a perfect $CaWO_4$ crystal (reprinted with permission from ref. 157. Copyright 2007 John Wiley and Sons).

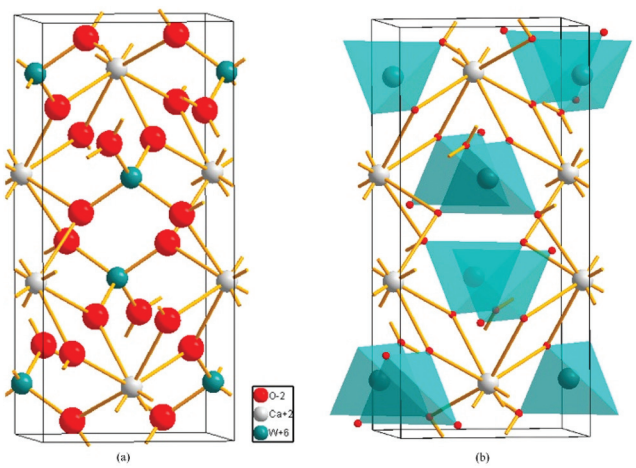

Fig. 17 Crystal structure of $CaWO_4$: (a) the coordination number of ions in $CaWO_4$, (b) the unit cell of $CaWO_4$ (reprinted with permission from ref. 159. Copyright 2018 Elsevier).

4.5 Glass-free systems for LTCC application

As a key technology of RF passive integration, several merits of low temperature cofired ceramic (LTCC) have attracted a lot of public attention: *e.g.* adjustability of dielectric properties of

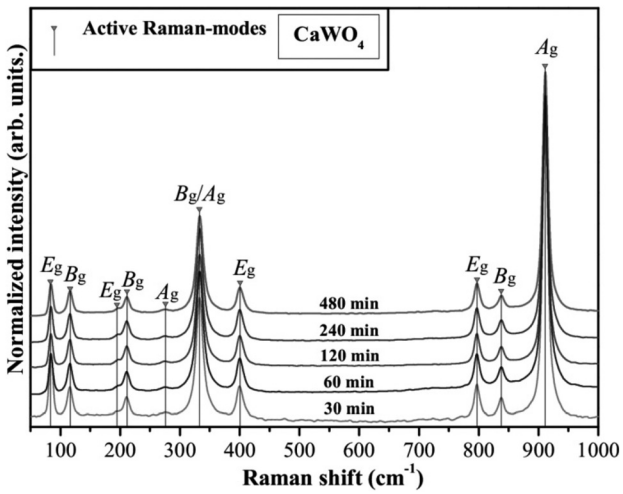

Fig. 19 FT-Raman spectra in the range from 50 to 1000 cm^{-1} of $CaWO_4$ crystals processed at 140 °C for different times in the MH system (reprinted with permission from ref. 158. Copyright 2011 AIP Publishing).

LTCC material based on different ingredients, allowing circuit design flexibility; adaptability to the requirements of high current and high temperature resistance, high reliability for application to harsh environments; circuit boards with multiple layers and passive components can be integrated, avoiding the costs of packaging, realizing the integration of passive and active components, and improving the assembly density of circuits; and excellent compatibility with other multi-layer cabling technologies.[160]

However, the excellent microwave dielectric properties of material candidates sintered at a temperature lower than 950 °C and chemical compatibility with Ag and Cu electrodes are required. Until now, two mainstream methods to prepare LTCC materials have been broadly acknowledged, where one type is to add low melting point glass frits into a ceramic matrix. The sample can be well-sintered at low temperatures with the help of a liquid phase formed by glass, such as Li_2O–B_2O_3–SiO_2, BaO–ZnO–B_2O_3, ZnO–B_2O_3–SiO_2, and CuO–B_2O_3.[161–163] However, dielectric performances have deteriorated due to the large dielectric loss of glass. Another type of ceramic has the feature of being "glass-free", where the ceramic contains low-melting oxides on their own: for instance, $BiVO_4$, Bi_2O_3–MoO_3, Li_2MoO_4, $NaAgMoO_4$ and (Ca, Bi)(Mo,V)O_4.[164–168] They can be sintered at low temperature without additives.

4.5.1 Orthorhombic olivine structure. $LiMPO_4$ (M = Mg, Mn, Co, Ni, Zn) compounds make themselves promising in LTCC because of the existence of low melting phosphates. Not only the magnetoelectric and electrochemical aspects, but the dielectric properties in the microwave region were explored: *e.g.* a low ε_r value of 6.6, a $Q \times f$ of about 79 100 GHz, and τ_f of *ca.* −55 ppm per °C for M = Mg when sintered at 950 °C.[169] For M = Ni sintered at 825 °C: ε_r = 7.18, $Q \times f$ = 27 754 GHz, τ_f = −67.7 ppm per °C.[170] The chemical compatibility of $LiMnPO_4$ with Ag presents excellent properties: ε_r = 8.1, $Q \times f$ = 44 224 GHz, τ_f = −90 ppm per °C.[171] Due to the excellent microwave properties of $LiMPO_4$ ceramics at low temperatures, several efforts have been made to analyse the structure–property relationship.

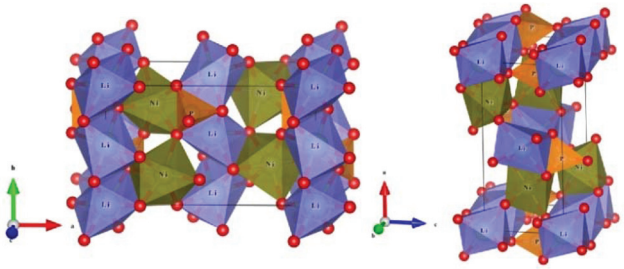

Fig. 20 Crystal structure of the orthorhombic $LiNiPO_4$ system.

Based on the crystal structure reported by Abrahams (COD #2001689), as presented in Fig. 20,[172] $LiMPO_4$ crystallizes as an orthorhombic structure with *Pnma* space group, where the lattice parameters are: a = 10.0317 Å, b = 5.8539 Å, c = 4.6748 Å, and V_{cell} = 274.643 $Å^3$. In this structure, the Li atom is in a 4a Wyckoff position, while Ni and P are in 4c sites. Besides, three types of O atoms are shown where O(1) and O(2) are in 4c sites, and O(3) is in a 8d site. Li^+ and Ni^{2+} cations are surrounded by six O^{2-} anions, forming [LiO_6] and [NiO_6] octahedra, while the P^{5+} cation is four-fold coordinated and presents a [PO_4] tetrahedron. The [LiO_6] octahedron interconnects with itself along the *b*-axis direction through sharing an edge (O(1)–O(2)). The [PO_4] tetrahedron links with the [LiO_6] octahedron by sharing a corner (O(1)) and an edge (O(3)–O(3)). The Li^+ cation appears in the top corner, face center of the *ac* plane and body center, thus, multi-layer [LiO_6] units appear, where [NiO_6] octahedra interpenetrate between layers and connect with the [LiO_6] octahedron by sharing edge (O(1)–O(3)) and corner (O(3)). By decomposing $LiMPO_4$ into binary compounds, the binary bonding formula is obtained as:[170]

$$\begin{aligned}LiNiPO_4 = {} & Li_{1/3}O(1)_{1/2} + Li_{1/3}O(2)_{1/2} + Li_{1/3}O(3)_{1/2} \\ & + Ni_{1/6}O(1)_{1/4} + Ni_{1/6}O(2)_{1/4} + Ni_{1/3}O(3)^{1}_{1/2} \\ & + Ni_{1/3}O(3)^{2}_{1/2} + P_{1/4}O(1)_{1/4} + P_{1/4}O(2)_{1/4} + P_{1/2}O(3)_{1/2}\end{aligned}$$

The coordination environment and charge distribution can be briefly explained in Fig. 21.[170] Citing O(3) as an instance, it connects with Li^+, Ni^{2+} and P^{5+} ions, where the effective valence electron numbers (Z) for the cations are 1, 2 and 5, respectively. Combined with the coordination number, an electron number of 1/6 from the Li^+ cation is given to the Li–O(3) bond. The Z values for O in Li–O, Ni–O and P–O bonds are 2, 4 and 15, respectively. Based on these considerations, the bond parameters can be calculated *via* P–V–L bond theory.

The average ionicity Af_i values are sequenced as: Af_i(Ni–O) = 76.4% > Af_i(P–O) = 74.2% > Af_i(Li–O) = 57.1%, emphasizing the indispensable role of Ni–O and P–O bonds in the ε_r value. While the lattice energy of P–O bonds provides about an

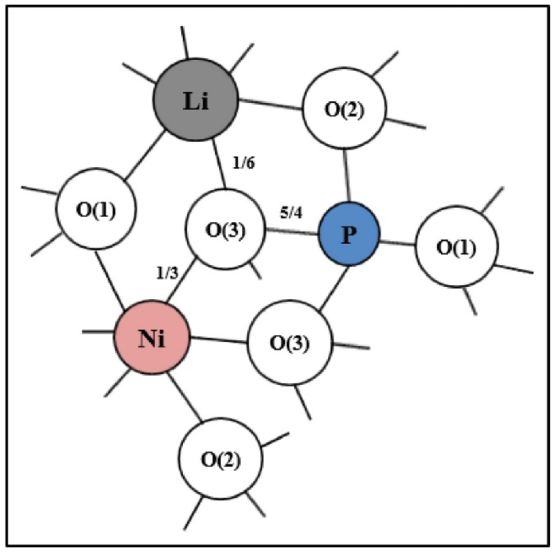

Fig. 21 The coordination number and charge distribution of ions in $LiNiPO_4$ ceramics (reprinted with permission from ref. 170. Copyright 2018 Elsevier).

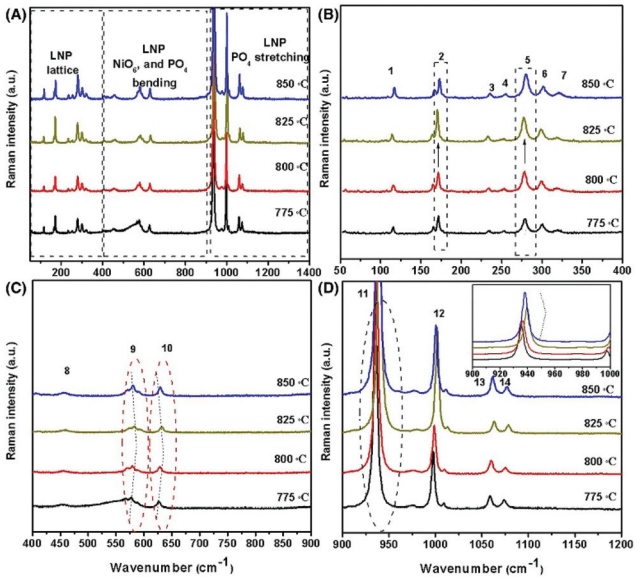

Fig. 22 (A) The Raman spectra of LNP ceramics; (B) the modes in 50–400 cm^{-1} representing the lattice modes; (C) the modes in 400–900 cm^{-1} representing mainly symmetric and antisymmetric bending modes of O–P–O and Ni–O; (D) the modes in 900–1200 cm^{-1} representing the symmetric and asymmetric stretching mode vibrations of the $[PO_4]^{3-}$ anion (reprinted with permission from ref. 173. Copyright 2019 John Wiley and Sons).

86.5% contribution (28055 kJ mol^{-1}), followed by that of Ni–O (3379 kJ mol^{-1}) and Li–O (986 kJ mol^{-1}) bonds, suggesting that P–O bonds are also important in determining the structural stability. Furthermore, as just mentioned, it would be more convincing to compare contributions to bond susceptibility to predict the ε_r value since the refractive index in eqn (48) varies with the type of binary crystal. By applying the reported bond parameters, bond susceptibility values are listed in Table 9.

As Table 9 shows, the contributions of P–O bonds reach about 46.3%, while the secondary contribution comes from Ni–O bonds (30.2%), and after that Li–O bonds account for 23.5%. These results suggest that P–O bonds may possibly be the dominant factor for dielectric polarization. Xiao reported the vibrational spectra of $LiMPO_4$ ceramics to study the Raman and IR active vibrations. Specifically, the Raman scatting spectra are shown in Fig. 22.[173] The Raman-active vibrational behaviours are divided into three regions, where in the frequency of 50–400 cm^{-1}, Raman peaks are related to lattice vibration. Internal modes associated with P–O–P bending vibrational modes are detected in 400–700 cm^{-1}, while Raman peaks in 930–1100 cm^{-1} are stretching vibrations of the $[PO_4]$ tetrahedral unit. As can clearly be seen, the most intense peaks located at 940 cm^{-1} and 1010 cm^{-1} are assigned to the $[PO_4]$ tetrahedron, suggesting its dominant role in Raman-active vibration. It is also found the peak position of the mode at 940 cm^{-1} is contrary to the change in ε_r value. This phenomenon is explained by the fact that when the Raman peak blue-shifts, the V_{cell} and electron mobility space are increased, causing the crystal to be polarized and improving the ε_r value. That is to say, the $[PO_4]$ tetrahedron is significant for dielectric polarization. If we look further, the damping value (FWHM) of both this mode (940 cm^{-1}, the symmetric stretching of the $[PO_4]$ tetrahedron) is in inverse proportion to the $Q \times f$ value, suggesting the relationship between damping coefficient of structure vibration and dielectric loss. Again, the importance of P–O bonds is emphasized.

Furthermore, far-infrared reflectivity spectra of $LiNiPO_4$ were also recorded in Fig. 23[173] and analysed using a four-parameter semi-quantum (FPSQ) model to obtain intrinsic dielectric properties, as shown in Fig. 24.[173] Based on the fitted phonon parameters, it is suggested that $[LiO_6]$ and $[NiO_6]$ octahedra account for 50.86% of the ε_r value. This finding is close to P–V–L bond theory calculation, where 53.71% contributions to bond susceptibility are indicated for $[LiO_6]$ and $[NiO_6]$ octahedra. However, infrared spectra analysis shows the majority contribution to dielectric loss (85.79%) originates from $[LiO_6]$ and $[NiO_6]$ octahedra, while bond theory shows 86.54% contributions come from P–O bonds. One poss-

Table 9 Susceptibility of chemical bonds in an $LiNiPO_4$ system

Bond type	N_e^{μ} ($Å^{-3}$)	E_g (eV)	χ^{μ}	F^{μ}	χ	$\chi/\sum\chi$ (%)
Li–O(1)	0.123	9.162	1.549	0.125	0.194	8.16
Li–O(2)	0.144	10.317	1.430	0.125	0.179	7.54
Li–O(3)	0.134	9.788	1.482	0.125	0.185	7.81
Ni–O(1)	0.265	13.074	1.900	0.063	0.119	5.01
Ni–O(2)	0.277	13.486	1.861	0.063	0.116	4.90
Ni–O(3)[1]	0.285	13.765	1.836	0.125	0.229	9.67
Ni–O(3)[2]	0.236	11.975	2.017	0.125	0.252	10.63
P–O(1)	2.746	28.722	4.148	0.063	0.259	10.93
P–O(2)	2.256	24.722	4.610	0.063	0.288	12.15
P–O(3)	2.454	26.365	4.405	0.125	0.551	23.21

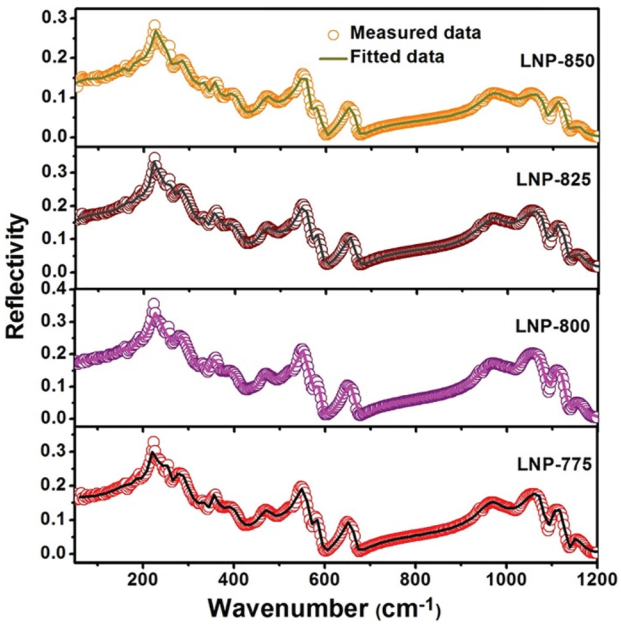

Fig. 23 Measured and fitted infrared reflectivity spectrum of LNP ceramics, together with the real parts (Re(ε)) and the imaginary parts (Im(ε)) of the complex dielectric function, as well as the reciprocal (Im(ε^{-1})), obtained from K–K analysis and the 4-P model as indicated (reprinted with permission from ref. 173. Copyright 2019 John Wiley and Sons).

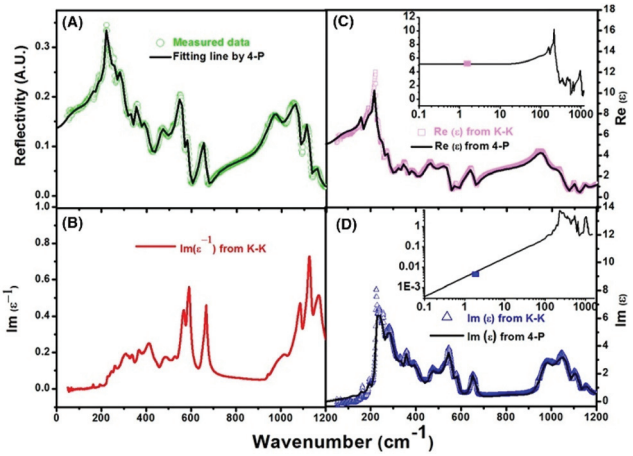

Fig. 24 (A) Fitted and measured infrared reflectivity spectra of an LNP ceramic; (B) the reciprocal of the imaginary part of permittivity obtained from K–K; (C) the real part of permittivity obtained from K–K and 4-P; and (D) the imaginary part of permittivity obtained from K–K and 4-P (reprinted with permission from ref. 173. Copyright 2019 John Wiley and Sons).

ible reason for this discrepancy is that there is no specific assignment of infrared modes *via* first principle calculations, and only general vibrations of polyhedra are classified. Thus, it is reasonable to use first-principles calculation to find out the reason for this difference.

4.5.2 Double trigonal molybdate structure. Mo-rich compounds, such as $(Na_{0.5}Bi_{0.5})MoO_4$, $Bi_2Mo_2O_9$, Li_2MoO_4, $(Na_xAg_{2-x})MoO_4$, and $Bi(Sc_{1/3}Mo_{2/3})O_4$ ceramic systems,[164,174–177] have the feature of low-temperature sintering because of the low melting point of MoO_3 of about 795 °C without using additives. Thus, the preparation technology and microwave dielectric properties are much easier to control since there is no concern about the effects of additives on phase formation, microstructure or crystal structure. Their excellent microwave dielectric performances, for instance: $(Na_{1.2}Ag_{0.8})MoO_4$: ε_r = 8.1, $Q \times f$ = 44 800 GHz, τ_f = −82 ppm per °C when sintered at 410 °C, Li_2MoO_4: ε_r = 5.5, $Q \times f$ = 46 000 GHz, τ_f = −160 ppm per °C when sintered at 540 °C, show prospects in LTCC usage. Recently, a series of molybdate-based trigonal structures with the chemical formulas of $Ln_2Zr_3(MoO_4)_9$ (Ln = La, Ce, Eu, Gd) have been reported with excellent properties when sintered at a low temperature (Ln = Gd: ST = 725 °C, ε_r = 11.2, $Q \times f$ = 57 460 GHz, τ_f = −31.9 ppm per °C).[178] By applying P–V–L bond theory, it is easier to understand the structure–property relationship.

$Ln_2Zr_3(MoO_4)_9$ shows a trigonal structure with a space group of $R\bar{3}c$(167). Its crystal structure is sketched in Fig. 25 (Ln = Ce is a case in point),[179] where two types of Zr (Zr(1) and Zr(2)) and Mo (Mo(1) and Mo(2)) atoms are presented, and six different O atoms exist. Ce and Zr2 atoms occupy 12c Wyckoff sites, and Zr1 is in a 6b site, while Mo1 and Mo2 atoms distribute in 36f and 18e sites, respectively. For O atoms, they all occupy 36f sites. The structure consists of five types of polyhedra because of different coordination environments of cations. For instance, the Ce^{3+} ion is surrounded by nine O^{2+} anion, where the bond types are classified as Ce–O1 × 3, Ce–O2 × 3 and Ce–O6 × 3. Both $Zr(1)^{4+}$ and $Zr(2)^{4+}$ ions are six-fold coordinated, while the $Zr(1)^{4+}$ ion is only in the center of an $O4^{2+}$ anion, forming a $[Zr(1)O_6]$ octahedron, and $O3^{2-}$ and $O5^{2-}$ anions are around the $Zr(2)^{4+}$ ion: Zr(2)–O3 × 3 and Zr(2)–O5 × 3. For the $[MoO_4]$ tetrahedron, Mo(1)–O1 × 1, Mo(1)–O2 × 1, Mo(1)–O3 × 1 and Mo(1)–O4 × 1 bonds are shown in $[Mo(1)O_4]$, while Mo(2)–O5 × 2 and Mo(2)–O5 × 2 bonds are presented in $[Mo(2)O_4]$.

Firstly, the binary bonding formula is decomposed into:

$$\begin{aligned} Ce_2Zr_3(MO_4)_9 = {} & Ce_{2/3}O(1)_3 + Ce_{2/3}O(2)_3 + Ce_{2/3}O(6)_3 \\ & + Zr(1)O(4)_3 + Zr(2)O(3)_3 + Zr(2)O(5)_3 + Mo(1)_{3/2}O(1)_3 \\ & + Mo(1)_{3/2}O(2)_3 + Mo(1)_{3/2}O(3)_3 + Mo(1)_{3/2}O(4)_3 \\ & + Mo(2)_{3/2}O(5)_3 + Mo(2)_{3/2}O(6)_3 \end{aligned}$$

The effective valence electron numbers of O anions in Ce–O, Zr–O and Mo–O bonds are Z_o = 2, 4 and 9, respectively. The coordination environment and charge distribution of the Ln = Zr system are sketched in Fig. 26.[180] Just as shown in section 4.3.2, discrepancies in Mg sites and Ti sites lead to different variations between ionicity and ε_r values in the $Li_2Mg_3TiO_6$ system. To figure out whether this situation occurs in trigonal $Ln_2Zr_3(MoO_4)_9$ structures, comparisons of bond ionicity, lattice energy and microwave dielectric properties among $Ln_2Zr_3(MoO_4)_9$ (Ln = La, Ce, Eu, Gd) systems are first listed in Table 10.[179–183]

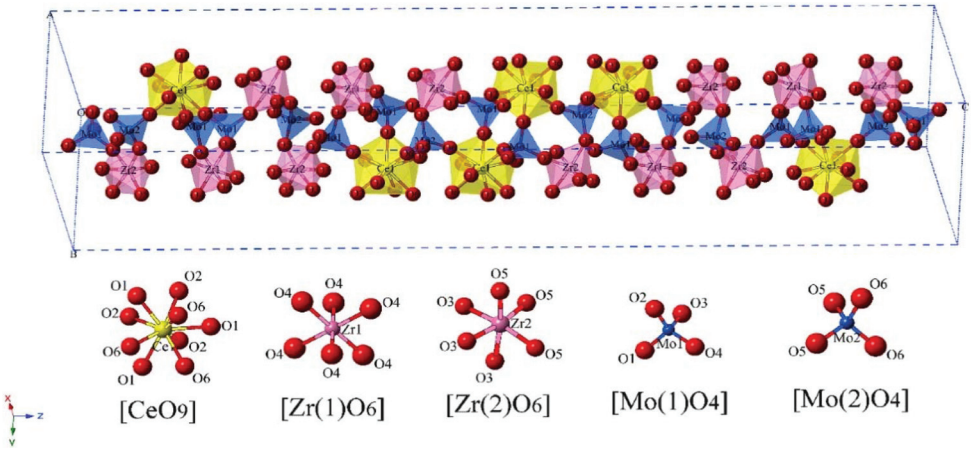

Fig. 25 Schematic diagram of the crystal structure for $Ce_2Zr_3(MoO_4)_9$ ceramics (reprinted with permission from ref. 179. Copyright 2019 Elsevier).

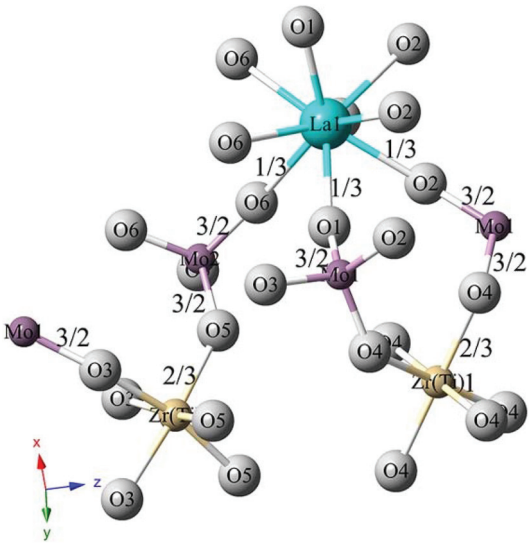

Fig. 26 The coordination number and charge distribution of ions in $La_2(Zr_{1-x}Ti_x)_3(MoO_4)_9$ ceramics (reprinted with permission from ref. 180. Copyright 2019 John Wiley and Sons).

Table 10 Comparisons between average bond ionicity, lattice energy and microwave dielectric properties of the $Ln_2Zr_3(MoO_4)_9$ (Ln = La, Ce, Eu, Gd) system

Average bond ionicity Af_i value (%)					
Ln site	Ln–O	Zr–O	Mo–O	Af_{itotal}	ε_r
La	85.146	79.306	72.801	79.324	10.17
Ce	85.178	78.975	73.250	79.321	10.69
Eu	84.967	79.100	72.575	79.121	10.75
Gd	85.000	78.825	72.863	79.097	11.17

Total lattice energy U_{total} (kJ mol^{-1})					
Ln site	Ln–O	Zr–O	Mo–O	U_{total}	$Q \times f$
La	3302	10 752	43 253	364 555	51 578
Ce	3317	10 933	42 856	363 358	24 720
Eu	3331	10 835	43 559	367 241	74 900
Gd	3336	10 988	43 180	366 144	57 460

In Table 10, it is shown that Ln–O bonds present the largest bond ionicity value, and the Af_{itotal} values show a decreasing trend as the Ln site ionic radius declines (IR values for La, Ce, Eu, Gd at CN = 9 are 1.216 Å, 1.196 Å, 1.120 Å, and 1.107 Å, respectively), while the increase in ε_r value indicates an enhancement in dielectric polarization. Considering that the densified temperatures are different, the ε_{rc} value after porosity is corrected also increases from 11.31 to 12.01. This phenomenon is similar to the ionic modification of the Ti site in $Li_2Mg_3TiO_6$ ceramics, suggesting that the bond covalency value of the Ln-site in $Ln_2Zr_3(MoO_4)_9$ (Ln = La, Ce, Eu, Gd) systems may possibly be closely related to the dielectric polarization. For lattice energy, one can still find that the largest intrinsic structural stability exists in Ln = Eu, followed by that in Gd, La, and Ce systems, which corresponds to the variations in $Q \times f$ values, where the Ln = Eu system obtains the largest value of about 74 900 GHz. This conclusion emphasizes the proportional relationship between structural stability and intrinsic dielectric loss in $Ln_2Zr_3(MoO_4)_9$ (Ln = La, Ce, Eu, Gd) systems. More importantly, by applying far-infrared reflectivity spectra, taking Ln = La as an example, as can be seen in Fig. 27,[184] the intrinsic dielectric loss is fitted and sequenced as: Eu (1.3×10^{-4}) < Gd (2.4×10^{-4}) < La (2.9×10^{-4}) < Ce (2.3×10^{-3}). This finding is also solid evidence to support the relationship between structural stability and dielectric loss. However, due to different sinterabilities, for instance, the densified temperatures of Ln = La, Ce, Eu, Gd are 650 °C, 575 °C, 600 °C, and 725 °C, the actual growth of grains and amounts of grain boundaries are different, which also negatively affects the dielectric loss.

TiO_2 is usually chosen as the Zr site substitution source. In $La_2(Zr_{1-x}Ti_x)_3(MoO_4)_9$ ceramics, solid solutions are formed in the range x = 0–0.1.[180] The introduction of a Ti^{4+} cation leads to an expansion in cell volume and bond length. Based on P–V–L theory calculation, decreasing bond ionicity is consistent

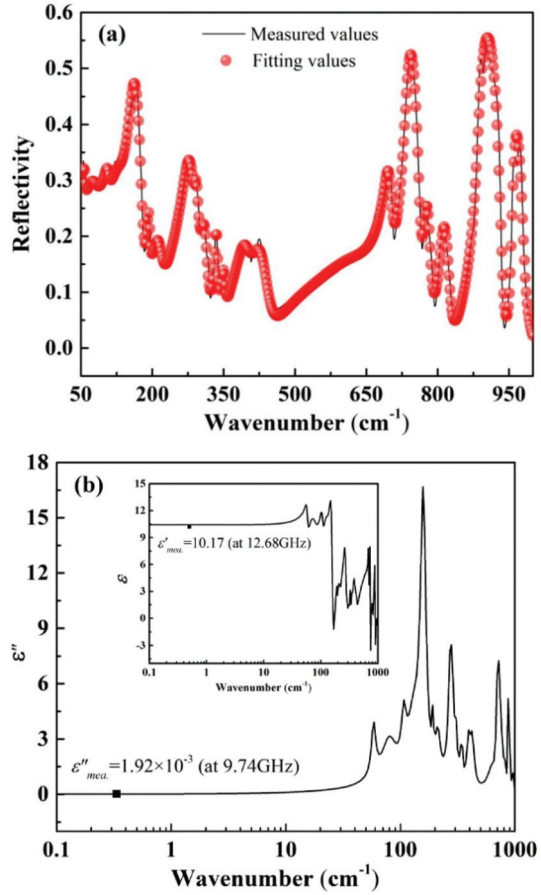

Fig. 27 (a) Measured (black line) and fitted (red line) IR reflectivity spectrum of $La_2Zr_3(MoO_4)_9$ ceramic prepared by a reaction-sintering process sintered at 650 °C for 4 h; (b) real and imaginary parts of complex permittivity for an $La_2Zr_3(MoO_4)_9$ ceramic prepared by a reaction-sintering process sintered at 650 °C for 4 h (points are measured values in the microwave region) (reprinted with permission from ref. 184. Copyright 2019 Elsevier).

with the ε_r value, which is confirmed by the observed and theoretical dielectric polarizability. It should also be mentioned that the Ti site situation can be also referred to the $Li_2Mg_3TiO_6$ system (Mg site substitution). Also, when the Zr site is partially replaced by an Sn^{4+} cation in $Ce_2(Zr_{0.94}Sn_{0.06})_3(MoO_4)_9$, one can still find a declining trend between bond ionicity and ε_r values in $Ce_2Zr_3(MoO_4)_9$ and $Ce_2(Zr_{0.94}Sn_{0.06})_3(MoO_4)_9$ systems, where the Af_{total} (ε_r) values are 79.32% (10.69) and 74.00% (10.35), respectively.[185] This conclusion indicates that in Zr site substitution, the bond ionicity value may possibly be proportional to dielectric polarization.

4.6 Cubic spinel structures

$MgO–TiO_2$ systems are appealing to the public for their richness in raw materials, low cost and excellent microwave dielectric properties. For instance, three main crystalline phases are reported in the binary $MgO–TiO_2$ phase diagram: spinel Mg_2TiO_4, ilmenite $MgTiO_3$ and pseudobrookite $MgTi_2O_5$, where Mg_2TiO_4 and $MgTiO_3$ exhibit low ε_r values and ultra-low

Table 11 Crystal structural detail, fractional coordinate, atomic position and occupancy of cubic spinel Mg_2TiO_4 structures

		Fractional coordinate			
Atom	Position	x	y	z	Occ
Mg1	8a	0.1250	0.1250	0.1250	0.964
Mg2	16d	0.5000	0.5000	0.5000	0.518
Ti1	8a	0.1250	0.1250	0.1250	0.036
Ti2	16d	0.5000	0.5000	0.5000	0.482
O	32e	0.2616	0.2616	0.2616	1.000

dielectric loss (Mg_2TiO_4: ST = 1480 °C, ε_r = 14.51, $Q \times f$ = 161 570 GHz, and τ_f = −49.3 ppm per °C; $MgTiO_3$: ST = 1400 °C, ε_r = 17.75, $Q \times f$ = 250 000 GHz, and τ_f = −42.5 ppm per °C).[186,187]

Li reported the chemical bond characteristics of the Mg_2TiO_4 system by using P–V–L bond theory. The Mg_2TiO_4 system has a cubic structure with a space group of $Fd3m$(227) and lattice parameters of $a = b = c$ = 8.443 Å and V_{cell} = 601.84 Å^3. Structural details, including fractional coordinate, atomic position and occupancy are listed in Table 11.[186]

The crystal structure is presented in Fig. 28, where the M1 site (8a) is occupied by Mg1 and Ti1, while Mg2 and Ti2 are in the M2 site (16d). A cation in the M1 site is four-fold coordinated, forming an $[M1O_4]$ tetrahedron, and an octahedral ligand $[M2O_8]$ forms in the M2 site. The O^{2-} anion is surrounded by four cations. The binary bonding formula is then expressed as:[188]

$$Mg_2TiO_4 = Mg(1)_{0.964}O_{0.964} + Mg(2)_{1.036}O_{1.554} + Ti(1)_{0.036}O_{0.0036} + Ti(2)_{0.964}O_{1.446}$$

Thus, Ti–O bonds show larger bond ionicity (88.34%) values than Mg–O bonds (76.62%), and the lattice energy of Ti–O bonds (13290 kJ mol^{-1}) is two times larger than that of Mg–O bonds (7473 kJ mol^{-1}). By substituting the Ti site with an Sn^{4+} cation in $Mg_2(Ti_{1-x}Sn_x)O_4$, a cubic solid solution was formed over the whole range of x = 0–1. An increase in Sn^{4+} content leads to an enhancement in bond lengths. Based on P–V–L bond theory calculation, it is found that the decrease in average bond covalency is responsible for the drop in ε_r value, as shown in Fig. 29.[186] The structural stability reflected by the U_{total} value gradually weakens as x increases. To verify the structural changes, Raman scatting spectra are presented in Fig. 30.[186] Raman-active vibrational modes are assigned into three parts, where the Raman modes located in the high-frequency region (600–750 cm^{-1}) are attributed to the symmetric stretching (A_{1g}) and asymmetric stretching behaviours ($T^1{}_{2g}$) of the $[M1O_4]$ tetrahedron. Modes in (350–600 cm^{-1}) are classified as symmetric ($T^2{}_{2g}$) and asymmetric (E_g) bending behaviours of the $[M1O_4]$ tetrahedron. The mode at 323 cm^{-1} implies a local lattice in the octahedral sub-lattice. The most intense Raman peak (A_{1g}) usually has a dominant effect on structural variation. It is shown that the A_{1g} mode redshifts as x increases, which verifies that the increase in cell volume and

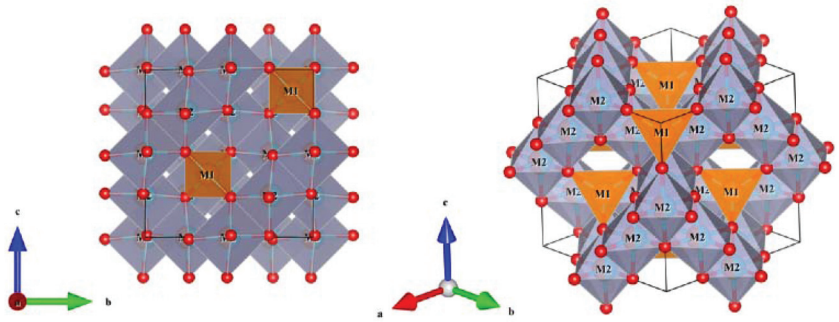

Fig. 28 Crystal structure of a cubic spinel Mg_2TiO_4 crystal.

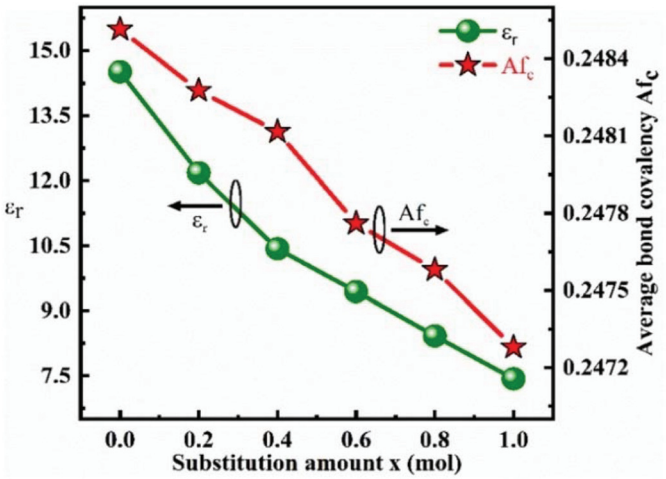

Fig. 29 The dielectric constant ε_r and the average bond covalency Af_c variation with x varying from 0 to 1 (reprinted with permission from ref. 186. Copyright 2019 Elsevier).

bond length leads to a decrease in vibrational energy. Thus, the decrease in the ε_r value is verified by the shift in A_{1g} Raman peak position.

4.7 Orthorhombic europium titanium structure

Ln_2TiO_5 ceramics have potential in the usage of forms of nuclear waste because of their excellent chemical durability and tolerance to high-energy particles. Recently, Zheng reported a novel orthorhombic europium titanium type Eu_2TiO_5 microwave dielectric system and analysed the bond parameters using P–V–L bond theory for the first time.[189]

Unlike reported crystal structural types, Eu_2TiO_5 is an orthorhombic structure with a *Pnam*(62) space group and lattice parameters of a = 10.5342 Å, b = 11.2957 Å, c = 3.7785 Å and V_{cell} = 449.61 Å^3, where cations are mixed with seven and five-fold coordination, as shown in Fig. 31. Two types of Eu atoms, and six different types of O atoms are shown. Specifically, both $Eu1^{3+}$ and $Eu2^{3+}$ cations are seven-fold coordinated, which is regarded as an irregular octahedron with the addition of a seventh atom. It is also reported that based on the polyhedral configuration of seven-fold coordination,

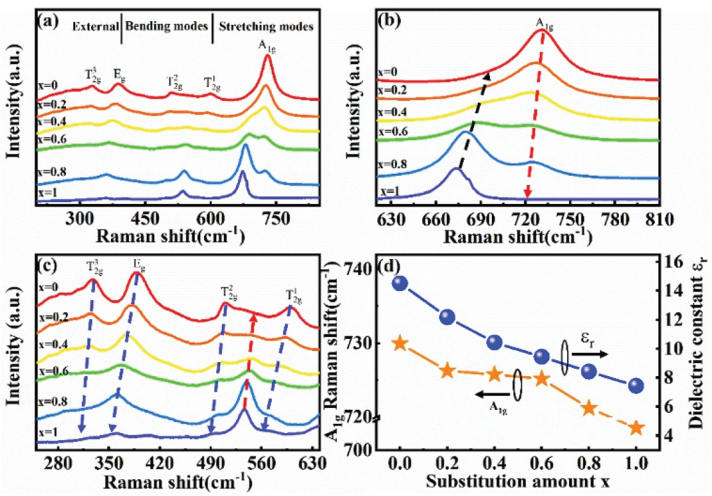

Fig. 30 (a) The Raman spectra of $Mg_2(Ti_{1-x}Sn_x)O_4$ compounds in the range 200 cm^{-1}–850 cm^{-1}; (b) the variation in Raman shift in the high frequency region (600 cm^{-1}–730 cm^{-1}); (c) the variation in Raman shift in the range 280 cm^{-1}–630 cm^{-1}; (d) the relationship between dielectric constant and A_{1g} Raman shift (reprinted with permission from ref. 186. Copyright 2019 Elsevier).

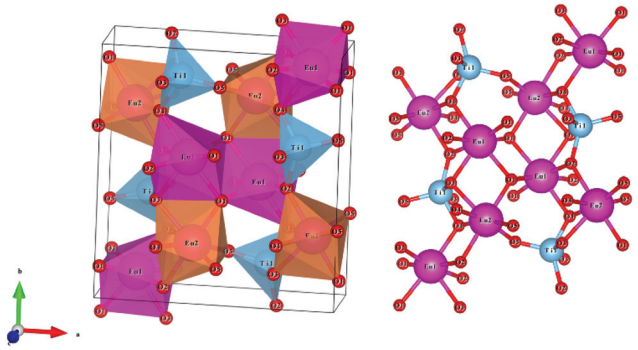

Fig. 31 Crystal structure of an orthorhombic Eu_2TiO_5 crystal.

the coordination of the Ln cation (for instance Ln = Y) can be regarded as a cube missing one oxygen atom, and a distorted trigonal prism with a seventh oxygen atom connected *via* a face.[190] The Ti^{4+} cation is surrounded by five O^{2-} anions. Eu1 is the center cation connecting with three O1, two O2, one O3 and one O4 anions in an Eu1 polyhedron; however, Eu2 connects with one O1, one O2, one O3, two O4 and two O5 anions in an Eu2 polyhedron. The Ti^{4+} cation links with one O2, two O3, one O4 and one O5 anion. The binary bonding formula is written as:[189]

$$\begin{aligned}Eu_2TiO_5 = {} & Eu(1)_{3/7}O(1)_{3/4} + Eu(1)_{2/7}O(3)_{1/2} + Eu(1)_{1/7}O(3)_{1/4} \\ & + Eu(1)_{1/7}O(4)_{1/4} + Eu(2)_{1/7}O(1)_{1/4} + Eu(2)_{1/7}O(2)_{1/4} \\ & + Eu(2)_{1/7}O(3)_{1/4} + Eu(2)_{2/7}O(4)_{1/2} + Eu(2)_{2/7}O(5)_{2/3} \\ & + Ti_{1/5}O(2)_{1/4} + Ti_{2/5}O(3)_{1/2} + Ti_{1/5}O(4)_{1/4} + Ti_{1/5}O(5)_{1/3}\end{aligned}$$

It is important to note that even for the same cation, taking Eu(2) as an example, the effective valence electron numbers of the O anion (Z_o) in Eu–O bonds are different: Z_o = 36/7 in an Eu(2)–O(4) bond, and Z_o = 27/7 in an Eu(2)–O(5) bond. Those values in Ti–O bonds also vary as the m and n values in A_mB_n change.

After taking these factors into consideration, the average bond ionicity f_i value is arranged as follows: $f_{i(Eu1-O)}$ = 88.17% > $f_{i(Eu2-O)}$ = 85.99% > $f_{i(Ti-O)}$ = 77.04%, where the chemical bonds tend to be more ionic, and the largest f_i value is found in the Eu1–O bond. For the lattice energy, Ti–O bonds have the largest average lattice energy AU value of about 3626 kJ mol^{-1}, followed by that of Eu1–O (1251 kJ mol^{-1}) and then Eu2–O (1241 kJ mol^{-1}) bonds, which shows that Ti–O bonds play an indispensable role in determining the structural stability of an orthorhombic Eu_2TiO_5 structure.

Niu reported the electron localization function (ELF) based on first principles calculation to give an insightful estimate of the ionicity or covalency aspects of bonds in orthorhombic Ln_2TiO_5 systems (Ln = La, Sm, Gd, Dy), as presented in Fig. 32.[191] As a dimensionless, empirical function, the ELF that generated comparatively large values (>0.5) is ascribed to the bonding/nonbonding localized electrons and smaller values (<0.5) for delocalized electrons. It is found that in both

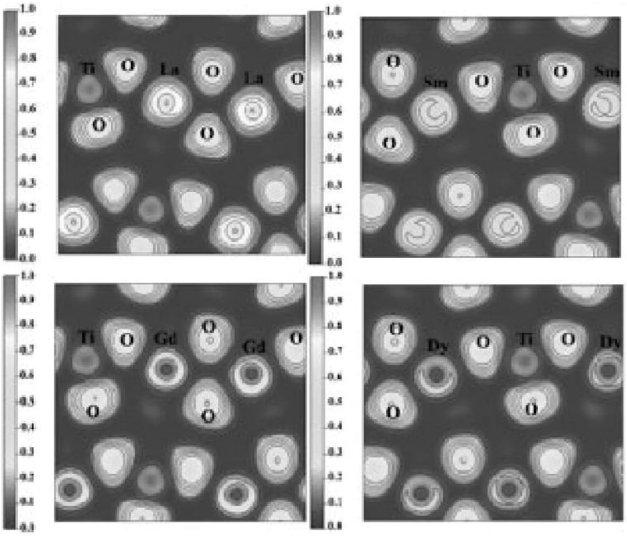

Fig. 32 ELF at the (040) plane for La_2TiO_5, Sm_2TiO_5, Gd_2TiO_5 and Dy_2TiO_5. (reprinted with permission from ref. 191. Copyright 2011 Cambridge University Press).

Ln/Ti–O bonds, the bond ionicity should be the essential factor, and Ti–O bonds are more covalent than Ln–O bonds for the σ-bonding Ti (3d)–O(2p) orbital interaction. This theoretical calculation also provides evidence for the bond ionicity results that Ti–O bonds have the largest bond covalency value of about 22.96% compared to that of Eu–O bonds of 14.01%.

4.8 Monoclinic fergusonite structure

As a typical case of fergusonite $RENbO_4$, $NdNbO_4$ is interesting to the public and is widely studied for its widespread application prospects. For instance, a phase transformation of $RENbO_4$ takes place between a tetragonal scheelite structure and a monoclinic ferroelastic structure at about 550 °C.[192] It could be promising for the application of anode-supporting substrates, proton conducting cells and energy-absorption by virtue of its surface properties, chemical compatibility and the strain resulting from the phase transformation.[193–196] For MWDC applications, a $RENbO_4$ ceramic also shows excellence in dielectric performance because of the existence of an [NbO_6] framework and rare-earth elements. *e.g.* an ε_r of 19.6, a $Q \times f$ value of about 33 000 GHz and a τ_f of −24 ppm per °C are obtained for an $NdNbO_4$ ceramic,[82] and for an $LaNbO_4$ ceramic sintered at 1275 °C: ε_r = 20.3, $Q \times f$ = 59 740 GHz, τ_f = 7.44 ppm per °C,[197] and a much lower dielectric loss is found in $(La_{0.92}Sm_{0.08})NbO_4$ ceramics with an ε_r value about 19.37, a $Q \times f$ value of 62 203 GHz and a τ_f of *ca.* 2.57 ppm per °C.[198] Thus, much effort has been put into studying the structure–property relationship and improving the microwave dielectric properties.

Based on the reported monoclinic fergusonite crystal structure configuration of $NdNbO_4$ ceramic: a = 5.146 Å, b = 11.294 Å, c = 5.451 Å and V_{cell} = 317.25 $Å^3$ with a space group of $I2/a$(15), as shown in Fig. 33,[199] the structure consists of a distorted [NdO_8] dodecahedron and [NbO_6] octahedron.

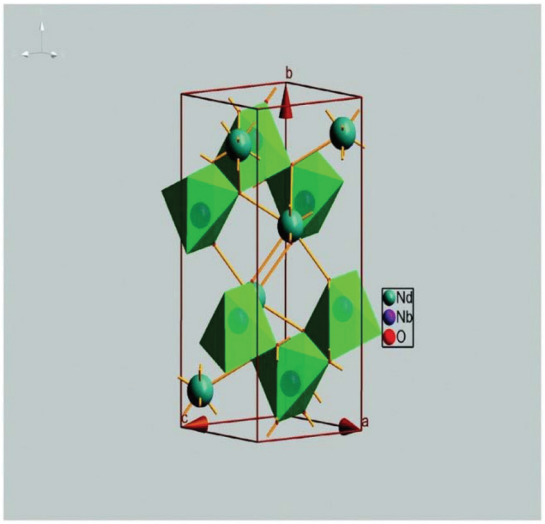

Fig. 33 The crystal structure patterns of the (1 × 1 × 1) supercell of monoclinic fergusonite structured $NdNbO_4$ (reproduced from ref. 199 with permission from the PCCP Owner Societies).

$[NbO_6]$ frames form a one-dimensional zigzag chain by sharing an edge, while the $[NdO_8]$ units are set in the propagating chains of $[NbO_6]$ sharing the oxygen. Both Nd and Nb atoms are in a 4e Wyckoff site, and both connect with two Nd^{3+} cations and two Nb^{5+} cations (CN = 4), while the O2 anion links with two Nd^{3+} cations and one Nb^{5+} cation (CN = 3). This discrepancy results in different effective valence electron numbers for the O anion (Z_o). Firstly, the binary bonding formula should be decomposed into:[199]

$$NdNbO_4 = Nd_{1/4}O(1)^1_{1/2} + Nd_{1/4}O(1)^2_{1/2} + Nd_{1/4}O(2)^1_{2/3} + Nd_{1/4}O(2)^2_{2/3} + Nb_{1/3}O(1)^1_{1/2} + Nb_{1/3}O(1)^2_{1/2} + Nb_{1/3}O(2)_{2/3}$$

Apparently, the Z_o values in $Nd_{1/4}$–O(1), $Nd_{1/4}$–O(2), $Nb_{1/3}$–O(1) and $Nb_{1/3}$–O(2) are 4.5, 3.375, 10 and 7.5, respectively. With the same crystal structure, bonding environment and binary bonding expressions of $RENbO_4$ (RE = Nd, La) ceramics, detailed comparisons between chemical bond features are listed in Table 6S.† Here, we summarize the bond ionicity, lattice energy and microwave dielectric properties in Table 12.[197,199]

Table 12 Comparisons of average bond ionicity, total lattice energy and microwave dielectric properties in $RENbO_4$ (RE = Nd, La) ceramics

RE	Bond type	Af_i (%)	U_{total} (kJ mol^{-1})	$\chi/\sum\chi$ (%)	ε_r	$Q \times f$ (GHz)
Nd	Nd–O	85.55	5767	48.22	19.6	33 000
	Nb–O	85.56	19 530	51.78		
	$\sum\chi$ = 2.98, Af_{itotal} = 85.55%, U_{total} = 25297 kJ mol^{-1}					
La	La–O	84.82	5412	53.87	20.3	59 740
	Nb–O	84.61	20 553	46.13		
	$\sum\chi$ = 3.62, Af_{itotal} = 84.73%, U_{total} = 25965 kJ mol^{-1}					

Combined with Table 6S in ESI† and Table 12, it can be found that all the ionicity f_i values of the chemical bonds in $LaNbO_4$ are smaller than those in the $NdNbO_4$ system. For the two structures, specifically, Af_i values of Nd–O bonds are very close to those of Nb–O bonds, and their susceptibility contribution ratios are also very similar. However, large contributions of lattice energy originate from Nb–O bonds (79%). This is to say, both Nd–O and Nb–O bonds are responsible for the dielectric polarization, but Nb–O bonds are the crucial factor for stabilizing the crystal structure. Moreover, it is also shown that the ε_r value of $LaNbO_4$, which is higher than that of $NdNbO_4$, corresponds to a lower bond ionicity value, suggesting that in the Nd–La transformation, an increase in bond covalency may possibly be closely related to dielectric polarization. This can be confirmed by the increase in bond susceptibility. High stability in $LaNbO_4$ ceramics also agrees with a higher $Q \times f$ value, which indicates that the structural stability in monoclinic fergusonite $RENbO_4$ (RE = Nd, La) is also an intrinsic factor determining intrinsic dielectric loss. Zhang reported the substitution of an La^{3+} ion on an Nd site in $(Nd_{1-x}La_x)NbO_4$ ceramics,[199] and the results show that an increase in the ε_r value is consistent with average bond covalency, and an increasing content of La_2O_3 (x = 0–0.06) is beneficial to improving the structural stability and $Q \times f$ value. This finding supports the conclusion above. The Nd site also can be replaced by an Sm^{3+} cation in $(Nd_{1-x}Sm_x)NbO_4$ ceramics. Interestingly, the bond ionicity decreases along with the ε_r value, and an increase in the $Q \times f$ value is also attributed to the enhancement in U_{total} value.[200] There is a temperature-induced phase transition in $SmNbO_4$ ceramics from a monoclinic to a tetragonal structure when the temperature exceeds 800 °C but no relevant chemical bond parameters have been reported for $SmNbO_4$; therefore, it is difficult to compare detailed bond features in RE = Nd, Sm systems.[201]

As noted, Nb–O bonds are the dominant influence on structural stability, apart from Nd site substitution. The Nb site is also substituted by pentavalent single ions and complex ions to improve the $Q \times f$ value: *e.g.* in the solid solution region of the $(1-x)LaNbO_4$–$xLaVO_4$ system (x = 0–0.1), the drop in ε_r value is also ascribed to the decrease in bond ionicity, which can be confirmed by the drop in dielectric polarizability of V^{5+} (2.92 Å) compared to Nb^{5+} (3.97 Å) and an increase in U_{total} value confirms the great improvement in $Q \times f$ value from 6770 GHz to 62370 GHz.[202] Substitution of the Nb site using Ta_2O_5 as a source in $LaNbO_4$ ceramics presents a similar trend, where the ε_r value consistently decreases with bond ionicity, and the increase in structural stability induced by the Ta^{5+} cation improves the $Q \times f$ value from 47 000 GHz to 66000 GHz.[203]

Complex ions, such as $(Al_{1/3}W_{2/3})^{5+}$, $(Mg_{1/4}W_{3/4})^{5+}$, $(Zr_{1/2}W_{1/2})^{5+}$ and $(AMo)^{5+}$ (A = Mg, Al, Si, Zr) were used to replace the Nb site. For instance, Yang took variations of $(Al_{1/3}W_{2/3})^{5+}$ and $(Mg_{1/4}W_{3/4})^{5+}$ ionic occupancies into consideration in modified $NdNbO_4$ systems,[204,205] and the results show that even the cell volume shows different changes. Both the average bond ionicity values are responsible for the ε_r value,

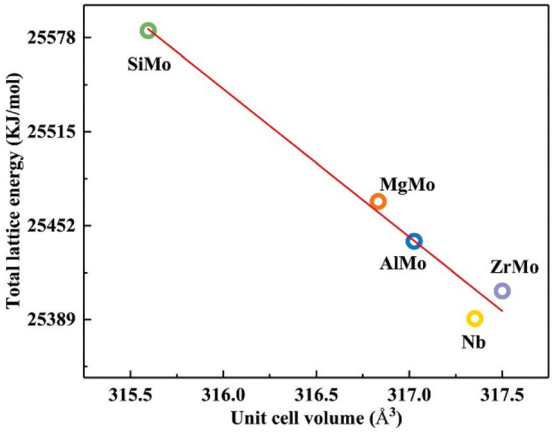

Fig. 34 Correlation between the lattice energy and molecular volume of different $NdNbO_4$-based ceramics (reprinted with permission from ref. 206. Copyright 2019 Elsevier).

and, for the $Q \times f$ value, variations in lattice energy and actual average size of grain together make contributions to the actual dielectric loss. They also found a close relationship between total lattice energy and cell volume in $(AMo)^{5+}$ (A = Mg, Al, Si, Zr) substitution, as shown in Fig. 34,[206] where shrinkage in cell volume improves the structural stability, consequently reducing the intrinsic loss. Based on their reports on microwave dielectric properties, an SiMo doping system also shows the largest $Q \times f$ value of about 49 466 GHz, which is higher than that of the undoped situation of 24 750 GHz.

4.9 Complex perovskite structure

Complex perovskite $Ba(M_{1/3}M'_{2/3})O_3$ (M = Mg, Ni, Zn; M′ = Nb, Ta) structures are well known for and have been broadly studied for their outstanding microwave dielectric properties For instance, $Ba(Mg_{1/3}Ta_{2/3})O_3$ ceramic has a moderate ε_r value of about 24, an ultra-high $Q \times f$ value of 250 000 GHz and a near-zero τ_f value,[1] and it is mostly used in resonators and has achieved widespread commercial value and thus continuously attracts public attention. Until now, much effort has been put into exploring the intrinsic structural impacts on dielectric performances: *e.g.* a 1 : 2 ordered structure was clearly revealed using transmission electron microscopy in Ba $((Co_{0.5}Zn_{0.3}Mg_{0.2})_{1/3}Nb_{2/3})O_3$ ceramic along $\langle 110\rangle_c$, $\langle 111\rangle_c$ and $\langle 112\rangle_c$ projections, where the ordering of M and M′ cations was considered to be a crucial factor for microwave dielectric properties.[207]

The Raman active and infrared active modes were assigned in detail by using first principles lattice dynamics calculation based on density functional theory, with the conclusion that the low dielectric loss found in this ordered $Ba(Mg_{1/3}Ta_{2/3})O_3$ ceramic can be ascribed to the long phonon lifetime and weak coupling among phonons.[208] The $Ba(Mg_{1/3}Ta_{2/3})O_3$ system is crystallized as a hexagonal structure with a $P\bar{3}m1(164)$ space group, as shown in Fig. 35. Based on reported structural details (COD #4000400) of $a = b = 5.77385$ Å, $c = 7.09376$ Å, $V_{cell} = 204.804$ Å^3 and P–V–L bond theory consideration, coordination environments for each cation are listed in Table 13. Also, the binary bonding formula is written as:

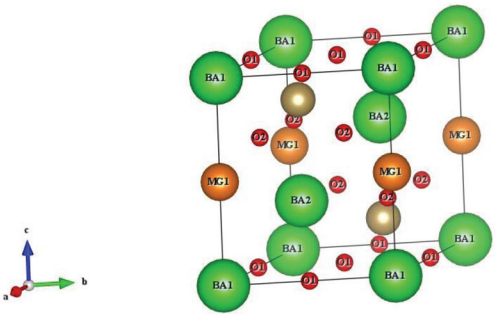

Fig. 35 Crystal structure of a hexagonal $Ba(Mg_{1/3}Ta_{2/3})O_3$ system.

Table 13 Coordinate environments of the $Ba(Mg_{1/3}Ta_{2/3})O_3$ system

$Ba_3MgTa_2O_9 = Ba_1 1 Ba_2 1 Mg Ta 2 O_1 3 O_2 6$			
Ba1	Ba2	Mg	Ta
CN = 12	CN = 12	CN = 6	CN = 6
N(Ba1–O1) = 6	N(Ba1–O1) = 3	N(Mg–O2) = 6	N(Ta–O1) = 3
N(Ba1–O2) = 6	N(Ba1–O2) = 9		N(Ta–O2) = 3
O1	O2		
CN = 6	CN = 6		
N(O1–Ba1) = 2	N(O2–Ba1) = 1		
N(O1–Ba2) = 2	N(O2–Ba2) = 3		
N(O1–Ta) = 2	N(O2–Mg) = 1		
	N(O2–Ta) = 1		

CN: coordination number, $N(B^j\text{–}A^i)$ represents the number of A^i cations in the ligand of the B^j ion.

$$Ba_3MgTa_2O_9 = Ba1_{1/12}O1(1)_{1/6} + Ba1_{5/12}O1(2)_{5/6} + Ba1_{1/2}O2_1 + Ba2_{1/2}O1_1 + Ba2_{1/2}O2(1)_1 + Ba2_1O2(2)_2 + Mg_1O2_1 + Ta_1O1_1 + Ta_1O2_1$$

Detailed bond features of the $Ba(Mg_{1/3}Ta_{2/3})O_3$ system can be found in Table 7S in ESI.† The average bond ionicity, effective valence electron number of oxygen anions, total lattice energy and bond susceptibility are summarized in Table 14.

Based on the results from Table 14, it can be seen that Ba–O bonds have the largest bond ionicity f_i value; however, the majority contributions to bond susceptibility come from Ta–O bonds, followed by Mg–O and Ba–O bonds. Furthermore, Ta–O

Table 14 Average bond ionicity, effective valence electron number of oxygen anion, total lattice energy and bond susceptibility of the $Ba(Mg_{1/3}Ta_{2/3})O_3$ system

Bond type	Af_i (%)	Z_o	U_{total} (kJ mol^{-1})	χ	$\chi/\sum\chi$ (%)
Ba1–O	95.61	3	2309	0.174	9.93
Ba2–O	95.61	3	3443	0.353	20.11
Mg–O	77.40	6	3864	0.564	32.14
Ta–O	89.78	15	49 016	0.664	37.82

bonds contribute about 89.8% of total lattice energy. This conclusion illustrates that Ta–O bonds in [TaO_6] octahedra may be the dominant factor determining the dielectric properties.

By performing first principles calculations to obtain thorough vibrational modes and comparing them with an experimental far-infrared reflectivity spectrum, Wang assigned the specific vibrational behaviours in a $Ba(Mg_{1/3}Ta_{2/3})O_3$ system.[209] For instance, symmetry coordinates and polarization are illustrated in Fig. 36. According to their fitting results of the FIR reflection spectrum using a four-parameter semi-quantum model, it is shown that the $E_u^{(4)}$ mode at 220 cm^{-1} and the $E_u^{(5)}$ mode at 241 cm^{-1} provide the largest theoretical contributions to dielectric properties. More importantly, the $E_u^{(4)}$ and $E_u^{(5)}$ modes are assigned as the vibrations of [TaO_6] octahedra (Ta motion *versus* O and vibration of O octahedra); that is to say, based on first principles calculation, it is confirmed that [TaO_6] octahedra should be the dominant reason for the dielectric properties, which is consistent with the results from P–V–L bond theory. Furthermore, the $E_u^{(4)}$ and $E_u^{(5)}$ modes in total contribute about 53.8% and 90.2% to the dielectric constant ε_r and dielectric loss tan δ, which are also close to the results from Table 14. Similarly, first principles calculation indicates that the $E_u^{(1)}$ mode at 149 cm^{-1} and the $A_{2u}^{(2)}$ mode at 212 cm^{-1}, where the vibrational behaviours closely related to [NbO_6] octahedra, dominate the dielectric properties in the $Ba(Mg_{1/3}Nb_{2/3})O_3$ system.[210]

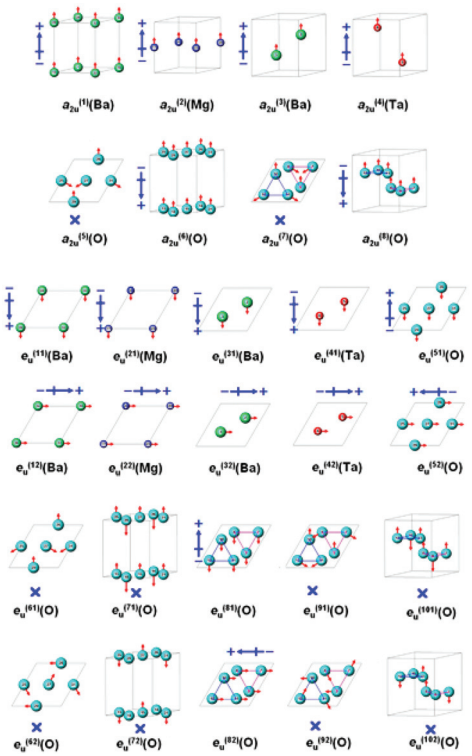

Fig. 36 Symmetry coordinates and polarization of $Ba(Mg_{1/3}Ta_{2/3})O_3$. The arrows (⟷) stand for the polarizing direction and the crosses (×) stand for no polarization (reprinted with permission from ref. 209. Copyright 2010 John Wiley and Sons).

At this point, we are driven to wonder whether the dominant factor in a complex perovskite structure is dependent on the heavier atom. Another typical complex perovskite can be found in cubic $Ba(Mg_{1/2}W_{1/2})O_3$ ceramics (ε_r = 17, $Q \times f$ = 42 000 GHz, τ_f = −33.6 ppm per °C). Based on reported first principles calculations, it is shown that the $F_{1u}^{(2)}$ mode at 277 cm^{-1} makes about 47.5% and 80.5% contributions to ε_r and tan δ, while the mode is regarded as the stretching behaviours of [MgO_6] and [WO_6] octahedra.[211] $Ba(Mg_{1/2}W_{1/2})O_3$ is a cubic structure with a space group of *Fm3m* and lattice parameters of: $a = b = c$ = 8.112 Å, and V_{cell} = 533.807 $Å^3$ as reported by Filip'ev from COD #1537301.[212] In the view of P–V–L bond theory, its coordination environment of cations is totally different from that in the $Ba(Mg_{1/3}Ta_{2/3})O_3$ system, where the binary bonding formula is much simpler with only one type of bond shown in the oxygen polyhedron:

$$Ba_2MgWO_6 = Ba_2O_4 + MgO + WO$$

The bond parameters are listed in Table 15. Comparing Table 15 with Table 14, it can be seen that even the f_i values are close to each other; however, the contributions to bond susceptibility are quite different, where the Mg–O bond accounts for 58.36% of the total bond susceptibility in this situation, illustrating that the Mg–O bond is indispensable for dielectric polarization. First principles calculation also shows that the [MgO_6] octahedra make large contributions to dielectric loss, while P–V–L bond theory indicates that W–O bonds are indispensable in structural stability. This difference may possibly be related to the boundary condition constraints in the establishment of the model. Therefore, the theoretical conclusions must be verified through experiments on Mg site and W site substitutions to give more precise results.

The discrepancy between the two structures may possibly lie in structural differences and ionic occupancies. From this section, it can be concluded that although both belong to complex perovskites, differences in structures, coordination environment and effective valence electron number of ions together lead to different bond parameters and different contributing sources to bond susceptibility and lattice energy.

This conclusion is similar in cubic $Li_{2x}Mg_{1-x}Ti_xO_{1+2x}$ (x = 1/4, 2/5 and 1/2) systems that although all of them are subject to a cubic structure and have a similar bonding environment, a discrepancy in ionic occupancy results in a different bond susceptibility. By comparing the bond susceptibility, lattice energy and dielectric properties of $Ba(Mg_{1/3}Ta_{2/3})O_3$ and $Ba(Mg_{1/2}W_{1/2})O_3$ systems in Table 16, one can clearly find from Table 16 that there is also a close relationship between bond

Table 15 Bond ionicity, lattice energy, and bond susceptibility in $Ba(Mg_{1/2}W_{1/2})O_3$ system

Bond type	f_i (%)	U (kJ mol^{-1})	χ^μ	F^μ	χ	$\chi/\sum\chi$ (%)
Ba–O	95.6	4627	0.71	0.67	0.47	30.12
Mg–O	77.6	3756	5.49	0.17	0.91	58.36
W–O	91.3	37 319	1.08	0.17	0.18	11.51

Table 16 Comparisons of bond susceptibility, lattice energy and microwave dielectric properties of complex perovskite $Ba(Mg_{1/3}Ta_{2/3})O_3$ and $Ba(Mg_{1/2}W_{1/2})O_3$ systems

System	χ	U_{total} (kJ mol^{-1})	ε_r	$Q \times f$ (GHz)
$Ba(Mg_{1/3}Ta_{2/3})O_3$	1.755	58 632	24	250 000
$Ba(Mg_{1/2}W_{1/2})O_3$	1.566	45 702	17	42 000

susceptibility, lattice energy and microwave dielectric properties, suggesting that bond features may also be crucial for intrinsic dielectric properties.

4.10 Monoclinic wolframite structure

Wolframite-type $AZrB_2O_8$ (A = Mn, Zn, Mg, Co, Ni; B = Nb, Ta) is crystallized as a monoclinic structure with a space group of $P2/c$ (13).[213] As mentioned in section 4.8, the appearance of $[NbO_6]$ units is beneficial for microwave dielectric properties, which is also the case for a wolframite structure. For instance, a $ZnZrNb_2O_8$ ceramic has a moderate ε_r value of 29.27, a high $Q \times f$ value of about 55 460 GHz, and a negative τ_f value of *ca.* −77.21 ppm per °C. Improvements in the $Q \times f$ value have been reported with ionic modification on the cation site: *e.g.* small amounts of Ni^{2+} cation (0.08 mol) on the Zn site greatly improve the $Q \times f$ value to 73224 GHz.[214] A Ti site replaced by a Ge^{4+} cation (0.2 mol) is beneficial for the development of the $Q \times f$ value to 80493 GHz.[215] An Nb site partially substituted by Ta^{5+} and Sb^{5+} cations also testified to positive effects on the $Q \times f$ value (Sb = 0.08 mol, $Q \times f$ = 89 400 GHz).[216] Therefore, structural impacts, especially the evolution of bond features in an $AZrB_2O_8$ monoclinic solid solution, may be crucial for discussing the structure–property relationship.

4.10.1 A site difference in $AZrNb_2O_8$ (A = Mn, Zn, Mg, Co). The monoclinic structure of an $AZrNb_2O_8$ system is shown in Fig. 37.[217] A and Zr atoms are in the 2f Wyckoff position while Nb is in a 2e site. All the cations are six-fold coordinated, forming structural basic units of $[MO_6]$ octahedra (M = A, Zr, Nb). Based on the coordination environments, the binary bonding formula is expressed as:

$$AZrNb_2O_8 = A_{1/3}O(1)_{2/3} + A_{1/3}O(2)^1_{2/3} + A_{1/3}O(2)^2_{2/3} + Zr_{1/3}O(1)_{2/3} + Zr_{1/3}O(2)^1_{2/3} + Zr_{1/3}O(2)^2_{2/3} + Nb_{2/3}O(1)^1_{4/3} + Nb_{2/3}O(1)^2_{4/3} + Nb_{2/3}O(2)_{4/3}$$

where the effective valence electron numbers of O anions in A–O, Zr–O and Nb–O bonds are considered to be 3, 6 and 7.5, respectively. The coordination number and charge distribution can be generalized as in Fig. 38.[218]

Due to the difference in ionic radii of A-site cations (IR values for Mn, Zn, Mg, Co at CN = 6 are 0.83, 0.74, 0.72, 0.65 Å), the V_{cell} and chemical bond lengths after Rietveld refinement present a declining trend from A = Mn to Co elements. Comparisons between bond ionicity, lattice energy, and microwave dielectric properties are listed in Table 17.[218] The largest bond ionicity is shown in Nb–O bonds, followed by that in Zr–O and A–O bonds. The average f_i for all types of bonds present a declining trend from 76.212% to 76.146%, corresponding to a decrease in dielectric polarization. As a result, the ε_r value declines from A = Mn to Co. This result indicates that variation in bond ionicity in different A site situations possibly affects the ε_r value. The largest total lattice energy value is found in A = Mg (52335 kJ mol^{-1}), and then A = Zn (52297 kJ mol^{-1}), while the smallest value is shown in A = Mn (51936 kJ mol^{-1}), suggesting that the internal losses in A = Zn, Mg may be smaller than those in A = Mn, Co. By using the far-infrared reflectivity spectra, it is also found that the fitting of intrinsic loss by a classical three-parameter model of A = Zn, Mg systems is much smaller than those in A = Mn, Co systems.

NiO (0–0.08 mol) was used to partially replace the Zn sites in $ZnZrNb_2O_8$ ceramics, and the results also provide evidence

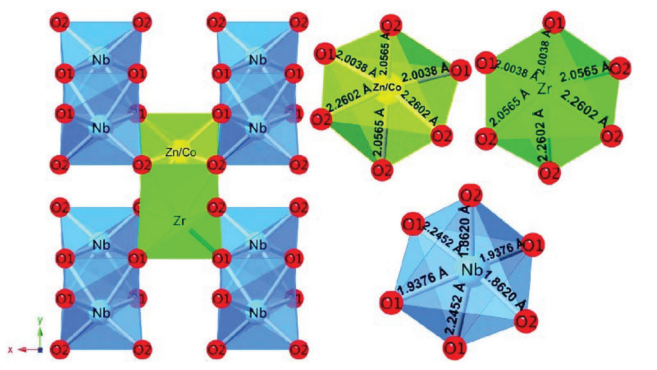

Fig. 37 Schematic representation of the $Zn_{1-x}Co_xZrNb_2O_8$ (2 × 2 × 2) supercell and the A-site (A = Zn^{2+}/Co^{2+}, Zr^{4+}) and B-site (B = Nb^{5+}) oxygen octahedrons of $Zn_{0.94}Co_{0.06}ZrNb_2O_8$ with their bond lengths (reproduced from ref. 217 with permission from the Royal Society of Chemistry).

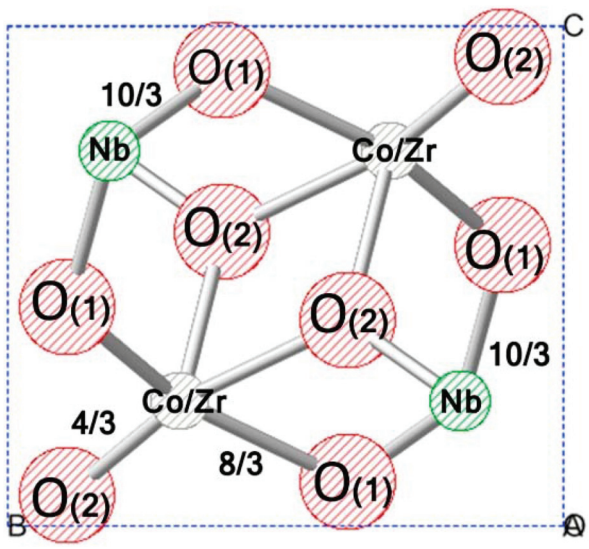

Fig. 38 The coordination number and charge distribution of ions in $AZrNb_2O_8$ ceramics (here A = Co ions) (reprinted with permission from ref. 218. Copyright 2016 Elsevier).

Table 17 Comparisons between bond ionicity, lattice energy, and microwave dielectric properties of $AZrNb_2O_8$ ceramics (A = Mn, Zn, Mg, Co)

A-site	Bond type	Af_i (%)	U (kJ mol^{-1})	ε_r	$Q \times f$ (GHz)
Mn	Mn–O	64.11	3212	27.56	27 400
	Zr–O	80.51	11 673		
	Nb–O	84.02	37 051		
Zn	Zn–O	64.02	3233	27.08	58 000
	Zr–O	80.48	11 744		
	Nb–O	83.99	37 320		
Mg	Mg–O	63.92	3255	26.55	68 000
	Zr–O	80.47	11 824		
	Nb–O	84.05	37 256		
Co	Co–O	64.00	3233	25.59	47 100
	Zr–O	80.47	11 744		
	Nb–O	83.98	37 320		

that the decrease in f_{iNb-O} value is responsible for the drop in the ε_r value, and the lattice energy consistently increases along with structural stability.[214]

4.10.2 Ionic doping on Zr/Nb sites in $AZrNb_2O_8$ (A = Zn, Mg). Due to the excellence of the microwave dielectric properties in $AZrNb_2O_8$ (A = Zn, Mg) systems, a large number of studies have developed around the goal of further improving the $Q \times f$ value. Just as mentioned in section 4.10.1, the improvement in structural stability may possibly be positive for the development of the $Q \times f$ value. Thus, many studies around the $MgZrNb_2O_8$ system seek whether a similar relationship exists and what types of substitution sources are suitable.

For instance, taking the Zr site as an example, the cell volume is obviously decreasing when the Zr site is partially substituted by a Ge^{4+} cation in an $Mg(Zr_{1-x}Ge_x)Nb_2O_8$ (x = 0–0.4) system, which is caused by its smaller ionic radius of 0.53 than the 0.72 of a Zr^{4+} cation. Consequently, the $Q \times f$ value is greatly enhanced from 64 784 GHz to 80493 GHz.[215] The Sn^{4+} cation (IR = 0.69 at CN = 6) replacing a Zr site in an $MgZr_{0.85}Sn_{0.15}Nb_2O_8$ ceramic also shows that lattice energy is advantageous to the $Q \times f$ value, where the largest U_{total} corresponds to the highest $Q \times f$ value of 94014 GHz.[219]

For Nb site substitution, Ta^{5+}, Sb^{5+}, $(Sn_{1/2}W_{1/2})^{5+}$ cations are used to study the structure–property relationship based on P–V–L bond theory: *e.g.* in $ZnZr(Nb_{1-x}A_x)_2O_8$ (A = Ta, Sb) ceramics,[216] an increasing content of donor reduces the cell volume, and the results show that a decrease in the Af_i value for all types of bonds in a Ta^{5+} doping system (from 76.19% to 76.03%) should be responsible for the decline in ε_r value (from 26.7 to 25.7). Also, the increase in lattice energy improves the $Q \times f$ value (from 65 100 GHz to 89 400 GHz). In an $MgZrNb_2O_8$ system, the Ta^{5+} cation is also proved to be an effective source to improve the lattice energy and $Q \times f$ value, and the average bond ionicity Af_i value decreases similarly with the ε_r value.[220] Complex $(Sn_{1/2}W_{1/2})^{5+}$ cation replacement for the Nb site in $MgZrNb_2O_8$ system (0–0.06 mol) is also confirmed by the similar variation tendency.[221]

From the above-mentioned reports, it can be concluded that the variation in bond ionicity may be proportional to the dielectric polarization, and an improvement in lattice energy actually enhances the structural stability and further improves the $Q \times f$ value.

4.11 ZnO–TiO_2–Nb_2O_5 ternary systems

The ternary system of ZnO–TiO_2–Nb_2O_5 was firstly introduced by Baumgarte and Blachnik in 1992.[222] It is proposed that in TiO_2–$Zn_{1/3}Nb_{2/3}O_2$, the rutile TiO_2 phase appears when the molar content of $Zn_{1/3}Nb_{2/3}O_2$ is lower than 58%, ixiolite $ZnTiNb_2O_8$ appears when the content is in the range of 69% to 85%, and columbite $ZnNb_2O_6$ is formed when the content is higher than 93%. In 2008, Kim first reported the formation and microwave dielectric properties of the $Zn_{0.15}Nb_{0.3}Ti_{0.55}O_2$ phase with a rutile structure.[223] It should be noted that all the above systems contain Zn, Ti, and Nb elements and the molar ratio of Zn : Nb remains unchanged at about 1 : 2. Further in-depth study shows that the above materials can be understood as the coordinated substitution of Ti^{4+} in TiO_2 by $(Zn_{1/3}Nb_{2/3})^{4+}$ ions: $(Zn_{1/3}Nb_{2/3})_xTi_{1-x}O_2$ (x = 0.45, 0.75, 1). Phase structures vary with the increase in x value, as indicated in the ternary phase diagram of Fig. 39.

This ZnO–TiO_2–Nb_2O_5 system has attracted much attention because of the excellence of its dielectric properties. For instance, columbite $ZnNb_2O_6$ has a considerable $Q \times f$ value of about 83 700 GHz with a moderate ε_r value of about 25.[89] Both ixiolite $ZnTiNb_2O_8$ and rutile $Zn_{0.15}Nb_{0.3}Ti_{0.55}O_2$ ceramics can be well-sintered at relatively low temperatures with various great dielectric performances (ixiolite: ST = 1100 °C, ε_r = 37.21, $Q \times f$ = 41 231 GHz; rutile: ST = 1050 °C, ε_r = 94.35, $Q \times f$ = 10 889 GHz).[224] Thus, many investigations have been undertaken to not only further improve the dielectric properties but also to decrease the sintering temperature, exploring applications in LTCC applications.

From the point of view of crystal structure and P–V–L bond theory, an attractive feature of this system is that three distinc-

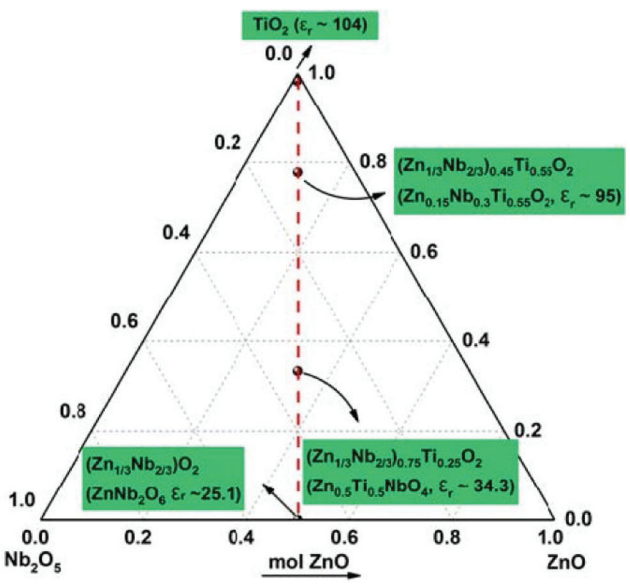

Fig. 39 Ternary ZnO–TiO_2–Nb_2O_5 systems.

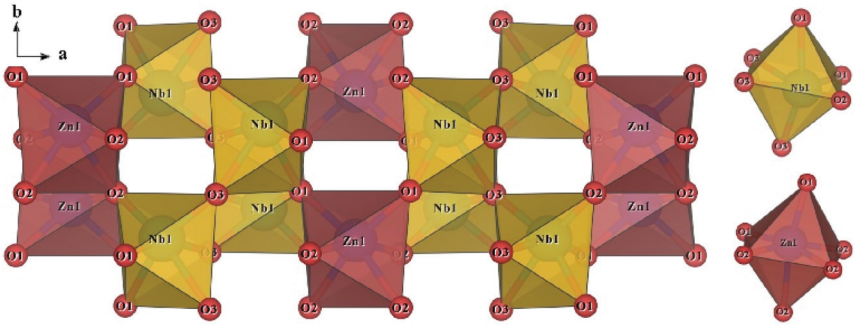

Fig. 40 Crystal structure of columbite $ZnNb_2O_6$ (reprinted with permission from ref. 225. Copyright 2019 John Wiley and Sons).

tive crystal structural types appear with the variations in mole contents of the $(Zn_{1/3}Nb_{2/3})^{4+}$ ions. That is to say, the ionic occupancy is presented with large differences, which causes the different bond parameters. And taking this effect into consideration, one may have a better understanding of the structure–property relationship in the ZnO–TiO_2–Nb_2O_5 system.

4.11.1 Variations in ionic occupancy in $(Zn_{1/3}Nb_{2/3})_xTi_{1-x}O_2$ (x = 0.45, 0.75, 1). Just as indicated, variations in complex ionic occupancy lead to different phase compositions, which directly causes various bond parameters. For x = 1, a columbite orthorhombic $ZnNb_2O_6$ structure with a space group of *Pbcn*(60) is formed, and its crystal structural parameters are reported as: a = 14.213 Å, b = 5.732 Å, c = 5.040 Å, V_{cell} = 410.60 Å^3. The crystal structure is shown in Fig. 40,[225] where Zn and Nb atoms occupy 4c and 8d Wyckoff positions, and the structure consists of $[ZnO_6]$ and $[NbO_6]$ octahedral units, and it is arranged as Zn–Nb–Nb–Zn–Nb–Nb⋯ along the *a*-axis orientation. A $[ZnO_6]$ octahedron links with an $[NbO_6]$ octahedron through sharing a vertex, while both of them interconnect with each other *via* a shared edge when the x value changes to x = 0.75, and an ixiolite orthorhombic $ZnTiNb_2O_8$ phase exists. This phase can also be treated as the formation of an equimolar solid solution between $ZnNb_2O_6$ and TiO_2. However, it should be noted that the disappearance of a superlattice diffraction peak (040) indicates the complete disorder of the solution structure, where Zn/Ti/Nb atoms are randomly distributed in 4c sites, coordinating with six oxygens to form $[MO_6]$ (M = Zn/Ti/Nb) octahedra, as shown in Fig. 41. Furthermore, when the x value reaches 0.45, the phase structure changes into rutile tetragonal $Zn_{0.15}Nb_{0.3}Ti_{0.55}O_2$, where the cations are also six-fold coordinated and in a 2a site.

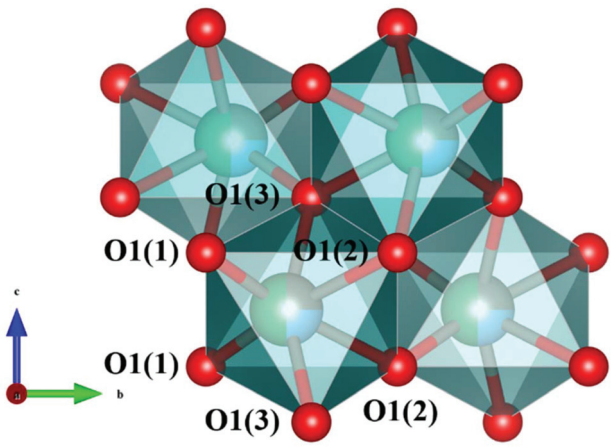

Fig. 41 Crystal structure of ixiolite $ZnTiNb_2O_8$.

It is necessary to investigate the structural impacts *via* P–V–L bond theory due to the three types of crystal structures showing large diversities in microwave dielectric properties. Based on a consideration of bonding environments and charge distributions, the binary bonding formulas for the three structures can be summarized as:[224,225]

$$\begin{aligned}(\text{Columbite } x=1)ZnNb_2O_6 &= Zn_{1/3}O1_{2/3} + Zn_{1/3}O2(1)_{2/3} \\ &+ Zn_{1/3}O2(2)_{2/3} + Nb_{1/3}O1(1)_{2/3} + Nb_{1/3}O1(2)_{2/3} \\ &+ Nb_{1/3}O2_{2/3} + Nb_{1/3}O3(1)_{2/3} + Nb_{1/3}O3(2)_{2/3} \\ &+ Nb_{1/3}O3(3)_{2/3}\end{aligned}$$

$$\begin{aligned}(\text{Ixiolite } x=0.75)ZnTiNb_2O_8 &= Zn_{1/3}O1(1)_{2/3} + Zn_{1/3}O1(2)_{2/3} \\ &+ Zn_{1/3}O1(3)_{2/3} + Ti_{1/3}O1(1)_{2/3} + Ti_{1/3}O1(2)_{2/3} + Ti_{1/3}O1(3)_{2/3} \\ &+ Nb_{2/3}O1(1)_{4/3} + Nb_{2/3}O1(2)_{4/3} + Nb_{2/3}O1(3)_{4/3}\end{aligned}$$

$$\begin{aligned}(\text{Rutile } x=0.45)Zn_{0.15}Nb_{0.3}Ti_{0.55}O_2 &= Zn_{0.05}O1(1)_{01} \\ &+ Zn_{0.1}O1(2)_{0.2} + Ti_{0.55/3}O1(1)_{1.1/3} + Ti_{1.1/3}O1(2)_{2.2/3} \\ &+ Nb_{0.1}O1(1)_{0.2} + Nb_{0.2}O1(2)_{0.4}\end{aligned}$$

Detailed comparisons between bond ionicity and lattice energy can be found in Table 8S in ESI.† Here we summarize the average bond ionicity, total lattice energy and microwave dielectric properties of $(Zn_{1/3}Nb_{2/3})_xTi_{1-x}O_2$ (x = 0.45, 0.75, 1) systems in Table 18. From Table 8S† and Table 18, it can be seen that the columbite structure is presented with a much lower average bond ionicity Af_i value, while the largest Af_i is shown in the rutile structure. More specifically, f_{iNb-O} bonds in the three types of structure are largest, followed by Ti–O bonds and Zn–O bonds. The lattice energy U value for each bond also shows similar variation. The largest U_{total} in the columbite $ZnNb_2O_6$ system shows excellent structural stability; correspondingly, its intrinsic loss would be a minimum. It is proved

Table 18 Comparisons between average bond ionicity, total lattice energy and microwave dielectric properties in $(Zn_{1/3}Nb_{2/3})_xTi_{1-x}O_2$ (x = 0.45, 0.75, 1) systems

x (mol)	Structure	Af_i (%)	U_{total} (kJ mol^{-1})	ε_r	$Q \times f$ (GHz)
1	C	74.04	13 532	23.1	72 885
0.75	I	76.06	13 145	37.2	41 231
0.45	R	76.52	12 872	94.4	10 889

C, I and R refer to columbite, ixiolite and rutile structures. The U value is normalized based on the formula $(Zn_{1/3}Nb_{2/3})_xTi_{1-x}O_2$.

that Nb–O bonds make about a 68% contribution to dielectric polarization in the $ZnNb_2O_6$ system, emphasizing the importance of Nb–O bonds.

Furthermore, far-infrared reflectivity spectra were applied to further testify to the intrinsic dielectric properties in $(Zn_{1/3}Nb_{2/3})_xTi_{1-x}O_2$ (x = 0.45, 0.75, 1) systems; taking x = 1 as an example, the infrared spectrum is presented in Fig. 42.[225] The real part and imaginary part of the complex dielectric constant fitted using a classical three-parameter model (LTPC) and a four-parameter semiquantum model (FPSQ) are shown in Fig. 43.[225] Both these fitting processes indicate an intrinsic low ε_r value of about 23.3 and an ultra-high $Q \times f$ value of 122 807 GHz. Similarly, intrinsic dielectric properties for ixiolite $ZnTiNb_2O_8$ (ε_r = 32.16, $Q \times f$ = 40 151 GHz) and rutile $Zn_{0.15}Nb_{0.3}Ti_{0.55}O_2$ (ε_r = 97.63, $Q \times f$ = 10 443 GHz) are also close to experimental values, indicating that the intrinsic factor may have a dominant effect on microwave dielectric performance.[224]

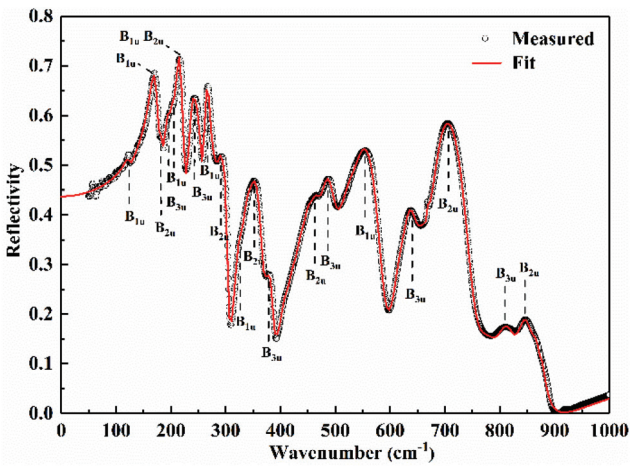

Fig. 42 Experimental and fitted far-infrared reflectivity spectra of $ZnNb_2O_6$ ceramic (reprinted with permission from ref. 225. Copyright 2019 John Wiley and Sons).

4.11.2 Ionic modification in $(Zn_{1/3}Nb_{2/3})_xTi_{1-x}O_2$ (x = 0.45, 0.75, 1). In the three typical structures, columbite $ZnNb_2O_6$ and ixiolite $ZnTiNb_2O_8$ ceramics are mostly studied for their considerable dielectric properties with moderate ε_r values. However, a number of investigations have been undertaken to improve the negative τ_f values (−52 ppm per °C for ixiolite). For instance, in $ZnTiNb_2O_8$ ceramics, Mg^{2+}, Co^{2+}, Ni^{2+}, Ca^{2+}/Sn^{4+} and Ta^{5+} cations were used to substitute the cation site, and most studies have shown that the ceramic system with ionic doping presents an increase in ε_r value and the τ_f value could be adjusted to the positive side. Interestingly, based on previous reports, it is the formation of secondary rutile $Zn_{0.15}Nb_{0.3}Ti_{0.55}O_2$ that regulates the dielectric properties.[226–229]

In our previous study, combined with the phase diagram, $Zn_{0.15+0.35x}Ti_{0.55-0.05x}Nb_{0.3+0.7x}O_{2+2x}$ ceramics (shortened to xZTN-(1-x)ZNT) were planned through directly introducing $Zn_{0.15}Nb_{0.3}Ti_{0.55}O_2$ into $Zn_{0.5}Ti_{0.5}NbO_4$ ceramics.[224] The purpose of this design is to understand the phase evolution and variations in bond features in both orthorhombic and tetragonal solid solution under the change in ionic occupancies in the absence of other donors. As shown by the XRD patterns in Fig. 44, orthorhombic and rutile solid solutions are formed in the ranges of x = 0–0.2 and x = 0.65–1. An increase in x value obviously leads to an expansion in cell volume and

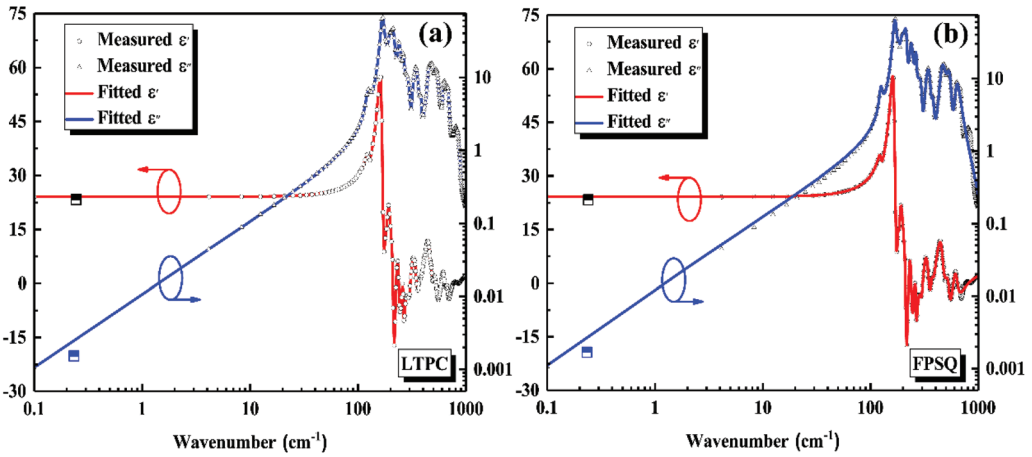

Fig. 43 Real $\varepsilon'(\omega)$ and imaginary parts $\varepsilon''(\omega)$ of relative permittivity after (a) LTPC and (b) FPSQ mode fitting. FPSQ, four parameter semiquantum model; LTPC, Lorentz three parameter semiquantum model (reprinted with permission from ref. 225. Copyright 2019 John Wiley and Sons).

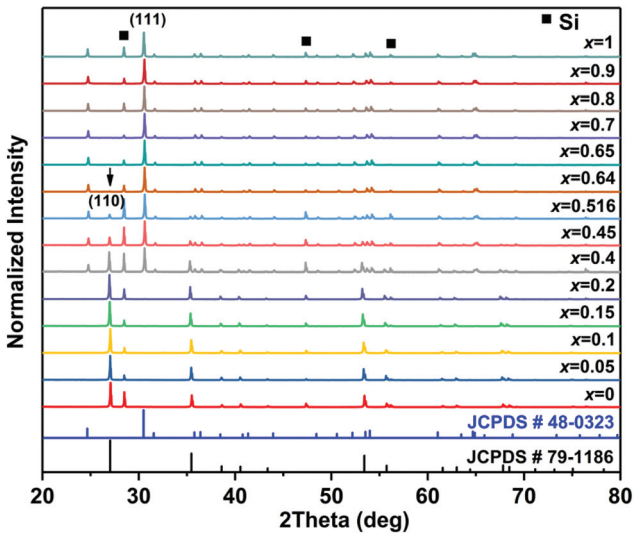

Fig. 44 X-ray diffraction patterns for all the compositions of xZTN-(1–x)ZNT ceramics for x = 0–1 (reprinted with permission from ref. 224. Copyright 2018 American Chemical Society).

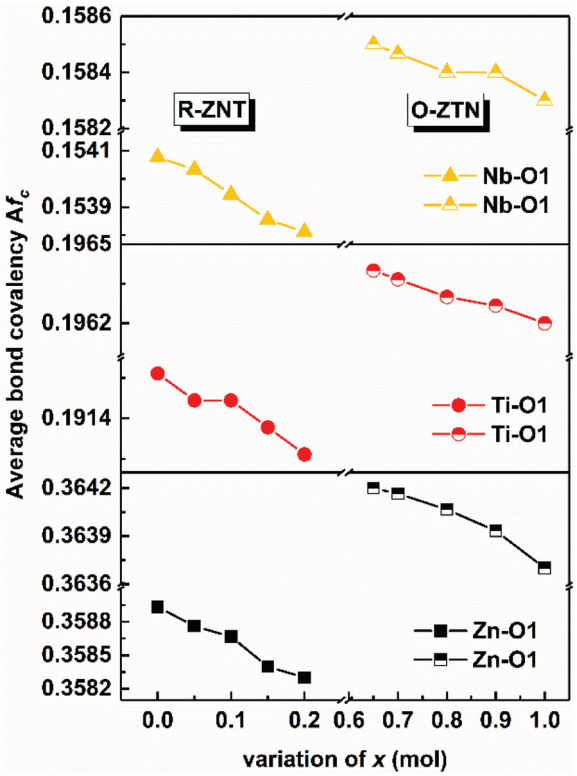

Fig. 45 Average bond covalency as a function of the x value in the R-ZNT phase and O-ZTN phase (reprinted with permission from ref. 224. Copyright 2018 American Chemical Society).

an enlargement in bond length. In section 4.3, it is noticed that occupancies in Li, Mg and Ti cations have different impacts on bond parameters. Thus, based on consideration of P–V–L bond theory, the binary bonding formula A_mB_n should vary with ionic occupancy, which can be found in Table 9S in ESI,† and the m value makes a large difference even in the same structure. Variations in average bond covalency are shown in Fig. 45. An increase in the x value in solid solution regions leads to a monotonous decrease in Af_c value for all types of bonds. However, a small variation in Af_c value is not enough to support the decrease in dielectric polarizability. Therefore, as indicated by the drop in total bond susceptibility value from 4.04 to 2.98 in the rutile structure and from 3.34 to 2.84 in the ixiolite structure, it is confirmed that the drop in average bond covalency is responsible for the decline in the ε_r value. Additionally, in the rutile solid solution, the variations in $d_{apical}/d_{equatorial}$ reflect the cation rattling and ε_r value. Similarly, the ratio varying from 1.0089 to 1.0083 still supports the decrease in dielectric polarization. Intrinsically, the lattice energy shows a linearly increasing trend in both rutile and ixiolite solid solutions, showing an improvement in structural stability. It can clearly be seen that with the variation in Zn/Ti/Nb cations, the $Q \times f$ value is reasonably improved (from 10 889 to 13 017 GHz in rutile and from 42 181 to 47 829 GHz in ixiolite).

It can be concluded that in orthorhombic $Zn_{0.5}Ti_{0.5}NbO_4$ and tetragonal $Zn_{0.15}Nb_{0.3}Ti_{0.55}O_2$ solid solutions, when the system is doped with larger sized cations, variations in dielectric polarization are affected by bond covalency.

Another case in point is the $Zr_{1-x}Zn_{0.5x}Ti_{1-0.5x}Nb_xO_4$ ceramic, where both $ZrTiO_4$ and $Zn_{0.5}Ti_{0.5}NbO_4$ belong to the same orthorhombic structure. With the increase in x value, both volume cell and bond length are increased. The covalency of all types of bonds declines in the range x = 0.1–0.5, corresponding to a drop in bond susceptibility. As a result, the ε_r value decreases as well. Similarly, the structural stability of $Zr_{1-x}Zn_{0.5x}Ti_{1-0.5x}Nb_xO_4$ is improved from 24 150 to 25200 kJ mol^{-1}, accompanied by an increase in $Q \times f$ value from 24 000 to 30558 GHz.[230]

In the rutile $Zn_{0.15}Nb_{0.3}Ti_{0.55}O_2$ system, the larger sized Zr^{4+} cation was used for Ti site substitution[231] in the $Zn_{0.15}Nb_{0.3}(Ti_{1-x}Zr_x)_{0.55}O_2$ system, where the rutile phase transforms into the orthorhombic in the range x = 0.3–0.4. Still, the increase in cell volume and bond length eventually leads to a drop in covalency for all types of bonds, and the theoretical and experimental ε_r values decrease.

From the above cases, one can find that when the cation sites in $Zn_{0.5}Ti_{0.5}NbO_4$ and $Zn_{0.15}Nb_{0.3}Ti_{0.55}O_2$ systems are replaced with larger sized ions, there is a proportional relationship between average bond covalency and ε_r value.

However, different situations occur if the cation site is doped with smaller sized ions. For instance, in our previous study, Ta_2O_5 was chosen as a substitution source to replace Nb sites in a rutile $Zn_{0.15}Nb_{0.3-x}Ta_xTi_{0.55}O_2$ ($0 \le x \le 0.3$) system,[232] where an infinite solid solution can be formed because of the close size of the radii between Nb^{5+} and Ta^{5+} cations. With the substitution of Ta^{5+} cations, cell volume and bond length decrease, leading to decreasing tendencies for all types of bond ionicity. Due to the asynchronous change in bond length, the ratio of $d_{apical}/d_{equatorial}$ shows a decreasing trend

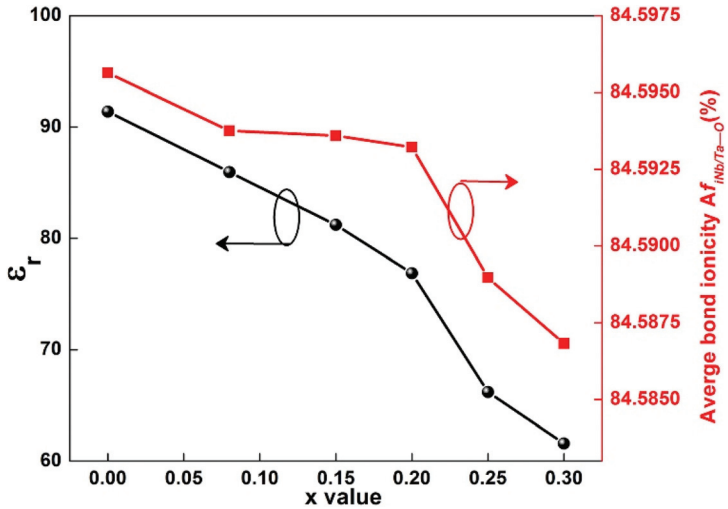

Fig. 46 ε_r and average Nb-site bond ionicity of $Zn_{0.15}Nb_{0.3-x}Ta_xTi_{0.55}O_2$ ($0 \le x \le 0.3$) ceramics (reprinted with permission from ref. 232. Copyright 2019 Elsevier).

from 1.0086 to 1.0075, suggesting a decreasing trend for the ε_r value. Thus, the bond ionicity is reasonably correlated with the ε_r value, as indicated in Fig. 46. The lattice energy consistently increases along with the x value in x = 0–0.2, corresponding to a great improvement in $Q \times f$ value from 11 012 to 22 050 GHz.

Furthermore, Luo used complex ions $(Al_{0.5}Nb_{0.5})^{4+}$ with small size to partially replace Ti sites in a $ZnTi_{1-x}(Al_{0.5}Nb_{0.5})_xNb_2O_8$ system and found that increasing structural stability has a positive relationship with bond covalency, where a high bond covalency indicates a low dielectric loss. By using THz time domain spectra to study the intrinsic dielectric properties, it is found that the ε_r value and dielectric loss in the THz region both present a declining trend; the variation of ε_r value is shown in Fig. 47.[233]

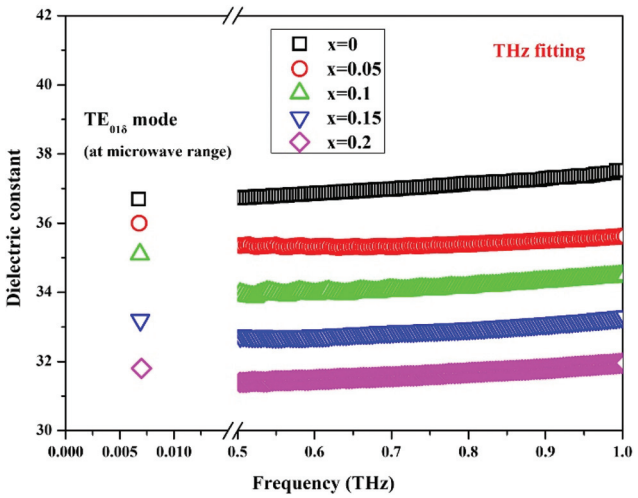

Fig. 47 Dielectric constant of $ZnTi_{1-x}(Al_{0.5}Nb_{0.5})_xNb_2O_8$ ceramics in the microwave and terahertz range (reprinted with permission from ref. 233. Copyright 2019 John Wiley and Sons).

We may infer from the reports that in $Zn_{0.5}Ti_{0.5}NbO_4$ and $Zn_{0.15}Nb_{0.3}Ti_{0.55}O_2$ systems, variations in bond covalency should play a dominant role in determining the ε_r value when the cation site is replaced with large sized ions; otherwise, it is the bond ionicity value that is proportional to dielectric polarization. Still, this conjecture should be tested with large amounts of experimental results in the future.

4.12 Tetragonal trirutile $A_{0.75}Ti_{0.75}Ta_{1.5}O_6$ structure (A = Co, Ni, Zn, Mg)

It is reported that in the substitution of the $ZnTi(Nb_{1-x}Ta_x)_2O_8$ system, the τ_f value is largely compensated for due to the existence of trirutile phases. Recently, pure tetragonal trirutile ceramics with chemical formula $A_{0.75}Ti_{0.75}Ta_{1.5}O_6$ have been investigated from the point of view of crystal structure and chemical bond features.

In general, the trirutile structure is regarded as an enlargement of the rutile structure along the c-axis length. Typical types of trirutile structures are shown in Fig. 48.[234] All the cations are surrounded by six oxygens. However, the bond types and ionic occupancies are presented with large differences even though they share the same structural type, leading to different bonding formula expressions (A = Ni is similar to A=Co):[234]

$$Co_{0.75}Ti_{0.75}Ta_{1.5}O_6 = Co_{1/4}O^1_{1/2} + Co_{1/2}O^2_1 + Ti_{1/4}O^1_{1/2} + Ti_{1/2}O^2_1 + Ta^1_{1/12}O^1_{1/6} + Ta^1_{1/6}O^2_{1/3} + Ta^2_{5/12}O^1_{5/6} + Ta^2_{10/12}O^2_{5/3}$$

$$Zn_{0.75}Ti_{0.75}Ta_{1.5}O_6 = Zn^1_{2/15}O^1_{4/15} + Zn^1_{4/15}O^2_{8/15} + Ti^1_{2/15}O^1_{4/15} + Ti^2_{4/15}O^2_{8/15} + Ta^1_{1/15}O^1_{2/15} + Ta^1_{2/15}O^2_{4/15} + Zn^2_{7/60}O^1_{7/30} + Zn^2_{7/30}O^2_{7/15} + Ti^2_{7/60}O^1_{7/30} + Ti^2_{7/30}O^2_{7/15} + Ta^2_{13/30}O^1_{13/15} + Ta^2_{13/15}O^2_{26/15}$$

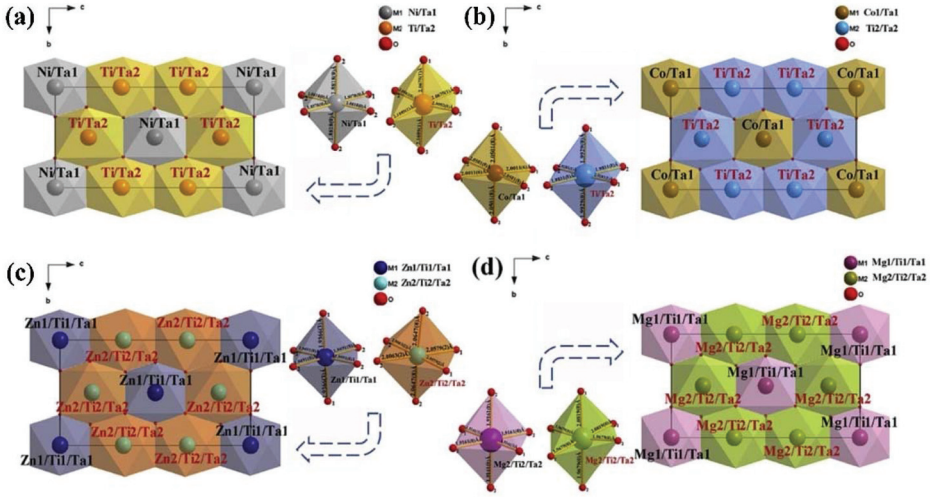

Fig. 48 The schematic diagram of the crystal structure of (a) $Ni_{0.75}Ti_{0.75}Ta_{1.5}O_6$, (b) $Co_{0.75}Ti_{0.75}Ta_{1.5}O_6$, (c) $Zn_{0.75}Ti_{0.75}Ta_{1.5}O_6$, (d) $Mg_{0.75}Ti_{0.75}Ta_{1.5}O_6$ ceramics (reprinted with permission from ref. 234. Copyright 2020 Elsevier).

$$Mg_{0.75}Ti_{0.75}Ta_{1.5}O_6 = Mg^1_{13/100}O^1_{13/50} + Mg^1_{13/50}O^2_{13/25} + Ti^1_{13/100}O^1_{13/50} + Ti^1_{13/50}O^2_{13/25} + Ta^1_{11/150}O^1_{11/75} + Ta^1_{11/75}O^2_{22/75} + Mg^2_{3/25}O^1_{6/25} + Mg^2_{6/25}O^2_{12/25} + Ti^2_{3/25}O^1_{6/25} + Ti^2_{6/25}O^2_{12/25} + Ta^2_{32/75}O^1_{64/75} + Ta^2_{64/75}O^2_{128/75}$$

Therefore, it is found that Ta–O bonds have larger bond ionicity values than Ti–O and A–O bonds. The largest lattice energy also shows the same tendency. Combined with the bond susceptibility value, this indicates that Ta–O bonds provide the majority contributions of about 60% and 70% to dielectric polarization and structural stability, illustrating the significance of Ta–O bonds in a trirutile structure.[235] In the synthesis of $A_{0.75}Ti_{0.75}Ta_{1.5}O_6$ (A = Co, Ni, Zn, Mg) ceramics, Wang also found a proportional relationship between the bond ionicity value of Ta–O bonds and the ε_r value, where with the increase in ionic radius, the increase in f_{iTa-O} value is mainly responsible for the ε_r value. The lattice energy, showing the maximum value in the A = Ni system (60941 kJ mol^{-1}), also corresponds to the largest $Q \times f$ value (25 051 GHz).

5. Summary and future work

The primary goal of applying P–V–L bond theory to microwave dielectric ceramics is to provide guidance for the exploration of practical novel systems and ion doping modifications on the basis of comprehensive knowledge of crystal structure and chemical bond properties. With the help of the binary bonding formula theory of complex polycrystals, it is very advantageous to provide basic chemical bond characteristics, such as bond ionicity, bond covalency and bond susceptibility. By applying these fundamental traits, the structural evolution and developments of microwave dielectric properties can be explained reasonably well. For instance, a preliminary understanding of the polarization ability and structural stability of crystals can be gained on the condition of knowing the crystal structure and structural parameters alone. Intrinsically, the crystal structure would be more lattice stable with a higher lattice energy. Far-infrared reflectance spectroscopy and THz time-domain spectroscopy may possibly be effective methods for examining the evolution of intrinsic dielectric properties. On the other hand, some conjectures based on experimental results are proposed, which require a large number of experiments to verify and supplement them in the future. For instance, it is found that Mg sites being doped using larger radius ions results in a similar variation tendency between bond ionicity and dielectric constant, while smaller radius ion doping at Ti sites is beneficial for improving the structural stability of and reducing the internal dielectric loss in cubic rock salt $Li_2Mg_3TiO_6$ systems. For most niobate systems, substitution of Nb sites by Ta ions obviously improves the structural stability of the crystal and further positively affects the $Q \times f$ value. Therefore, with the conclusions put forward, P–V–L bond theory can provide ideas for subsequent ion doping in other systems.

However, P–V–L bond theory is predictable theoretically, while the actual situation is still subject to influences from external factors, such as the experimental/fabrication process. Therefore, the use of bond theory is meaningful on the premise of improving the sinterability of materials and reducing the loss from external processes (such as the use of spark plasma sintering). Furthermore, we know that chemical bonds in polyhedra will be in stretched or compressed states, leading to discrepancies in ionic polarizabilities deviating from theoretical ionic polarization, as a result, affecting the dielectric constant of dielectric materials. In a binary system, the specific polarization ability of each kind of ion in a specific crystal can be determined according to bond theory given the crystal

structure and dielectric constant. With the help of the binary bonding formula and calculation of bond susceptibility, the dielectric constant of a bond can be used to theoretically calculate the ionic polarizability and volume polarizability of the ions in the complex crystal. Combined with normalized chemical bond analysis, the variations in specific polarizability in the crystal can be quantitatively characterized, which is of great significance to discussing the change in dielectric polarization in microwave dielectric ceramics.

Conflicts of interest

There are no conflicts to declare.

Acknowledgements

Reproduced from ref. 199 with permission from the PCCP Owner Societies; Reproduced from ref. 217 with permission from the Royal Society of Chemistry. The authors acknowledge financial supports from the National Natural Science Foundation of China (Grant. 51872037). The authors would also like to thank Prof. Shu Zhang for her helpful discussions on the P–V–L bond theory.

Notes and references

1 I. M. Reaney and D. Iddles, Microwave Dielectric Ceramics for Resonators and Filters in Mobile Phone Networks, *J. Am. Ceram. Soc.*, 2006, **89**, 2063–2072.
2 M. T. Sebastian, R. Ubic and H. Jantunen, Low-loss dielectric ceramic materials and their properties, *Int. Mater. Rev.*, 2015, **60**, 392–412.
3 M. T. Sebastian, *Dielectric Materials for Wireless Communication*, Elsevier Science, 2008.
4 D. Zhou, L. X. Pang, D. W. Wang and I. M. Reaney, $BiVO_4$ based high k microwave dielectric materials: a review, *J. Mater. Chem. C*, 2018, **6**, 9290–9313.
5 S. J. Penn, N. M. Alford, A. Templeton, X. Wang, M. Xu, M. Reece and K. Schrapel, Effect of Porosity and Grain Size on the Microwave Dielectric Properties of Sintered Alumina, *J. Am. Ceram. Soc.*, 1997, **80**, 1885–1888.
6 Y. Guo, H. Ohsato and K.-I. Kakimoto, Characterization and dielectric behavior of willemite and TiO_2-doped willemite ceramics at millimeter-wave frequency, *J. Eur. Ceram. Soc.*, 2006, **26**, 1827–1830.
7 C. W. Zheng, S. Y. Wu, X. M. Chen and K. X. Song, Modification of $MgAl_2O_4$ Microwave Dielectric Ceramics by Zn Substitution, *J. Am. Ceram. Soc.*, 2007, **90**, 1483–1486.
8 D. J. Barber, K. M. Moulding, J. I. Zhou and M. Li, Structural order in $Ba(Zn_{1/3}Ta_{2/3})O_3$, $Ba(Zn_{1/3}Nb_{2/3})O_3$ and $Ba(Mg_{1/3}Ta_{2/3})O_3$ microwave dielectric ceramics, *J. Mater. Sci.*, 1997, **32**, 1531–1544.
9 C. W. Ahn, H. J. Jang, S. Nahm, H. M. Park and H. J. Lee, Effects of microstructure on the microwave dielectric properties of $Ba(Co_{1/3}Nb_{2/3})O_3$ and $(1-x)Ba(Co_{1/3}Nb_{2/3})O_3-xBa(Zn_{1/3}Nb_{2/3})O_3$ ceramics, *J. Eur. Ceram. Soc.*, 2003, **23**, 2473–2478.
10 M. H. Kim, J. B. Lim, J. C. Kim, S. Nahm, J. H. Paik, J. H. Kim and K. S. Park, Synthesis of $BaCu(B_2O_5)$ Ceramics and their Effect on the Sintering Temperature and Microwave Dielectric Properties of $Ba(Zn_{1/3}Nb_{2/3})O_3$ Ceramics, *J. Am. Ceram. Soc.*, 2006, **89**, 3124–3128.
11 K. S. Hong, I. T. Kim and C. D. Kim, Order-Disorder Phase Formation in the Complex Perovskite Compounds $Ba(Ni_{1/3}Nb_{2/3})O_3$ and $Ba(Zn_{1/3}Nb_{2/3})O_3$, *J. Am. Ceram. Soc.*, 1996, **79**, 3218–3224.
12 W. Y. Lin, R. F. Speyer, W. S. Hackenberger and T. R. Shrout, Microwave Properties of $Ba_2Ti_9O_{20}$ Doped with Zirconium and Tin Oxides, *J. Am. Ceram. Soc.*, 1999, **82**, 1207–1211.
13 J. H. Choy, Y. S. Han, J. H. Sohn and M. Itoh, Microwave Characteristics of BaO-TiO_2 Ceramics Prepared via a Citrate Route, *J. Am. Ceram. Soc.*, 1995, **78**, 1169–1172.
14 T. Takada, S. F. Wang, S. Yoshikawa, S. J. Jang and R. E. Newnham, Effects of Glass Additions on $(Zr,Sn)TiO_4$ for Microwave Applications, *J. Am. Ceram. Soc.*, 1994, **77**, 2485–2488.
15 C. L. Huang and M. H. Weng, Liquid phase sintering of $(Zr,Sn)TiO_4$ microwave dielectric ceramics, *Mater. Res. Bull.*, 2000, **35**, 1881–1888.
16 R. Ubic, I. M. Reaney and W. E. Lee, Microwave dielectric solid–solution phase in system $BaO–Ln_2O_3–TiO_2$ (Ln=lanthanide cation), *Int. Mater. Rev.*, 1998, **43**, 205–219.
17 J. B. Lim, K. H. Cho, S. Nahm, J. H. Paik and J. H. Kim, Effect of $BaCu(B_2O_5)$ on the sintering temperature and microwave dielectric properties of $BaO–Ln_2O_3–TiO_2$ (Ln=Sm, Nd) ceramics, *Mater. Res. Bull.*, 2006, **41**, 1868–1874.
18 Z. Xiong, B. Tang, Z. Fang, C. Yang and S. Zhang, Crystal structure, Raman spectroscopy and microwave dielectric properties of $Ba_{3.75}Nd_{9.5}Ti_{18-z}(Al_{1/2}Nb_{1/2})_zO_{54}$ ceramics, *J. Alloys Compd.*, 2017, **723**, 580–588.
19 Y. Chen, S. Zhang, E. Li, N. Niu and H. Yang, Sintering characteristic and microwave dielectric properties of $0.45Ca_{0.6}Nd_{0.267}TiO_3–0.55Li_{0.5}Nd_{0.5}TiO_3$ ceramics with $La_2O_3–B_2O_3–ZnO$ additive, *Appl. Phys. A: Mater. Sci. Process.*, 2018, **124**, 188.
20 K. Ezaki, Y. Baba, H. Takahashi, K. Shibata and S. Nakano, Microwave Dielectric Properties of CaO-Li_2O-Ln_2O_3-TiO_2 Ceramics, *Jpn. J. Appl. Phys.*, 1993, **32**, 4319–4322.
21 H. Takahashi, Y. Baba, K. Ezaki and K. Shibata, Microwave Dielectric Properties and Crystal Structure of $CaO–Li_2O–(1-x)Sm_2O_3–x,Ln_2O_3–TiO_2$ (Ln: lanthanide) Ceramics System, *Jpn. J. Appl. Phys.*, 1996, **35**, 5069–5073.
22 R. J. Cava, Dielectric materials for applications in microwave communications, *J. Mater. Chem.*, 2001, **11**, 54–62.

23 T. A. Vanderah, Talking Ceramics, *Science*, 2002, **298**, 1182–1184.
24 H. Yang, E. Li, H. Yang, H. He and R. S. Zhang, Synthesis of $Zn_{0.5}Ti_{0.5}NbO_4$ microwave dielectric ceramics with Li_2O-B_2O_3-SiO_2 glass for LTCC application, *Int. J. Appl. Glass Sci.*, 2018, **9**, 392–402.
25 H. Wu and J. Bi, Synthesis, characterization, and microwave dielectric properties of monoclinal structure $ZnZrNb_2O_8$ ceramics through the aqueous sol–gel process, *J. Mater. Sci.: Mater. Electron.*, 2016, **27**, 3474–3480.
26 C. H. Wang, X. P. Jing, L. Wang and J. Lu, XRD and Raman Studies on the Ordering/Disordering of Ba$(Mg_{1/3}Ta_{2/3})O_3$, *J. Am. Ceram. Soc.*, 2009, **92**, 1547–1551.
27 C. F. Tseng, Microwave dielectric properties of low loss microwave dielectric ceramics: $A_{0.5}Ti_{0.5}NbO_4$ (A=Zn, Co), *J. Eur. Ceram. Soc.*, 2014, **34**, 3641–3648.
28 K. Kanehara, T. Hoshina, H. Takeda and T. Tsurumi, Terahertz permittivity of rutile TiO_2 single crystal measured by anisotropic far-infrared ellipsometry, *J. Ceram. Soc. Jpn.*, 2015, **123**, P5-1–P5-3.
29 Y. Liao, S. Takezawa, H. Takeda, T. Tsurumi and T. Hoshina, Terahertz dielectric response of nano-grained barium titanate ceramics measured by far-infrared spectroscopic ellipsometry, *Jpn. J. Appl. Phys.*, 2019, **58**, SLLA07.
30 J. Guo, D. Zhou, Y. Li, T. Shao, Z. M. Qi, B. B. Jin and H. Wang, Structure–property relationships of novel microwave dielectric ceramics with low sintering temperatures: $(Na_{0.5x},Bi_{0.5x}Ca_{1-x})MoO_4$, *Dalton Trans.*, 2014, **43**, 11888–11896.
31 K. Kanehara, T. Hoshina, H. Takeda and T. Tsurumi, Hoshina, Takuya-Measurement of ionic polarization of $SrTiO_3$ single crystal by far-infrared spectroscopic ellipsometry, *Appl. Phys. Lett.*, 2014, **105**, 042901.
32 R. D. Shannon, Dielectric polarizabilities of ions in oxides and fluorides, *J. Appl. Phys.*, 1993, **73**, 348–366.
33 D. Zhou, X. Q. Fan, X. W. Jin, D. W. He and G. H. Chen, Structures, Phase Transformations, and Dielectric Properties of $BiTaO_4$ Ceramics, *Inorg. Chem.*, 2016, **55**, 11979–11986.
34 M. M. Mao, X. Q. Liu and X. M. Chen, Structural Evolution and Its Effects on Dielectric Loss in $Sr_{1+x,}Sm_{1-x}Al_{1-x}Ti_xO_4$ Microwave Dielectric Ceramics, *J. Am. Ceram. Soc.*, 2011, **94**, 2506–2511.
35 N. E. Brese and M. O'Keeffe, Bond-valence parameters for solids, *Acta Crystallogr., Sect. B: Struct. Sci.*, 1991, **47**, 192–197.
36 X. C. Fan, X. M. Chen and X. Q. Liu, Structural Dependence of Microwave Dielectric Properties of $SrRAlO_4$ (R=Sm, Nd, La) Ceramics: Crystal Structure Refinement and Infrared Reflectivity Study, *Chem. Mater.*, 2008, **20**, 4092.
37 A. Magrez, M. Cochet, O. Joubert, G. Louarn, A. M. Ganne and O. Chauvet, High Internal Stresses in $Sr_{1-x}La_{1+x}Al_{1-x}Mg_xO_4$ Solid Solution ($0 \leq x \leq 0.7$) Characterized by Infrared and Raman Spectroscopies Coupled with Crystal Structure Refinement, *Chem. Mater.*, 2001, **13**, 3893–3898.
38 J. C. Phillips, Dielectric Definition of Electronegativity, *Phys. Rev. Lett.*, 1968, **20**, 550–553.
39 J. A. Van Vechten, Quantum Dielectric Theory of Electronegativity in Covalent Systems. I. Electronic Dielectric Constant, *Phys. Rev.*, 1969, **182**, 891–905.
40 J. A. Van Vechten, Quantum Dielectric Theory of Electronegativity in Covalent Systems. II. Ionization Potentials and Interband Transition Energies, *Phys. Rev.*, 1969, **187**, 1007–1020.
41 J. C. Phillips, Ionicity of the Chemical Bond in Crystals, *Rev. Mod. Phys.*, 1970, **42**, 317–356.
42 B. F. Levine, Bond susceptibilities and ionicities in complex crystal structures, *J. Chem. Phys.*, 1973, **59**, 1463–1486.
43 J. C. Phillips, Bonds and Bands in Semiconductors, *Science*, 1970, **169**, 1035.
44 W. Kucharczyk, A bond-charge calculation of the quadratic electro-optic effect in LiF, *J. Phys. C: Solid State Phys.*, 1987, **20**, 1875–1880.
45 B. F. Levine, Bond-Charge Calculation of Nonlinear Optical Susceptibilities for Various Crystal Structures, *Phys. Rev. B: Solid State*, 1973, **8**, 4046–4046.
46 J. C. Phillips and J. A. Van Vechten, Charge Redistribution and Piezoelectric Constants, *Phys. Rev. Lett.*, 1969, **23**, 1115–1117.
47 R. M. Martin, Elastic Properties of ZnS Structure Semiconductors, *Phys. Rev. B: Solid State*, 1970, **1**, 4005–4011.
48 J. A. Van Vechten and T. K. Bergstresser, Electronic Structures of Semiconductor Alloys, *Phys. Rev. B: Solid State*, 1970, **1**, 3351–3358.
49 G. B. Stringfellow, Calculation of ternary phase diagrams of III–V systems, *J. Phys. Chem. Solids*, 1972, **33**, 665–677.
50 J. C. Phillips and J. A. Van Vechten, Spectroscopic Analysis of Cohesive Energies and Heats of Formation of Tetrahedrally Coordinated Semiconductors, *Phys. Rev. B: Solid State*, 1970, **2**, 2147–2160.
51 B. F. Levine, Electrodynamical Bond-Charge Calculation of Nonlinear Optical Susceptibilities, *Phys. Rev. Lett.*, 1969, **22**, 787–790.
52 J. C. Phillips and J. A. Van Vechten, Nonlinear Optical Susceptibilities of Covalent Crystals, *Phys. Rev.*, 1969, **183**, 709–711.
53 B. F. Levine, A New Contribution to the Nonlinear Optical Susceptibility Arising from Unequal Atomic Radii, *Phys. Rev. Lett.*, 1970, **25**, 440–443.
54 P. Lawaetz, Effective Charges and Ionicity, *Phys. Rev. Lett.*, 1971, **26**, 697–700.
55 P. Lawaetz, Valence-Band Parameters in Cubic Semiconductors, *Phys. Rev. B: Solid State*, 1971, **4**, 3460–3467.
56 C. V. de Alvarez, J. P. Walter, M. L. Cohen, J. Stokes and Y. R. Shen, Wavelength-Modulation Spectra and Band Structures of InP and GaP, *Phys. Rev. B: Solid State*, 1972, **6**, 1412–1419.

57 A. Baldereschi and J. J. Hopfield, Binding to Isoelectronic Impurities in Semiconductors, *Phys. Rev. Lett.*, 1972, **28**, 171–174.
58 D. K. Biegelsen, Frequency dependence of the photoelastic coefficients of silicon, *Phys. Rev. B: Solid State*, 1975, **12**, 2427–2431.
59 D. K. Biegelsen, Photoelastic Tensor of Silicon and the Volume Dependence of the Average Gap, *Phys. Rev. Lett.*, 1974, **32**, 1196–1199.
60 W. Kucharczyk, The anisotropy of the cubic susceptibility in alkali halides as related to electro-optic and elasto-optic phenomena, *J. Phys. C: Solid State Phys.*, 1988, **21**, L985–L988.
61 X. Dongfeng and S. Zhang, Calculation of the nonlinear optical coefficient of the $NdAl_3(BO_3)_4$ crystal, *J. Phys.: Condens. Matter*, 1996, **8**, 1949–1956.
62 Z. J. Wu, Q. B. Meng and S. Y. Zhang, Semiempirical study on the valences of Cu and bond covalency in $Y_{1-x}Ca_xBa_2Cu_3O_{6+y}$, *Phys. Rev. B: Condens. Matter Mater. Phys.*, 1998, **58**, 958–962.
63 F. Gao, D. Li, J. He, Y. Tian, D. Yu and S. Zhang, Chemical bond properties and Mössbauer spectroscopy in $REBa_2Cu_3O_7$ (RE=Eu, Y), *Phys. C*, 2002, **371**, 151–155.
64 Q. B. Meng, Z. J. Wu and S. Y. Zhang, The bond ionicity in (R=Pr, Sm, Eu, Gd, Dy, Y, Ho, Er, Tm), *J. Phys.: Condens. Matter*, 1998, **10**, L85–L88.
65 Z. J. Wu, S. Y. Zhang and H. J. Zhang, Relationship between chemical bond parameters and superconducting temperature in $HgBa_2Ca_{n-1}Cu_nO_{2n+2+\delta}$ (n=1, 2, 3, 4), *J. Phys. Chem. Solids*, 2002, **63**, 193–196.
66 F. M. Gao, D. C. Li and S. Y. Zhang, M ssbauer spectroscopy and chemical bonds in $BaFe_{12}O_{19}$ hexaferrite, *J. Phys.: Condens. Matter*, 2003, **15**, 5079–5084.
67 H. Li, S. Zhou, S. Zhang and X. Cao, Calculation of the thermal expansion coefficient for $Bi_2Sr_2CaCu_2O_8$, *Phys. C*, 2006, **449**, 41–46.
68 D. Liu, S. Zhang and Z. Wu, Lattice energy estimation for inorganic ionic crystals, *Inorg. Chem.*, 2003, **42**, 2465–2469.
69 D. R. Penn, Wave-Number-Dependent Dielectric Function of Semiconductors, *Phys. Rev.*, 1962, **128**, 2093–2097.
70 S. W. Wu, G. Wang, Q. Wang, Y. D. Jia, J. Yi, Q. J. Zhai, J. B. Liu, B. A. Sun, H. J. Chu, J. Shen, P. K. Liaw, C. T. Liu and T. Y. Zhang, Enhancement of strength-ductility trade-off in a high-entropy alloy through a heterogeneous structure, *Acta Mater.*, 2019, **165**, 444–458.
71 D. Zhou, D. Guo, W.-B. Li, L.-X. Pang, X. Yao, D.-W. Wang and I. M. Reaney, Novel temperature stable high-er microwave dielectrics in the Bi_2O_3-TiO_2-V_2O_5 system, *J. Mater. Chem. C*, 2016, **4**, 5357–5362.
72 H. Yang, S. Zhang, Y. Chen, H. Yang, Z. Fang, Y. Yuan and E. Li, Low-firing, temperature stable and improved microwave dielectric properties of ZnO-TiO_2-Nb_2O_5 composite ceramics, *J. Materiomics*, 2019, **5**, 471–479.
73 C. L. Diao, C. H. Wang, N. N. Luo, Z. M. Qi, T. Shao, Y. Y. Wang, J. Lu, Q. C. Wang, X. J. Kuang, L. Fang, F. Shi and X. P. Jing, First-principle calculation and assignment for vibrational spectra of $Ba(Mg_{1/3}Nb_{2/3})O_3$ microwave dielectric ceramic, *J. Appl. Phys.*, 2014, **115**, 114103.
74 J. S. Shi and S. Y. Zhang, Barycenter of Energy of Lanthanide 4fN-15d Configuration in Inorganic Crystals, *J. Phys. Chem. B*, 2004, **108**, 18845–18849.
75 D. Xue and S. Zhang, Chemical Bond Analysis of Nonlinearity of Urea Crystal, *J. Phys. Chem. A*, 1997, **101**, 5547–5550.
76 T. Tsunooka, M. Androu, Y. Higashida, H. Sugiura and H. Ohsato, Effects of TiO_2 on sinterability and dielectric properties of high-Q forsterite ceramics, *J. Eur. Ceram. Soc.*, 2003, **23**, 2573–2578.
77 N. M. Alford and S. J. Penn, Sintered alumina with low dielectric loss, *J. Appl. Phys.*, 1996, **80**, 5895–5898.
78 K. P. Surendran, P. V. Bijumon, P. Mohanan and M. T. Sebastian, (1-*x*)$MgAl_2O_4$-*x*TiO_2 dielectrics for microwave and millimeter wave applications, *Appl. Phys. A: Mater. Sci. Process.*, 2005, **81**, 823–826.
79 A. Kan, H. Ogawa and A. Yokoi, Sintering temperature dependence of microwave dielectric properties in $Mg_4(TaNb_{1-x}V_x)O_9$ compounds, *Mater. Res. Bull.*, 2006, **41**, 1178–1184.
80 S. H. Yoon, D. W. Kim, S. Y. Cho and K. S. Hong, Investigation of the relations between structure and microwave dielectric properties of divalent metal tungstate compounds, *J. Eur. Ceram. Soc.*, 2006, **26**, 2051–2054.
81 A. Belous, O. Ovchar, D. Durylin, M. Valant, M. Macek-Krzmanc and D. Suvorov, Microwave composite dielectrics based on magnesium titanates, *J. Eur. Ceram. Soc.*, 2007, **27**, 2963–2966.
82 D. W. Kim, D. K. Kwon, S. H. Yoon and K. S. Hong, Microwave Dielectric Properties of Rare-Earth Ortho-Niobates with Ferroelasticity, *J. Am. Ceram. Soc.*, 2006, **89**, 3861–3864.
83 C. L. Huang and M. H. Weng, Improved high q value of $MgTiO_3$-$CaTiO_3$ microwave dielectric ceramics at low sintering temperature, *Mater. Res. Bull.*, 2001, **36**, 2741–2750.
84 H. T. Kim, S. Nahm, J. D. Byun and Y. Kim, Low-Fired (Zn, Mg)TiO_3 Microwave Dielectrics, *J. Am. Ceram. Soc.*, 1999, **82**, 3476–3480.
85 S. Nomura, Ceramics for microwave dielectric resonator, *Ferroelectrics*, 1983, **49**, 61–70.
86 T. Shimada, K. Kura and S. Ohtsuki, Dielectric properties and far infrared reflectivity of lanthanum aluminate–strontium titanate ceramics, *J. Eur. Ceram. Soc.*, 2006, **26**, 2017–2021.
87 J. Zhang, Y. Luo, Z. Yue and L. Li, High-Q and temperature-stable microwave dielectrics in layer cofired $Zn_{1.01}Nb_2O_6/TiO_2/Zn_{1.01}Nb_2O_6$ ceramic architectures, *J. Am. Ceram. Soc.*, 2019, **102**, 342–350.
88 M. P. Seabra, A. N. Salak, V. M. Ferreira, J. L. Ribeiro and L. G. Vieira, Dielectric properties of (1−*x*)$La(Mg_{1/2}Ti_{1/2})O_3$–*x*$SrTiO_3$ ceramics, *J. Eur. Ceram. Soc.*, 2004, **24**, 2995–3002.
89 D. W. Kim, J. H. Kim, J. R. Kim and K. S. Hong, Phase Constitutions and Microwave Dielectric Properties of $Zn_3Nb_2O_8$–TiO_2, *Jpn. J. Appl. Phys.*, 2001, **40**, 5994–5998.

90 D. J. Kim, J. W. Hahn, G. P. Han, S. S. Lee and T. G. Choy, Effects of Alkaline-Earth-Metal Addition on the Sinterability and Microwave Characteristics of (Zr,Sn)TiO_4 Dielectrics, *J. Am. Ceram. Soc.*, 2000, **83**, 1010–1012.

91 I. N. Jawahar, P. Mohanan and M. T. Sebastian, $A_5B_4O_{15}$ (A=Ba, Sr, Mg, Ca, Zn; B=Nb, Ta) microwave dielectric ceramics, *Mater. Lett.*, 2003, **57**, 4043–4048.

92 Y. Tohdo, K. Kakimoto, H. Ohsato, H. Yamada and T. Okawa, Microwave dielectric properties and crystal structure of homologous compounds $ALa_4Ti_4O_{15}$ (A=Ba, Sr and Ca) for base station applications, *J. Eur. Ceram. Soc.*, 2006, **26**, 2039–2043.

93 P. RiaziKhoei, F. Azough and R. Freer, The Influence of $ZnNb_2O_6$ on the Microwave Dielectric Properties of $ZrTi_2O_6$ Ceramics, *J. Am. Ceram. Soc.*, 2006, **89**, 216–223.

94 A. Borisevich and P. K. Davies, Microwave dielectric properties of $Li_{1+x-y}M_{1-x-3y}Ti_{x+4y}O_3$ ($M=Nb^{5+}$, Ta^{5+}) solid solutions, *J. Eur. Ceram. Soc.*, 2001, **21**, 1719–1722.

95 K. Fukuda, I. Fujii, R. Kitoh, Y. Cho and I. Awai, Influence of Rare Earth Ions on BaO-TiO_2-Rare Earth Oxide Ceramics for Microwave Applications, *Jpn. J. Appl. Phys.*, 1993, **32**, 1712–1715.

96 M. Heuer, A. L. Huber, G. D. Bromiley, K. T. Fehr and K. Bente, Characterization of synthetic hedenbergite ($CaFeSi_2O_6$)–petedunnite ($CaZnSi_2O_6$) solid solution series by X-ray single crystal diffraction, *Phys. Chem. Miner.*, 2005, **32**, 552–563.

97 G. J. Redhammer and G. Roth, A comparison of the clinopyroxene compounds $CaZnSi_2O_6$ and $CaZnGe_2O_6$, *Acta Crystallogr., Sect. C: Cryst. Struct. Commun.*, 2005, **61**, i20–i22.

98 G. J. Redhammer, G. Roth, W. Treutmann, W. Paulus, G. André, C. Pietzonka and G. Amthauer, Magnetic ordering and spin structure in Ca-bearing clinopyroxenes $CaM^{2+}(Si, Ge)_2O_6$, M=Fe, Ni, Co, Mn, *J. Solid State Chem.*, 2008, **181**, 3163–3176.

99 A. L. Huber, S. Heuss-Aßbichler, K. T. Fehr and G. D. Bromiley, Petedunnite ($CaZnSi_2O_6$): Stability and phase relations in the system CaO-ZnO-SiO_2, *Am. Mineral.*, 2012, **97**, 739–749.

100 M. Xiao, Y. Wei and P. Zhang, The effect of sintering temperature on the crystal structure and microwave dielectric properties of $CaCoSi_2O_6$ ceramic, *Mater. Chem. Phys.*, 2019, **225**, 99–104.

101 H. Sun, Q. Zhang, H. Yang and J. Zou, $(Ca_{1-x}Mg_x)SiO_3$: A low-permittivity microwave dielectric ceramic system, *Mater. Sci. Eng., B*, 2007, **138**, 46–50.

102 H. Li, X. Chen, Q. Xiang, B. Tang, J. Lu, Y. Zou and S. Zhang, Structure, bond characteristics and Raman spectra of $CaMg_{1-x}Mn_xSi_2O_6$ microwave dielectric ceramics, *Ceram. Int.*, 2019, **45**, 14160–14166.

103 J. Zhang, Y. Zhou and Z. Yue, Low-temperature sintering and microwave dielectric properties of LiF-doped $CaMg_{1-x}Zn_xSi_2O_6$ ceramics, *Ceram. Int.*, 2013, **39**, 2051–2058.

104 Y. Lai, H. Su, G. Wang, X. Tang, X. Liang, X. Huang, Y. Li, H. Zhang, C. Ye and X. R. Wang, Improved microwave dielectric properties of $CaMgSi_2O_6$ ceramics through CuO doping, *J. Alloys Compd.*, 2019, **772**, 40–48.

105 H. Li, C. Cai, Q. Xiang, B. Tang, S. Yu, J. Xiao, H. Luo and S. Zhang, , Raman, complex chemical bond and structural studies of novel $CaMg_{1-x}(Mn_{1/2}Zn_{1/2})_xSi_2O_6$ (x=0-0.1) ceramics, *Ceram. Int.*, 2019, **45**, 23157–23163.

106 T. Joseph, M. T. Sebastian, H. Sreemoolanadhan and V. K. Sree Nageswari, Effect of Glass Addition on the Microwave Dielectric Properties of $CaMgSi_2O_6$ Ceramics, *Int. J. Appl. Ceram. Technol.*, 2010, **7**, E98–E106.

107 R. M. Thompson and R. T. Downs, The crystal structure of diopside at pressure to 10 GPa, *Am. Mineral.*, 2008, **93**, 177–186.

108 H. Ohsato, T. Tsunooka, T. Sugiyama, K.-I. Kakimoto and H. Ogawa, Forsterite ceramics for millimeterwave dielectrics, *J. Electroceram.*, 2006, **17**, 445–450.

109 T. Joseph and M. T. Sebastian, Microwave Dielectric Properties of $(Sr_{1-x}A_x)_2(Zn_{1-x}B_x)Si_2O_7$ Ceramics (A=Ca, Ba and B=Co, Mg, Mn, Ni), *J. Am. Ceram. Soc.*, 2010, **93**, 147–154.

110 M. Xiao, Y. Wei, H. Sun, J. Lou and P. Zhang, Crystal structure and microwave dielectric properties of low-permittivity $Sr_2MgSi_2O_7$ ceramic, *J. Mater. Sci.: Mater. Electron.*, 2018, **29**, 20339–20346.

111 T. Endo, Y. Doi, M. Wakeshima and Y. Hinatsu, Crystal Structures and Magnetic Properties of New Europium Melilites $Eu_2MSi_2O_7$ (M=Mg, Mn) and Their Strontium Analogues, *Inorg. Chem.*, 2010, **49**, 10809–10814.

112 B. E. Warren and O. R. Trautz, The structure of hardystonite $Ca_2ZnSi_2O_7$, *Z. Kristallogr.*, 1930, **75**, 525–528.

113 M. Xiao, Y. Wei and P. Zhang, The Correlations between Complex Chemical Bond Theory and Microwave Dielectric Properties of $Ca_2MgSi_2O_7$ Ceramics, *J. Electron. Mater.*, 2019, **48**, 1652–1659.

114 J. Hanuza, M. Ptak, M. Mączka, K. Hermanowicz, J. Lorenc and A. A. Kaminskii, Polarized IR and Raman spectra of $Ca_2MgSi_2O_7$, $Ca_2ZnSi_2O_7$ and $Sr_2MgSi_2O_7$ single crystals: Temperature-dependent studies of commensurate to incommensurate and incommensurate to normal phase transitions, *J. Solid State Chem.*, 2012, **191**, 90–101.

115 X. Q. Song, W. Lei, M. Q. Xie, J. Li, X. C. Wang and W. Z. Lu, Sintering behaviour, lattice energy and microwave dielectric properties of melilite-type $BaCo2Si_2O_7$ ceramics, *Mater. Res. Express*, 2020, **6**, 126322.

116 J. W. Kaiser and W. Jeitschko, Crystal structure of the new barium zinc silicate $Ba_2ZnSi_2O_7$, *Z. Kristallogr. - New Cryst. Struct.*, 2002, **217**, 25–26.

117 R. Shannon, Revised effective ionic radii and systematic studies of interatomic distances in halides and chalcogenides, *Acta Crystallogr., Sect. A: Cryst. Phys., Diffr., Theor. Gen. Crystallogr.*, 1976, **32**, 751–767.

118 H. Zhou, X. Tan, J. Huang, N. Wang, G. Fan and X. Chen, Phase structure, sintering behavior and adjustable microwave dielectric properties of $Mg_{1-x}Li_{2x}Ti_xO_{1+2x}$ solid solution ceramics, *J. Alloys Compd.*, 2017, **696**, 1255–1259.

119 H. Zhou, X. Tan, J. Huang and X. Chen, Sintering behavior, phase evolution and microwave dielectric properties of thermally stable Li_2O-3MgO-mTiO_2 ceramics ($1 \leq m \leq 6$), *Ceram. Int.*, 2017, **43**, 3688–3692.

120 J. X. Bi, C. C. Li, Y. H. Zhang, C. F. Xing, C. H. Yang and H. T. Wu, Crystal structure, infrared spectra and microwave dielectric properties of ultra low-loss $Li_2Mg_4TiO_7$ ceramics, *Mater. Lett.*, 2017, **196**, 128–131.

121 P. Zhang, M. Yang and M. Xiao, Sintering behavior, crystalline structure and microwave dielectric properties of $Li_2(Ni_{1-x}Mg_x)_3TiO_6$ ($0 \leq x \leq 1$) ceramics, *Ceram. Int.*, 2018, **44**, 21607–21612.

122 J. Bi, Y. Niu and H. Wu, $Li_4Mg_3Ti_2O_9$: A novel low-loss microwave dielectric ceramic for LTCC applications, *Ceram. Int.*, 2017, **43**, 7522–7530.

123 H. L. Pan, C. F. Xing, X. S. Jiang and H. T. Wu, Characterization on low loss dielectric Li_2MgTiO_4 ceramics based on chemical bond theory at microwave frequency, *J. Alloys Compd.*, 2016, **688**, 416–421.

124 Z. Fu, P. Liu, J. Ma, X. Zhao and H. Zhang, Novel series of ultra-low loss microwave dielectric ceramics: $Li_2Mg_3BO_6$ (B=Ti, Sn, Zr), *J. Eur. Ceram. Soc.*, 2016, **36**, 625–629.

125 Z. Fang, B. Tang, F. Si, E. Li, H. Yang and S. Zhang, Phase evolution, structure and microwave dielectric properties of Li_{2+x},Mg_3SnO_6 (x=0.00–0.12) ceramics, *Ceram. Int.*, 2017, **43**, 13645–13652.

126 H. Wu and E. S. Kim, Correlations between crystal structure and dielectric properties of high-Q materials in rock-salt structure Li_2O–MgO–BO_2 (B=Ti, Sn, Zr) systems at microwave frequency, *RSC Adv.*, 2016, **6**, 47443–47453.

127 J. Song, J. Zhang and R. Zuo, Ultrahigh Q values and atmosphere-controlled sintering of $Li_{2(1+x)}Mg_3ZrO_6$ microwave dielectric ceramics, *Ceram. Int.*, 2017, **43**, 2246–2251.

128 Z. Fang, B. Tang, Y. Yuan, X. Zhang and S. Zhang, Structure and microwave dielectric properties of the $Li_{2/3(1-x)}Sn_{1/3(1-x)}Mg_xO$ systems (x=0-4/7), *J. Am. Ceram. Soc.*, 2018, **101**, 252–264.

129 H. L. Pan, L. Cheng and H. T. Wu, Relationships between crystal structure and microwave dielectric properties of $Li_2(Mg_{1-x}Co_x)_3TiO_6$ ($0 \leq x \leq 0.4$) ceramics, *Ceram. Int.*, 2017, **43**, 15018–15026.

130 X. Shi, H. Zhang, D. Zhang, F. Xu, Y. Zheng, G. Wang, C. Liu, L. Jin, J. Li and L. Jia, Correlation between structure characteristics and dielectric properties of $Li_2Mg_{3-x}Cu_xTiO_6$ ceramics based on complex chemical bond theory, *Ceram. Int.*, 2019, **45**, 23509–23514.

131 E. S. Kim, B. S. Chun, R. Freer and R. J. Cernik, Effects of packing fraction and bond valence on microwave dielectric properties of $A^{2+}B^{6+}O_4$ (A^{2+}: Ca, Pb, Ba; B^{6+}: Mo, W) ceramics, *J. Eur. Ceram. Soc.*, 2010, **30**, 1731–1736.

132 C. H. Yang, H. L. Pan, Y. K. Yang and H. T. Wu, Influence of Zn substitution on the crystal structures and microwave dielectric properties of $Li_2(Mg_{1-x}Zn_x)_3TiO_6$ ($0 \leq x \leq 0.2$) ceramics, *J. Alloys Compd.*, 2018, **764**, 424–430.

133 Z. Fang, B. Tang, F. Si and S. Zhang, Temperature stable and high-Q microwave dielectric ceramics in the $Li_2Mg_{3-x}Ca_xTiO_6$ system (x=0.00–0.18), *Ceram. Int.*, 2017, **43**, 1682–1687.

134 X. Shi, H. Zhang, D. Zhang, C. Liu, L. Shi and X. Wang, Structural characteristics and dielectric properties of Ti^{4+}-substituted $Li_2Mg_3SnO_6$ ceramics, *Ceram. Int.*, 2020, **46**, 16038–16046.

135 C. H. Yang, H. L. Pan, Y. K. Yang and H. T. Wu, Effects of Ti-substitution on the crystal structures, micro-structures and microwave dielectric properties of $Li_2Mg_3Zr_{1-x}Ti_xO_6$ ($0 \leq x \leq 1$) ceramics, *Ceram. Int.*, 2018, **44**, 5155–5162.

136 H. L. Pan, Y. X. Mao, Y. K. Yang, Y. W. Zhang and H. T. Wu, Crystal structure, Raman spectra, infrared spectra and microwave dielectric properties of $Li_2Mg_3Ti_{1-x}(Mg_{1/3}Ta_{2/3})_xO_6$ ($0 \leq x \leq 0.2$) solid solution ceramics, *Mater. Res. Bull.*, 2018, **105**, 296–305.

137 H. L. Pan, Y. W. Zhang and H. T. Wu, Crystal structure, infrared spectroscopy and microwave dielectric properties of ultra low-loss $Li_2Mg_3Ti_{0.95}(Mg_{1/3}Sb_{2/3})_{0.05}O_6$ ceramic, *Ceram. Int.*, 2018, **44**, 3464–3468.

138 Y. K. Yang, H. L. Pan and H. T. Wu, Crystal structure, Raman spectra and microwave dielectric properties of $Li_2Mg_3Ti_{1-x}(Mg_{1/3}Nb_{2/3})_xO_6$ ($0 \leq x \leq 0.25$) ceramics, *Ceram. Int.*, 2018, **44**, 11350–11356.

139 H. Xiang, C. Li, C. Yin, Y. Tang and L. Fang, A reduced sintering temperature and improvement in the microwave dielectric properties of $Li_2Mg_3TiO_6$ through Ge substitution, *Ceram. Int.*, 2018, **44**, 5817–5821.

140 H. Wu and E. S. Kim, Characterization of low loss microwave dielectric materials $Li_3Mg_2NbO_6$ based on the chemical bond theory, *J. Alloys Compd.*, 2016, **669**, 134–140.

141 S. S. Batsanov, Dielectric methods of studying the chemical bond and the concept of electronegativity, *Russ. Chem. Rev.*, 1982, **51**, 684–697.

142 P. Zhang, K. Sun, X. Mao, M. Xiao and Z. Zheng, Crystal structures and high microwave dielectric properties in Li^+/Ti^{4+} ions co-doped $Li_3Mg_2NbO_6$ ceramics, *Ceram. Int.*, 2020, **46**, 8097–8103.

143 P. Zhang, L. Liu, M. Xiao and Y. Zhao, A novel temperature stable and high Q microwave dielectric ceramic in $Li_3(Mg_{1-x}Mn_x)_2NbO_6$ system, *J. Mater. Sci.: Mater. Electron.*, 2017, **28**, 12220–12225.

144 P. Zhang, K. Sun, L. Liu and M. Xiao, A novel low loss and low temperature sintering $Li_3(Mg_{1-x}Ca_x)_2NbO_6$ microwave dielectric ceramics by doping LiF additives, *J. Alloys Compd.*, 2018, **765**, 1209–1217.

145 T. Zhang and R. Zuo, Effect of Li_2O–V_2O_5 addition on the sintering behavior and microwave dielectric properties of $Li_3(Mg_{1-x}Zn_x)_2NbO_6$ ceramics, *Ceram. Int.*, 2014, **40**, 15677–15684.

146 H. L. Pan, Y. X. Mao, L. Cheng and H. T. Wu, New $Li_3Ni_2NbO_6$ microwave dielectric ceramics with the orthorhombic structure for LTCC applications, *J. Alloys Compd.*, 2017, **723**, 667–674.

147 C. F. Xing, J. X. Bi and H. T. Wu, Effect of Co-substitution on microwave dielectric properties of $Li_3(Mg_{1-x}Co_x)_2NbO_6$

($0.00 \leq x \leq 0.10$) ceramics, *J. Alloys Compd.*, 2017, **719**, 58–62.

148 X. Zhang, B. Tang, Z. Fang, H. Yang, Z. Xiong, L. Xue and S. Zhang, Structural evolution and microwave dielectric properties of a novel $Li_3Mg_{2-x/3}Nb_{1-2x/3}Ti_xO_6$ system with a rock salt structure, *Inorg. Chem. Front.*, 2018, **5**, 3113–3125.

149 G. Wang, H. Zhang, X. Huang, F. Xu, G. Gan, Y. Yang, D. Wen, J. Li, C. Liu and L. Jin, Correlations between the structural characteristics and enhanced microwave dielectric properties of V–modified $Li_3Mg_2NbO_6$ ceramics, *Ceram. Int.*, 2018, **44**, 19295–19300.

150 P. Zhang, S. Wu and M. Xiao, Effect of Sb^{5+} ion substitution for Nb^{5+} on crystal structure and microwave dielectric properties for $Li_3Mg_2NbO_6$ ceramics, *J. Alloys Compd.*, 2018, **766**, 498–505.

151 C. Pei, C. Hou, Y. Li, G. Yao, Z. Ren, P. Liu and H. Zhang, A low εr and temperature-stable $Li_3Mg_2SbO_6$ microwave dielectric ceramics, *J. Alloys Compd.*, 2019, **792**, 46–49.

152 G. Wang, D. Zhang, X. Huang, Y. Rao, Y. Yang, G. Gan, Y. Lai, F. Xu, J. Li, Y. Liao, C. Liu, L. Jin, V. G. Harris and H. Zhang, Crystal structure and enhanced microwave dielectric properties of Ta^{5+} substituted $Li_3Mg_2NbO_6$ ceramics, *J. Am. Ceram. Soc.*, 2020, **103**, 214–223.

153 P. Zhang, M. Hao, X. Mao, K. Sun and M. Xiao, Effects of W^{6+} substitution on crystal structure and microwave dielectric properties of $Li_3Mg_2NbO_6$ ceramics, *Ceram. Int.*, 2020, **46**, 21336–21342.

154 G. Wang, D. Zhang, J. Li, G. Gan, Y. Rao, X. Huang, Y. Yang, L. Shi, Y. Liao, C. Liu, L. Jin and H. Zhang, Crystal structure, bond energy, Raman spectra, and microwave dielectric properties of Ti-doped $Li_3Mg_2NbO_6$ ceramics, *J. Am. Ceram. Soc.*, 2020, **103**, 4321–4332.

155 H. Li, P. Zhang, X. Chen, B. Tang, S. Yu, J. Lu and S. Zhang, Effect of Zn^{2+} substitution for Mg^{2+} in $Li_3Mg_2SbO_6$ and the impact on the bond characteristics and microwave dielectric properties, *J. Alloys Compd.*, 2020, **832**, 155043.

156 P. Rodríguez-Hernández, J. López-Solano, S. Radescu, A. Mujica, A. Muñoz, D. Errandonea, J. Pellicer-Porres, A. Segura, C. Ferrer-Roca, F. J. Manjón, R. S. Kumar, O. Tschauner and G. Aquilanti, Theoretical and experimental study of $CaWO_4$ and $SrWO_4$ under pressure, *J. Phys. Chem. Solids*, 2006, **67**, 2164–2171.

157 Z. X. Shao, Q. R. Zhang, T. Y. Liu and J. Y. Chen, First-principles study on electronic structures and absorption bands of $CaWO_4$ crystals with interstitial oxygen atoms, *Phys. Status Solidi A*, 2007, **204**, 3159–3164.

158 L. Gracia, V. M. Longo, L. S. Cavalcante, A. Beltrán, W. Avansi, M. S. Li, V. R. Mastelaro, J. A. Varela, E. Longo and J. Andrés, Presence of excited electronic state in $CaWO_4$ crystals provoked by a tetrahedral distortion: An experimental and theoretical investigation, *J. Appl. Phys.*, 2011, **110**, 043501.

159 M. Xiao, H. Sun, Z. Zhou and P. Zhang, Bond ionicity, lattice energy, bond energy, and microwave dielectric properties of $Ca_{1-x}Sr_xWO_4$ ceramics, *Ceram. Int.*, 2018, **44**, 20686–20691.

160 M. T. Sebastian, H. Wang and H. Jantunen, Low temperature co-fired ceramics with ultra-low sintering temperature: A review, *Curr. Opin. Solid State Mater. Sci.*, 2016, **20**, 151–170.

161 H. Yang, E. Li, Y. Yang, Y. Shi, H. He and S. Zhang, Co_2O_3 substitution effects on the structure and microwave dielectric properties of low-firing $(Zn_{0.9}Mg_{0.1})TiO_3$ ceramics, *Ceram. Int.*, 2018, **44**, 5010–5016.

162 Y. Chen, E. Li, S. Duan and S. Zhang, Low Temperature Sintering Kinetics and Microwave Dielectric Properties of $BaTi_5O_{11}$ Ceramic, *ACS Sustainable Chem. Eng.*, 2017, **5**, 10606–10613.

163 H. H. Guo, D. Zhou, C. Du, P. J. Wang, W. F. Liu, L. X. Pang, Q. P. Wang, J. Z. Su, C. Singh and S. Trukhanov, Temperature stable $Li_2Ti_{0.75}(Mg_{1/3}Nb_{2/3})_{0.25}O_3$-based microwave dielectric ceramics with low sintering temperature and ultra-low dielectric loss for dielectric resonator antenna applications, *J. Mater. Chem. C*, 2020, **8**, 4690–4700.

164 D. Zhou, J. Li, L. X. Pang, D.-W. Wang and I. M. Reaney, Novel water insoluble $(Na_x,Ag_{2-x})MoO_4$ ($0 \leq x \leq 2$) microwave dielectric ceramics with spinel structure sintered at 410 degrees, *J. Mater. Chem. C*, 2017, **5**, 6086–6091.

165 H. H. Guo, D. Zhou, W. F. Liu, L. X. Pang, D. W. Wang, J. Z. Su and Z. M. Qi, Microwave dielectric properties of temperature-stable zircon-type (Bi, Ce)VO_4 solid solution ceramics, *J. Am. Ceram. Soc.*, 2020, **103**, 423–431.

166 L. X. Pang, W. G. Liu, D. Zhou and Z. X. Yue, Novel glass-free low-temperature fired microwave dielectric ceramics: $Bi(Ga_{1/3}Mo_{2/3})O_4$, *Ceram. Int.*, 2016, **42**, 4574–4577.

167 H. H. Xi, D. Zhou, H. D. Xie, B. He and Q. P. Wang, Raman Spectra, Infrared Spectra, and Microwave Dielectric Properties of Low-Temperature Firing $[(Li_{0.5}Ln_{0.5})_{1-x}Ca_x]MoO_4$ (Ln=Sm and Nd) Solid Solution Ceramics with Scheelite Structure, *J. Am. Ceram. Soc.*, 2015, **98**, 587–593.

168 H. H. Guo, D. Zhou, L. X. Pang and Z. M. Qi, Microwave dielectric properties of low firing temperature stable scheelite structured (Ca,Bi)(Mo,V)O_4 solid solution ceramics for LTCC applications, *J. Eur. Ceram. Soc.*, 2019, **39**, 2365–2373.

169 D. Thomas and M. T. Sebastian, Temperature-Compensated $LiMgPO_4$: A New Glass-Free Low-Temperature Cofired Ceramic, *J. Am. Ceram. Soc.*, 2010, **93**, 3828–3831.

170 P. Zhang, S. Wu and M. Xiao, The microwave dielectric properties and crystal structure of low temperature sintering $LiNiPO_4$ ceramics, *J. Eur. Ceram. Soc.*, 2018, **38**, 4433–4439.

171 X. Hu, Z. Cheng, Y. Li and Z. Ling, Dielectric relaxation and microwave dielectric properties of low temperature sintering $LiMnPO_4$ ceramics, *J. Alloys Compd.*, 2015, **651**, 290–293.

172 I. Abrahams and K. S. Easson, Structure of lithium nickel phosphate, *Acta Crystallogr., Sect. C: Cryst. Struct. Commun.*, 1993, **49**, 925–926.

173 E. C. Xiao, Z. Cao, J. Li, X. H. Li, M. Liu, Z. Yue, Y. Chen, G. Chen, K. Song, H. Zhou and F. Shi, Crystal structure, dielectric properties, and lattice vibrational characteristics of $LiNiPO_4$ ceramics sintered at different temperatures, *J. Am. Ceram. Soc.*, 2020, **103**, 2528–2539.

174 D. Wang, D. Zhou, S. Zhang, Y. Vardaxoglou, W. G. Whittow, D. Cadman and I. M. Reaney, Cold-Sintered Temperature Stable $Na_{0.5}Bi_{0.5}MoO_4$–Li_2MoO_4 Microwave Composite Ceramics, *ACS Sustainable Chem. Eng.*, 2018, **6**, 2438–2444.

175 D. Zhou, L. X. Pang, D. W. Wang, H. H. Guo, F. Yang, Z. M. Qi, C. Li, B. B. Jin and I. M. Reaney, Crystal structure, impedance and broadband dielectric spectra of ordered scheelite-structured $Bi(Sc_{1/3}Mo_{2/3})O_4$ ceramic, *J. Eur. Ceram. Soc.*, 2018, **38**, 1556–1561.

176 L. X. Pang, D. Zhou, Z. M. Qi and Z. X. Yue, Influence of W substitution on crystal structure, phase evolution and microwave dielectric properties of $(Na_{0.5}Bi_{0.5})MoO_4$ ceramics with low sintering temperature, *Sci. Rep.*, 2017, **7**, 3201.

177 D. Zhou, H. Wang, L.-X. Pang, C. A. Randall and X. Yao, Bi_2O_3–MoO_3 Binary System: An Alternative Ultralow Sintering Temperature Microwave Dielectric, *J. Am. Ceram. Soc.*, 2009, **92**, 2242–2246.

178 H. Yang, S. Zhang, H. Yang, Y. Yuan and E. Li, $Gd_2Zr_3(MoO_4)_9$ microwave dielectric ceramics with trigonal structure for LTCC application, *J. Am. Ceram. Soc.*, 2020, **103**, 1131–1139.

179 B. J. Tao, C. F. Xing, W. F. Wang, H. T. Wu and Y. Y. Zhou, A novel $Ce_2Zr_3(MoO_4)_9$ microwave dielectric ceramic with ultra-low firing temperature, *Ceram. Int.*, 2019, **45**, 24675–24683.

180 Y. Zhang and H. Wu, Crystal structure and microwave dielectric properties of $La_2(Zr_{1-x}Ti_x)_3(MoO_4)_9$ $(0 \le x \le 0.1)$ ceramics, *J. Am. Ceram. Soc.*, 2019, **102**, 4092–4102.

181 Y. H. Zhang, J. J. Sun, N. Dai, Z. C. Wu, H. T. Wu and C. H. Yang, Crystal structure, infrared spectra and microwave dielectric properties of novel extra low-temperature fired $Eu_2Zr_3(MoO_4)_9$ ceramics, *J. Eur. Ceram. Soc.*, 2019, **39**, 1127–1131.

182 C. F. Xing, B. Wu, J. Bao, H. T. Wu and Y. Y. Zhou, Crystal structure, infrared spectra and microwave dielectric properties of a novel low-firing $Gd_2Zr_3(MoO_4)_9$ ceramic, *Ceram. Int.*, 2019, **45**, 22207–22214.

183 L. Shi, C. Liu, H. Zhang, R. Peng, G. Wang, X. Shi, X. Wang and W. Wang, Crystal structure, Raman spectroscopy, metal compatibility and microwave dielectric properties of $Ce_2Zr_3(MoO_4)_9$ ceramics, *Mater. Chem. Phys.*, 2020, **250**, 122954.

184 C. Xing, Y. Zhang, B. Tao, H. Wu and Y. Zhou, Crystal structure, infrared spectra and microwave dielectric properties of low-firing $La_2Zr_3(MoO_4)_9$ ceramics prepared by reaction-sintering process, *Ceram. Int.*, 2019, **45**, 22376–22382.

185 H. Tian, X. Liu, Y. Yang, H. Wu and Z. Zhang, Crystal Structure, Infrared Spectra, and Microwave Dielectric Properties of $Ce_2(Zr_{0.94}Sn_{0.06})_3(MoO_4)_9$ Ceramics With Low Sintering Temperature, *Front. Mater.*, 2020, **7**, 145.

186 H. Li, P. Zhang, S. Yu, H. Yang, B. Tang, F. Li and S. Zhang, Structural dependence of microwave dielectric properties of spinel structured $Mg_2(Ti_{1-x}Sn_x)O_4$ solid solutions: Crystal structure refinement, Raman spectra study and complex chemical bond theory, *Ceram. Int.*, 2019, **45**, 11639–11647.

187 H. J. Jo, J. S. Kim and E. S. Kim, Microwave dielectric properties of $MgTiO_3$-based ceramics, *Ceram. Int.*, 2015, **41**, S530–S536.

188 H. Li, R. Xiang, X. Chen, H. Hua, S. Yu, B. Tang, G. Chen and S. Zhang, Intrinsic dielectric behavior of Mg_2TiO_4 spinel ceramic, *Ceram. Int.*, 2020, **46**, 4235–4239.

189 J. Zheng, Y. Yang, H. Wu, Y. Zhou and Z. Zhang, Structure, infrared spectra and microwave dielectric properties of the novel Eu_2TiO_5 ceramics, *J. Am. Ceram. Soc.*, 2020, **103**, 4333–4341.

190 W. G. Mumme and A. D. Wadsley, The structure of orthorhombic Y_2TiO_5, an example of mixed seven- and fivefold coordination, *Acta Crystallogr., Sect. B: Struct. Sci.*, 1968, **24**, 1327–1333.

191 H. Niu, H. Gou, R. C. Ewing and J. Lian, First Principles Investigation of Structural, Elstic and Electronic Properties of Lanthanide Titanate Oxides Ln_2TiO_5, *MRS Online Proc. Libr.*, 2011, **1298**, 85–90.

192 W. I. F. David, The high-temperature paraelastic structure of LaNbO4, *Mater. Res. Bull.*, 1983, **18**, 749–756.

193 K. Hadidi, R. Hancke, T. Norby, A. E. Gunnæs and O. M. Løvvik, Atomistic study of $LaNbO_4$; surface properties and hydrogen adsorption, *Int. J. Hydrogen Energy*, 2012, **37**, 6674–6685.

194 B. Ma, B. Chi, J. Pu and L. Jian, LaNbO4 toughened NiO–Y_2O_3 stabilized ZrO_2 composite for the anode support of planar solid oxide fuel cells, *Int. J. Hydrogen Energy*, 2013, **38**, 4776–4781.

195 G. Canu, V. Buscaglia, C. Ferrara, P. Mustarelli, S. Gonçalves Patrício, A. I. Batista Rondão, C. Tealdi and F. M. B. Marques, Oxygen transport and chemical compatibility with electrode materials in scheelite-type $LaW_xNb_{1-x}O_{4+x/2}$ ceramic electrolyte, *J. Alloys Compd.*, 2017, **697**, 392–400.

196 P. Sarin, R. W. Hughes, D. R. Lowry, Z. D. Apostolov and W. M. Kriven, High-Temperature Properties and Ferroelastic Phase Transitions in Rare-Earth Niobates $(LnNbO_4)$, *J. Am. Ceram. Soc.*, 2014, **97**, 3307–3319.

197 M. Xiao, P. Zhang, J. Lou, Y. Wei and P. Zhang, Combined synthesis methods for producing $LaNbO_4$ ceramics and investigation of microwave dielectric properties based on complex chemical bond theory, *J. Alloys Compd.*, 2020, **812**, 152154.

198 M. Xiao, Q. Gu, Z. Zhou and P. Zhang, Study of the microwave dielectric properties of $(La_{1-x}Sm_x)NbO_4$ (x=0-0.10) ceramics via bond valence and packing fraction, *J. Am. Ceram. Soc.*, 2017, **100**, 3952–3960.

199 P. Zhang, Y. Zhao and L. Li, The correlations among bond ionicity, lattice energy and microwave dielectric properties of $(Nd_{1-x}La_x)NbO_4$ ceramics, *Phys. Chem. Chem. Phys.*, 2015, **17**, 16692–16698.

200 P. Zhang and Y. Zhao, Influence of Sm^{3+} substitutions for Nd^{3+} on the microwave dielectric properties of $(Nd_{1-x}Sm_x)NbO_4$ (x=0.02–0.15) ceramics, *J. Alloys Compd.*, 2016, **654**, 240–245.

201 S. D. Ramarao and V. R. K. Murthy, Structural phase transformation and microwave dielectric studies of $SmNb_{1-x}(Si_{1/2}Mo_{1/2})_xO_4$ compounds with fergusonite structure, *Phys. Chem. Chem. Phys.*, 2015, **17**, 12623–12633.

202 D. Guo, D. Zhou, W. B. Li, L. X. Pang, Y. Z. Dai and Z.-M. Qi, Phase Evolution, Crystal Structure, and Microwave Dielectric Properties of Water-Insoluble (1-x) $LaNbO_4$-$x$$LaVO_4$ ($0 \le x \le 0.9$) Ceramics, *Inorg. Chem.*, 2017, **56**, 9321–9329.

203 M. Xiao, Y. Wei, Q. Gu, Z. Zhou and P. Zhang, Relationships between bond ionicity, lattice energy, bond energy and the microwave dielectric properties of La $(Nb_{1-x}Ta_x)O_4$ (x=0–0.10) ceramics, *J. Alloys Compd.*, 2019, **775**, 168–174.

204 H. Yang, S. Zhang, H. Yang, Y. Yuan and E. Li, Influence of $(Al_{1/3}W_{2/3})^{5+}$ co-substitution for Nb^{5+} in $NdNbO_4$ and the impact on the crystal structure and microwave dielectric properties, *Dalton Trans.*, 2018, **47**, 15808–15815.

205 H. Yang, S. Zhang, H. Yang, Y. Yuan and E. Li, $NdNb_{1-x}(Mg_{1/4}W_{3/4})_xO_4$ ($0.02 \le x \le 0.06$) solid solution characterized by infrared spectrum and complex chemical theory, *J. Alloys Compd.*, 2019, **787**, 358–366.

206 H. Yang, S. Zhang, H. Yang, Y. Yuan and E. Li, Structure stability, bond characteristics and microwave dielectric properties of co-substituted $NdNbO_4$ ceramics, *Ceram. Int.*, 2019, **45**, 3620–3626.

207 P. P. Ma, H. Gu and X. M. Chen, Evaluation of the 1 : 2 ordered structure of $Ba(B'_{1/3}B''_{2/3})O_3$ perovskites along various zone axes using transmission electron microscopy, *J. Mater. Chem. C*, 2015, **3**, 10755–10760.

208 C. H. Wang, X. P. Jing, L. Wang and J. Lu, XRD and Raman studies on the ordering/disordering of Ba $(Mg_{1/3}Ta_{2/3})O_3$, *J. Am. Ceram. Soc.*, 2009, **92**, 1547–1551.

209 C. H. Wang, G. H. Liu, X. P. Jing, G. S. Tian, X. Lu and J. Shao, First-Principle Calculation and Far Infrared Measurement for Infrared-Active Modes of $Ba(Mg_{1/3}Ta_{2/3})O_3$, *J. Am. Ceram. Soc.*, 2010, **93**, 3782–3787.

210 C. L. Diao, C. H. Wang, N. N. Luo, Z. M. Qi, T. Shao, Y. Y. Wang, J. Lu, Q. C. Wang, X. J. Kuang and L. Fang, First-principle calculation and assignment for vibrational spectra of Ba $(Mg_{1/3}Nb_{2/3})O_3$ microwave dielectric ceramic, *J. Appl. Phys.*, 2014, **115**, 114103–114112.

211 C. L. Diao, C. H. Wang, N. N. Luo, Z. M. Qi, T. Shao, Y. Y. Wang, J. Lu, F. Shi and X. P. Jing, First-Principle Calculation and Assignment for Vibrational Spectra of Ba $(Mg_{1/2}W_{1/2})O_3$ Microwave Dielectric Ceramic, *J. Am. Ceram. Soc.*, 2013, **96**, 2898–2905.

212 V. Filip'ev, G. Shatalova and E. Fesenko, Determination of bond lengths in tungstates with Perovskite-type structure, *Kristallografiya*, 1974, **19**, 386–387.

213 H. Yang, S. Zhang, Y. Li, H. Yang, Y. Yuan, T. Wen and E. Li, Investigations of dielectric properties of wolframite $A_{0.5}Zr_{0.5}NbO_4$ ceramics by bond theory and far-infrared spectroscopy, *Ceram. Int.*, 2020, **46**, 3688–3694.

214 M. Xiao, P. Zhang, H. Sun, Z. Zhou and P. Zhang, Influence of Ni^{2+} Substitution for Zn^{2+} on Microwave Dielectric Properties of $Zn_{1-x}Ni_xZrNb_2O_8$ Ceramics, *J. Electron. Mater.*, 2019, **48**, 6553–6560.

215 M. Xiao, S. He, J. Lou and P. Zhang, Influence of Ge^{4+} substitution for Zr^{4+} on the microwave dielectric properties of $Mg(Zr_{1-x}Ge_x)Nb_2O_8$ ($0 \le x \le 0.4$) ceramics, *Ceram. Int.*, 2018, **44**, 21585–21590.

216 P. Zhang, Y. Zhao and W. Haitao, Bond ionicity, lattice energy, bond energy and microwave dielectric properties of $ZnZr(Nb_{1-x}A_x)_2O_8$ (A=Ta, Sb) ceramics, *Dalton Trans.*, 2015, **44**, 16684–16693.

217 H. L. Pan, Q. Q. Liu, Y. H. Zhang and H. T. Wu, Crystal structure and microwave dielectric characteristics of Co-substituted $Zn_{1-x}Co_xZrNb_2O_8$ ($0 \le x \le 0.1$) ceramics, *RSC Adv.*, 2016, **6**, 86889–86903.

218 H. Wu and E. S. Kim, Characterization of crystal structure and microwave dielectric properties of $AZrNb_2O_8$ (A=Zn, Co, Mg, Mn) ceramics based on complex bond theory, *Ceram. Int.*, 2016, **42**, 5785–5791.

219 M. Xiao, J. Lou and P. Zhang, Characteristics and microwave dielectric properties of low loss $MgZr_{0.85}Sn_{0.15}Nb_2O_8$ ceramics, *J. Mater. Sci.: Mater. Electron.*, 2018, **29**, 18311–18319.

220 M. Xiao, J. Lou, Z. Zhou, Q. Gu, Y. Wei and P. Zhang, Crystal structure and microwave dielectric properties of Ta^{5+} substituted $MgZrNb_2O_8$ ceramics, *Ceram. Int.*, 2017, **43**, 15567–15572.

221 M. Xiao, S. He, J. Meng and P. Zhang, Dependence of microwave dielectric properties on the substitution of isovalent composite ion for Nb-site of $MgZrNb_{2-x}(Sn_{1/2}W_{1/2})_xO_8$ ($0 \le x \le 0.15$) ceramics, *J. Mater. Sci.: Mater. Electron.*, 2019, **30**, 18280–18286.

222 A. Baumgarte and R. Blachnik, Phase relations in the system titaniumdioxide-diniobium-zinc-hexoxide, *Mater. Res. Bull.*, 1992, **27**, 1287–1294.

223 E. S. Kim and H. K. Dong, Relationships between crystal structure and microwave dielectric properties of $(Zn_{1/3}B_{2/3}{}^{5+})_x,Ti_{1-x}O_2$ (B^{5+}=Nb, Ta) ceramics, *Ceram. Int.*, 2008, **34**, 883–888.

224 H. Yang, S. Zhang, H. Yang, X. Zhang and E. Li, Structural Evolution and Microwave Dielectric Properties of x, $Zn_{0.5}Ti_{0.5}NbO_4$-(1−x)$Zn_{0.15}Nb_{0.3}Ti_{0.55}O_2$ Ceramics, *Inorg. Chem.*, 2018, **57**, 8264–8275.

225 H. Yang, S. Zhang, H. Yang, Y. Yuan and E. Li, Intrinsic dielectric properties of columbite $ZnNb_2O_6$ ceramics studied by P–V–L bond theory and Infrared spectroscopy, *J. Am. Ceram. Soc.*, 2019, **10**, 5365–5374.

226 Q. Liao, L. Li, X. Ding and X. Ren, A New Temperature Stable Microwave Dielectric Material $Mg_{0.5}Zn_{0.5}TiNb_2O_8$, *J. Am. Ceram. Soc.*, 2012, **95**, 1501–1503.

227 H. Yang, E. Li, S. Duan, H. He and S. Zhang, Structure, microwave properties and low temperature sintering of Ta_2O_5 and Co_2O_3 codoped $Zn_{0.5}Ti_{0.5}NbO_4$ ceramics, *Mater. Chem. Phys.*, 2017, **199**, 43–53.

228 L. Li, H. Cai, X. Yu, Q. Liao and Z. Gao, Structure analysis and microwave dielectric properties of $Ca_xZn_{1-x}Sn_{0.08}Ti_{1.92}Nb_2O_{10}$ ceramics, *J. Alloys Compd.*, 2014, **584**, 315–321.

229 T. Chen, W. Ma, Q. Sun, C. Tang, Z. Huan and B. Niu, The microwave dielectric properties of $(Ni, Zn)_{0.5}Ti_{0.5}NbO_4$ solid solution, *Mater. Lett.*, 2013, **113**, 111–113.

230 Q. Yang, E. Li, H. Yang, H. Yang, Q. Wen, Y. Yuan and S. Zhang, Influence of $Zn_{0.5}Ti_{0.5}NbO_4$ on the structure and microwave dielectric properties of $ZrTiO_4$ ceramics, *Ceram. Int.*, 2020, **46**, 4543–4549.

231 H. Yang, S. Zhang, H. Yang, Y. Chen, Y. Yuan and E. Li, Effects of ZrO_2 substitution on crystal structure and microwave dielectric properties of $Zn_{0.15}Nb_{0.3}(Ti_{1-x}Zr_x)_{0.55}O_2$ ceramics, *Ceram. Int.*, 2018, **44**, 22710–22717.

232 Y. Chen, S. Zhang, H. Yang, H. Yang, Y. Yuan and E. Li, Bond ionicity, lattice energy and structural evolution of Ta substituted $0.15ZnO\text{-}0.15Nb_2O_5\text{-}0.55TiO_2$ dielectric ceramics, *Ceram. Int.*, 2019, **45**, 8832–8839.

233 W. Luo, L. Li, S. Yu, J. Li, B. Zhang, J. Qiao and S. Chen, Bond theory, terahertz spectra, and dielectric studies in donor-acceptor (Nb-Al) substituted $ZnTiNb_2O_8$ system, *J. Am. Ceram. Soc.*, 2019, **102**, 4612–4620.

234 S. Wang and Y. Zhang, Structure, bond characteristics and microwave dielectric properties of new $A_{0.75}Ti_{0.75}Ta_{1.5}O_6$ (A=Ni, Co, Zn and Mg) ceramics based on complex chemical bond theory, *J. Eur. Ceram. Soc.*, 2020, **40**, 1181–1185.

235 H. Yang, S. Zhang, Y. Chen, H. Yang, Y. Yuan and E. Li, Crystal Chemistry, Raman Spectra, and Bond Characteristics of Trirutile-Type $Co_{0.5}Ti_{0.5}TaO_4$ Microwave Dielectric Ceramics, *Inorg. Chem.*, 2019, **58**, 968–976.